

## ABSTRACT

Title of Document: INTEGRATED MODELING OF RELIABILITY  
AND PERFORMANCE OF 4H-SILICON CARBIDE  
POWER MOSFETS USING ATOMISTIC AND  
DEVICE SIMULATIONS

Devanarayanan Perinthatta Ettisserry,  
Doctor of Philosophy, 2015

Directed By: Professor Neil Goldsman,  
Department of Electrical and Computer Engineering

4H-Silicon Carbide (4H-SiC) power MOSFET is a promising technology for future high-temperature and high-power electronics. However, poor device reliability and performance, that stem from the inferior quality of 4H-SiC/SiO<sub>2</sub> interface, have hindered its development. This dissertation investigates the role of interfacial and near-interfacial atomic defects as the root cause of these key concerns. Additionally, it explores device processing strategies for mitigating reliability-limiting defects.

In order to understand the atomic nature of material defects, and their manifestations in electrical measurements, this work employs an *integrated* modeling approach together with experiments. Here, the electronic and structural properties of defects are analyzed using first-principles hybrid Density Functional Theory (DFT). The insights from first-principles calculations are integrated with conventional physics-based modeling techniques like Drift-Diffusion and Rate equation simulations to model

various device characteristics. Subsequently, the atomic-level models are validated by comparison with experiments.

From device reliability perspective, this dissertation models the time-dependent worsening of threshold voltage ( $V_{th}$ ) instability in 4H-SiC MOSFETs operated under High-Temperature and Gate-Bias (HTGB) conditions. It proposes a DFT-based oxygen-vacancy hole trap activation model, where certain originally ‘electrically inactive’ oxygen vacancies are structurally transformed under HTGB stress to form electrically ‘active’ switching oxide hole traps. The transients of this atomistic process were simulated with inputs from DFT. The calculated time-evolution of the buildup of positively charged vacancies correlated well with the experimentally measured time-dependence of HTGB-induced  $V_{th}$  instability. Moreover, this work designates near-interfacial single carbon interstitial defect in SiO<sub>2</sub> as an additional switching oxide hole trap that could cause room-temperature  $V_{th}$  instability.

This work employs DFT-based molecular dynamics to develop device processing strategies that could mitigate reliability-limiting defects in 4H-SiC MOSFETs. It identifies Fluorine treatment to be effective in neutralizing oxygen vacancy and carbon-related hole traps, unlike molecular hydrogen. Similarly, Nitric Oxide passivation is found to eliminate carbon-related defects.

From device performance perspective, this dissertation proposes a methodology to identify and quantify channel mobility-limiting interfacial defects by integrating Drift-Diffusion simulations of 4H-SiC power MOSFET with DFT. It identifies the density of interface trap spectrum to be composed of *three* atomically distinct defects, one of which is potentially carbon di-interstitial defect.

INTEGRATED MODELING OF RELIABILITY AND PERFORMANCE OF 4H-  
SILICON CARBIDE POWER MOSFETS USING ATOMISTIC AND DEVICE  
SIMULATIONS

By

Devanarayanan Perinthatta Ettisserry

Dissertation submitted to the Faculty of the Graduate School of the  
University of Maryland, College Park, in partial fulfillment  
of the requirements for the degree of  
Doctor of Philosophy  
2015

Advisory Committee:  
Professor Neil Goldsman, Chair  
Professor Agisilaos Iliadis  
Professor Jeremy Munday  
Professor Martin Peckerar  
Professor Lourdes G. Salamanca-Riba

© Copyright by  
Devanarayanan Perinthatta Ettisserry  
2015

# Dedication

*To my Amma, Appan, and Amrutha*

## Acknowledgements

I take this opportunity to convey my deepest gratitude to everyone who has helped and supported me through this journey.

Firstly, I am immensely thankful to Prof. Goldsman for guiding and supporting me throughout this work. He has motivated and supported me from my first day at Maryland, and without his invaluable guidance, this dissertation would not have been possible. I am extremely fortunate to have him as my advisor all these years. My gratitude to him is beyond words.

I express my sincere gratitude to Prof. Peckerar, Prof. Iliadis, Prof. Salamanca-Riba, and Prof. Munday for taking time off their busy schedule to serve on my dissertation committee. Their advice and suggestions were extremely useful for this work.

I thank the U.S. Army Research Laboratory (ARL), Adelphi, MD, for financially supporting this research. I specially thank Dr. Lelis, Dr. Green, and Dan Habersat for providing the experimental data necessary for this work. Their comments and suggestions were very valuable.

I would like to thank Dr. Akturk, Dr. Potbhare and Dr. McGarrity for their constant support and encouragement all these years. The discussions I had with them were really helpful in my research. I did learn a lot from them.

I sincerely thank my friends and colleagues - Chris, Ziyang, Peiwen, Negin, and Shahrzad – for their wonderful company during my time in the lab.

I would like to thank all my friends in College Park who made my life away from home so much enjoyable. Without them, life would have been much harder.

Last but not least, this dissertation would not have been possible without the constant support and encouragement from my parents and family. I thank them for their prayers, and the unwavering confidence they have shown in me and my work. I also thank my wife, Amrutha, for her incredible patience, support, and love.

# Table of Contents

Dedication .....	ii
Acknowledgements .....	iii
Table of Contents .....	v
List of Tables.....	viii
List of Figures .....	ix
Chapter 1: Introduction and Background.....	1
1.1    Research Goals.....	4
1.1.1    Physics-based modeling of high-temperature reliability degradation in 4H-SiC power MOSFETs .....	4
1.1.2    Role of Carbon-related defects in the reliability degradation of 4H-SiC power MOSFETs .....	5
1.1.3    Development of passivation processes for improving device reliability ..	6
1.1.4    Identification and quantification of performance (mobility)-limiting defects at 4H-SiC/SiO <sub>2</sub> interface .....	6
1.2    Key Contributions .....	7
1.2.1    Towards 4H-SiC reliability improvement .....	7
1.2.2    Towards 4H-SiC mobility improvement .....	9
1.3    Literature Survey.....	10
1.3.1    Reliability issues in 4H-SiC power MOSFETs .....	10
1.3.2    Performance- or mobility-related issues in 4H-SiC power MOSFETs ...	14
1.3.3    Device-level modeling of 4H-SiC power MOSFETs.....	17
Chapter 2: Modeling Tools and techniques .....	19
2.1    Drift-Diffusion Simulations.....	19
2.1.1    Mobility Models.....	21
2.1.2    Generation-Recombination Models .....	24
2.2    A Brief Introduction to Density Functional Theory.....	25
2.3    Quantum Molecular Dynamics .....	33
2.4    Minimum Energy Pathway Calculations.....	34
2.5    Methodologies for Generating Amorphous Silica Models.....	37
2.5.1    Sequential Back-bond Break Method.....	39
2.5.2    Melt-and-Quench Molecular Dynamics .....	42
2.6    Computational Setup .....	43
Chapter 3: High Temperature-and-Gate Bias Stress-assisted Reliability Degradation in 4H-SiC Power MOSFETs.....	47
3.1    Background and Motivation .....	47
3.2    Analysis Techniques .....	50
3.2.1    Charge Transition Levels.....	50
3.2.2    Optical Transition Levels .....	52
3.3    Bandgap Alignment .....	53
3.4    Oxygen Vacancy Hole Traps.....	58
3.4.1    ‘Permanently Electrically Active’ Oxygen Vacancy .....	59
3.4.2    ‘Electrically Inactive’ Oxygen Vacancies .....	65

3.4.3	Additional Structural Transformations in Hole-trapped Oxygen Vacancies - Secondary Back-bonding: .....	73
3.5	Transient Modeling of Oxygen vacancy Hole Trap Activation .....	77
3.6	Comparison with other Experimental Observations .....	83
3.6.1	Long-term Threshold Voltage Instability .....	83
3.6.2	EDMR Observations in 4H-SiC Power MOSFETs .....	84
3.6.3	Comparison with Silicon MOSFETs.....	85
3.7	Chapter Summary .....	86
Chapter 4: Additional Reliability-limiting Defects, and Passivation Processes for Reliability Improvement .....		88
4.1	Background and Motivation .....	88
4.2	Hole Trapping by Carboxyl Defects .....	89
4.2.1	Formation and Charge Transition Levels of Carboxyl Defects .....	90
4.2.2	Structural Transformations of Carboxyl Defects upon Hole Trapping ...	93
4.3	Mitigation of Reliability-limiting Defects.....	96
4.3.1	Effect of Nitric Oxide on Carboxyl Hole Traps.....	97
4.3.2	Effect of Nitric Oxide on Oxygen Vacancy Hole Traps .....	101
4.3.3	Implications of NO Treatment on 4H-SiC MOSFET Reliability .....	103
4.3.4	Other Effects of NO Treatment on 4H-SiC MOSFETs – Nitrogen Counter-doping .....	104
4.3.5	Effect of Molecular Hydrogen Treatment on Carboxyl Hole Traps .....	106
4.3.6	Effect of Fluorine Treatment on Carboxyl and Oxygen Vacancy Hole Traps .....	110
4.4	Chapter Summary .....	112
Chapter 5: Integrated Modeling of Performance-limiting Defects in 4H-SiC Power MOSFETs .....		114
5.1	Background and Motivation .....	114
5.2	Methodology for Defect Identification and Quantification.....	115
5.2.1	2D-device Simulations and Experimental Verification.....	116
5.2.2	Algorithm for the Identification and Quantification of Traps .....	118
5.2.3	Density Functional Theory Simulations .....	122
5.3	Simulation Results .....	123
5.3.1	2-D Device Simulation Results.....	123
5.3.2	Results from the Algorithm .....	128
5.3.3	Density Functional Simulation Results .....	129
5.4	Comparison with Experiments.....	133
5.5	Additional Comments on the Methodology .....	135
5.6	Chapter Summary .....	136
Chapter 6: Conclusions, Summary, and Future Work.....		138
6.1	Summary of the Research and Major Conclusions .....	138
6.1.1	General Approach .....	138
6.1.2	Reliability of 4H-SiC Power MOSFETs .....	139
6.1.3	Mitigation of Reliability-limiting Defects.....	141
6.1.4	Performance of 4H-SiC Power MOSFETs.....	142
6.2	Future Work.....	143
References.....		145

Journal and Conference Publications ..... 156

## List of Tables

**Table 1.1:** Physical and electronic properties of 4H-SiC and Silicon.

**Table 5.1:** Extracted parameters for modeling the density of interface traps ( $D_{it}$ ) in equation (5.1).

**Table 5.2:** Trap energy levels and their concentrations extracted using the algorithm for two locations in the channel.

## List of Figures

**Figure 1.1:** Cross-section of a 4H-SiC power MOSFET. Owing to symmetry, only one half is shown.

**Figure 1.2:** A depiction of the switching oxide hole trap model.

**Figure 2.1:** A summary of Kohn-Shan Density Functional Theory as a flow chart.

**Figure 2.2:** A schematic illustration of the minimum energy pathway (MEP) between two stable states on a potential energy surface (PES). The dotted line indicated the initial guess in a NEB calculation.

**Figure 2.3:** (a) Step 1, (b) Step 2, and (c) Step 3, in an iteration of the SBB methodology for generating 72-atom amorphous SiO<sub>2</sub> model. The individual atoms involved in the iteration are indicated. Each supercell in the periodic array is enclosed within the box marked by solid lines.

**Figure 2.4:** The bond angle and bond length distributions in a representative amorphous SiO<sub>2</sub> model generated using the SBB method. The isolated bond angle data points originate from two-membered rings.

**Figure 2.5:** The calculated partial pair correlation function for the amorphous SiO<sub>2</sub> model generated using the SBB method.

**Figure 2.6:** A 72-atom supercell of 4H-SiC used in this work. Blue and yellow spheres represent Silicon and carbon atoms, respectively.

**Figure 3.1:** A Model of 4H-SiC/SiO<sub>2</sub> interface.

**Figure 3.2:** Plane-average electrostatic potential in 4H-SiC bulk as calculated using DFT.

**Figure 3.3:** Plane-average electrostatic potential in a-SiO<sub>2</sub> bulk as calculated using DFT.

**Figure 3.4:** Density of states for 4H-SiC bulk as calculated using DFT. The bandgap is indicated.

**Figure 3.5:** Density of states for a-SiO<sub>2</sub> bulk as calculated using DFT. The bandgap is indicated. The additional state within the bandgap is likely to be due to additional strain.

**Figure 3.6:** Plane-average electrostatic potential across the 4H-SiC/SiO<sub>2</sub> interface as calculated using DFT.

**Figure 3.7:** Bandgap alignment between 4H-SiC and SiO<sub>2</sub> at their interface.

**Figure 3.8:** Sequence of structural transformations of ‘permanently electrically active’ near-interfacial oxygen vacancies seen in highly amorphous oxide regions in 4H-SiC MOSFETs. Bias-dependent tunneling and thermal processes (barriers) are depicted as solid and dashed lines, respectively. Large blue spheres and small red spheres represent Si and O atoms, respectively. The shaded regions represent the calculated Electron Localization Function (ELF) isosurfaces at ELF=0.89, with the

adjacent red arrow/s showing the type of localization (unpaired/paired). fp- and bp- stand for forward-projected and back-projected, respectively. The sequence involving dimer and forward-projected configurations resemble the HDL model.

**Figure 3.9:** Most stable charge states as a function of Fermi level for various ‘permanently electrically active’ oxygen vacancy configurations seen in highly amorphous oxide regions in 4H-SiC MOSFETs. The shaded region represents the experimental bandgap line up between 4H-SiC and SiO<sub>2</sub>. Solid vertical lines represent theoretical bandgap lineup. The kinks represent charge transition level for the respective configuration, which is seen to move towards right as the vacancy accesses higher energy structures. All the configurations are permanent switching oxide traps due to their +1/0 CTL within the 4H-SiC bandgap.

**Figure 3.10:** Minimum energy pathways, calculated using standard DFT-based nudged elastic band (NEB) method, for thermally-assisted transition between various ‘permanently electrically active’ oxygen vacancy configurations in 4H-SiC MOSFETs. (a) neutral dimer  $E_{\delta}$ ’ to neutral forward-projected (fp)  $E_{\gamma}$ ’, (b) positive forward-projected  $E_{\gamma}$ ’ to positive back-projected (bp)  $E_{\gamma}$ ’, and (c) neutral forward-projected  $E_{\gamma}$ ’ to neutral back-projected  $E_{\gamma}$ ’. The atomic arrangements of initial, final and saddle point structures are indicated. Hybrid functional DFT was used to recalculate the energies at these special reaction coordinates (indicated as red squares) to determine the activation barriers.

**Figure 3.11:** Sequence of structural transformations involved in the negative bias-and-temperature-assisted activation of ‘electrically inactive’ near-interfacial oxygen vacancies seen in less amorphous oxide regions to form ‘electrically active’ hole traps in 4H-SiC MOSFETs. The  $E_{\delta}$ ’ dimers are ‘electrically inactive’, as opposed to the ‘electrically active’ forward-projected (fp) and back-projected (bp)  $E_{\gamma}$ ’ structures. Bias-dependent tunneling and thermal processes (barriers) are depicted as solid and dashed lines, respectively. However, the final barrier for trap activation also depends on the 4H-SiC/SiO<sub>2</sub> bandgap alignment (see text). Large blue spheres and small red spheres represent Si and O atoms, respectively. The shaded regions represent the calculated Electron Localization Function (ELF) isosurfaces at ELF=0.89, with the adjacent red arrow/s showing the type of localization (unpaired/paired).

**Figure 3.12:** Most stable charge states as a function of Fermi level for ‘electrically inactive’ Si-Si dimer seen in less amorphous oxide regions in 4H-SiC MOSFETs, and its subsequent NBTS-activated configurations. The shaded region represents the experimental bandgap line up between 4H-SiC and SiO<sub>2</sub>. Solid vertical lines represent theoretical bandgap lineup. The kinks represent charge transition level (CTL) for the respective configuration, which is seen to move towards right as the vacancy accesses higher energy structures leading to hole trap activation. The initial Si-Si inactive dimer with +1/0 CTL below 4H-SiC bandgap is activated to form switching oxide hole traps with +1/0 CTL within the bandgap during NBTS.

**Figure 3.13:** Minimum energy pathways, calculated using standard DFT-based nudged elastic band (NEB) method, for thermally-assisted inter-conversions between various oxygen vacancy configurations seen in less amorphous oxide regions in 4H-SiC MOSFETs. (a) positive dimer  $E_{\delta}$ ’ to positive forward-projected (fp)  $E_{\gamma}$ ’, (b)

neutral dimer  $E_{\delta}'$  to neutral forward-projected  $E_{\gamma}'$  (c) positive dimer  $E_{\delta}'$  to positive back-projected (bp)  $E_{\gamma}'$ , (d) neutral dimer  $E_{\delta}'$  to neutral back-projected  $E_{\gamma}'$ , and (e) positive forward-projected  $E_{\gamma}'$  to positive back-projected  $E_{\gamma}'$ . The atomic arrangements of initial, final and saddle point structures are indicated. Hybrid functional DFT was used to recalculate the energies at these special reaction coordinates (indicated as red squares) to determine the activation barriers. However, the final barrier for trap activation also depends on the 4H-SiC/SiO<sub>2</sub> bandgap alignment (see text).

**Figure 3.14:** Additional structural transformations in hole trapped oxygen vacancies. a) Secondary back-bonding leading to the migration of positively charged Si center, b) energy gained through secondary back-bonding based on a statistics of oxygen vacancy hole traps. Red and blue represents positive and negative energy changes, respectively.

**Figure 3.15:** Comprehensive model for the activation of electrically inactive oxygen vacancies, including secondary back-bonding. The structural transformations during neutralization (electron capture) are also indicated. The shaded regions represent the calculated Electron Localization Function (ELF) isosurfaces at ELF=0.89, with the adjacent red arrow/s showing the type of localization (unpaired/paired).

**Figure 3.16:** The HTGB stress-and-measure sequence used in the experimental measurement of threshold voltage instability in 4H-SiC power MOSFETs. The absolute threshold voltages are measured during the sweep up/down sequences, after a course of bias stress. The difference between the measured absolute threshold voltages is defined as the threshold voltage instability ( $\Delta V_{th}$ ).

**Figure 3.17:** The hole trap activation model during NBTS. The thermal transformations in hole-trapped oxygen vacancies are indicated by dotted lines. The NEB-calculated barriers are indicated in black. The barriers used in the rate equation-based modeling are indicated within parenthesis in red. The various states are labelled within the circles.

**Figure 3.18:** Simulation of the HTGB stress-assisted  $\Delta V_{th}$  transients in 4H-SiC MOSFET using the oxygen vacancy hole trap activation model. Circles represent experimental data points. The room-temperature contribution is subtracted from the measured threshold voltage instability at the indicated temperatures.

**Figure 4.1:** a) Configuration with a single carbon interstitial located at the 4H-SiC/SiO<sub>2</sub> interface, at the start of the quantum molecular dynamics (QMD) simulation, b) Si-O-C-Si bridge, which is rapidly formed, by the end of 1ps long QMD run.

**Figure 4.2:** Minimum energy pathway for the formation of carboxyl defect from silicon oxycarbide (Si-O-C-Si) bridge in amorphous SiO<sub>2</sub>. The initial, saddle point and final configurations are given in the inset. Silicon - blue, Carbon - yellow, Oxygen - red.

**Figure 4.3:** Formation energy of the carboxyl defect for various charge states in SiO<sub>2</sub>. Energies are relative to the neutral state (dotted line). The (+2/0) charge transition

level is shown. Theoretical 4H-SiC/SiO<sub>2</sub> bandgap alignment, achieved in Section 3.3, is used here.

**Figure 4.4:** Structural transformations in carboxyl defect upon hole capture. a) Neutral state, b) +1 charged state, and c) +2 charged state. Silicon - blue, Carbon - yellow, Oxygen - red.

**Figure 4.5:** Electron localization function isosurfaces at two isovalues for the carboxyl defect in its stable neutral and doubly positive charge states. High isovalue is chosen to identify the localization domains of lone pairs (LP) on oxygen. Low isovalue reveals the localization of bonding pairs (BP) in the carbon-oxygen bond. a) ELF = 0.89 and neutral state, b) ELF = 0.8 and neutral state, c) ELF = 0.89 and +2 state, and d) ELF = 0.8 and +2 state. Only the ELF around the carboxyl defect is shown. Silicon - blue, Carbon - yellow, Oxygen - red. Isosurfaces are in grey.

**Figure 4.6:** Diffusion of NO in along two paths in a-SiO<sub>2</sub>, and its NEB-calculated minimum energy pathways. The NO molecule is circled.

**Figure 4.7:** The mechanism of NO passivation of carboxyl defect. (a) - (e) represents various structural configurations during the defect removal. (f) shows Nitrogen incorporation in the SiO<sub>2</sub> lattice. Silicon - blue, Carbon - yellow, Oxygen - red, Grey-Nitrogen.

**Figure 4.8:** The NEB-calculated minimum energy pathway for the reaction between NCO and NO to give N<sub>2</sub> and CO<sub>2</sub> in SiO<sub>2</sub> void. Lattice atoms are not shown. (a) initial configuration with NCO and NO, b) intermediate nitrocylic isocyanate (ONNCO), (c) configuration of cyclic intermediate, and (d) final products, N<sub>2</sub> and CO<sub>2</sub>. All the components are unconnected to the SiO<sub>2</sub> lattice. Silicon - blue, Carbon - yellow, Oxygen - red, Grey- Nitrogen.

**Figure 4.9:** The basic nitroxyl defect configuration in its neutral state.

**Figure 4.10:** Minimum energy pathway for the rapid formation of nitroxyl configuration from a nitrogen interstitial in bulk a-SiO<sub>2</sub>.

**Figure 4.11:** Higher energy configurations of the nitroxyl structure achieved during NBTS, and their formation energies in various charge states as a function of Fermi level.

**Figure 4.12:** a) Incorporation of NO into 4H-SiC surface at the interface, b), c), d) various resulting configurations with their relative energies. The most feasible path results in e) counter-doping, f) re-oxidation.

**Figure 4.13:** Structural transformations in H<sub>2</sub> passivated - carboxyl defect upon hole capture. a) Neutral state, b) +1 charged state, and c) +2 charged state. Bond lengths are indicated along the bonds in angstroms. Silicon - blue, Carbon - yellow, Oxygen - red, Hydrogen - grey.

**Figure 4.14:** Formation energy of H<sub>2</sub>-passivated carboxyl defect in various charge states in SiO<sub>2</sub>. The energy of the neutral defect is taken as the reference (dotted line). The (+2/0) charge transition level is marked. 4H-SiC bandgap exists in between the vertical lines.

**Figure 4.15:** Electron localization function isosurfaces at two isovalues for the H<sub>2</sub> passivated - carboxyl defect in its stable neutral and doubly positive charge states. High isovalue is chosen to identify the localization of lone pairs (LP) on oxygen. Low isovalue identifies the localization domains of bonding pairs (BP) in the carbon-oxygen bond, a) ELF = 0.9 and neutral state, b) ELF = 0.8 and neutral state, c) ELF = 0.9 and +2 state, and d) ELF = 0.8 and +2 state. Only the ELF around the defect is shown. Silicon - blue, Carbon - yellow, Oxygen - red, Hydrogen - small blue. Isosurfaces are in grey.

**Figure 4.16:** a) The structure resulting from Fluorine passivation of carboxyl or oxygen vacancy hole trap, b) Formation energy of the Fluorine-related structure in various charge states in SiO<sub>2</sub>. The energy of the neutral defect is taken as the reference (dotted line). 4H-SiC bandgap exists in between the vertical lines. No CTL is seen within the 4H-SiC bandgap, indicating the effectiveness of Fluorine passivation in improving device reliability.

**Figure 5.1:** Methodology for the identification and quantification of mobility-reducing traps in 4H-SiC/SiO<sub>2</sub> interface.

**Figure 5.2:** Experimental and simulated I<sub>D</sub>-V<sub>D</sub> characteristics of 4H-SiC power MOSFET for different temperatures. Measurements were done at the U.S. Army Research Lab, Adelphi, MD.

**Figure 5.3:** Experimental and simulated I<sub>D</sub>-V<sub>G</sub> characteristics of 4H-SiC power MOSFET for different temperatures. Measurements were done at the U.S. Army Research Lab, Adelphi, MD.

**Figure 5.4:** Fermi level position as a function of gate bias at different temperatures as calculated by 2D-device simulations. The voltage regime where the algorithm is applied is shown in the inset.

**Figure 5.5:** Occupied trap concentration at different gate voltages and temperatures as calculated by 2D-device simulations. The voltage regime where the algorithm is applied is shown in the inset.

**Figure 5.6:** (a) Silicon vacancy at cubic site (*k*-center), (b) Silicon vacancy at hexagonal site (*h*-center) and (c) Carbon di-interstitial defect. The defects are circled and are in their neutral states. Larger spheres represent Silicon and smaller spheres represent Carbon.

**Figure 5.7:** Positions of thermodynamic charge transition levels of defects in the bandgap of 4H-SiC/SiO<sub>2</sub> interface. The valence band maximum and conduction band minimum are shown as dotted lines. Si vacancy at *h*- and *k*- centers in charge states of +2, +1, 0, -1 and -2 were examined. Similarly, C di-interstitial in 0, -1 and -2 charge states were studied.

**Figure 5.8:** Pictorial representation of carbon di-interstitial defect. The arrows represent bonds. The dotted lines show the ideal bonding in the absence of the defect.

## Chapter 1: Introduction and Background

4H-Silicon carbide (4H-SiC)-based Metal-Oxide-Semiconductor Field-Effect Transistors (MOSFETs) are beginning to be available in the market for high temperature and high power applications. Their eventual large-scale replacement of Silicon in conventional power electronic circuits (like rectifiers, inverters and variable frequency drives) is expected to result in massive improvements in energy efficiency with extremely low loss. Important application areas that could benefit from the deployment of 4H-SiC-based electronics include industrial motor systems, data centers, consumer electronics and renewable energy industry.

On the other hand, 4H-SiC based electronics could also be extremely promising for niche military, space, and aerospace applications. This is due to its capability to withstand high temperatures along with high-power. Once fully mature, this technology will also find important use in future transportation technologies (For example, hybrid/electric cars, rail transport, fuel cells etc.) and energy harvesting (solar/wind) systems. In short, 4H-SiC technology holds the key to revolutionizing high-power and high-temperature electronics, similar to Silicon that dramatically changed the consumer and portable electronics industry.

The qualities that render Silicon Carbide superior to Silicon for high-temperature and high-power applications include its wide bandgap, high thermal conductivity and high breakdown electric field. Additionally, silicon dioxide ( $\text{SiO}_2$ ) could be naturally grown on 4H-SiC by thermal oxidation to form stable semiconductor-dielectric (4H-SiC/ $\text{SiO}_2$ ) junction – a critical feature in metal-oxide-semiconductor field effect

transistors (MOSFET). A comparison between important electrical and thermal properties of 4H-SiC and Silicon is given in Table 1.1 [1].

Table 1.1: Physical and electronic properties of 4H-SiC and Silicon.

Property	4H-SiC	Silicon
Bandgap (eV)	3.2	1.1
Critical electric field (MV/cm)	2.2	0.25
Saturation velocity ( $10^7$ cm/s)	2.0	1.0
Thermal conductivity (W/cm K)	5.0	1.5
Bulk electron mobility (cm <sup>2</sup> /Vs)	950	1350
Bulk hole mobility (cm <sup>2</sup> /Vs)	120	480
Relative permittivity	10.0	11.9

Now, I briefly touch upon how these material properties affect the electrical characteristics of 4H-SiC power MOSFETs (which is pictorially shown in Figure 1.1 [2]) in relation to Silicon MOSFETs. From Table 1.1, the bandgap of 4H-SiC is about three times higher than that of Silicon. Thus, the Electron-Hole Pair (EHP) generation rate during processes like impact ionization is much limited in 4H-SiC, making it suitable for high power electronics. The wide bandgap also enables reliable operation of 4H-SiC MOSFETs in high temperature regime. The critical electric field of 4H-SiC is about ten times higher than Silicon. This means that 4H-SiC devices are not only capable of handling higher voltages, but also are amenable to size scaling in comparison with Silicon MOSFETs. The high electron saturation velocity in 4H-SiC, which is twice that of Silicon, makes it attractive for high frequency applications. The thermal conductivity of 4H-SiC is about thrice as high as Silicon. This enables 4H-

SiC MOSFETs to dissipate heat faster than Si MOSFETs – a quality that is crucial for high temperature and power applications.

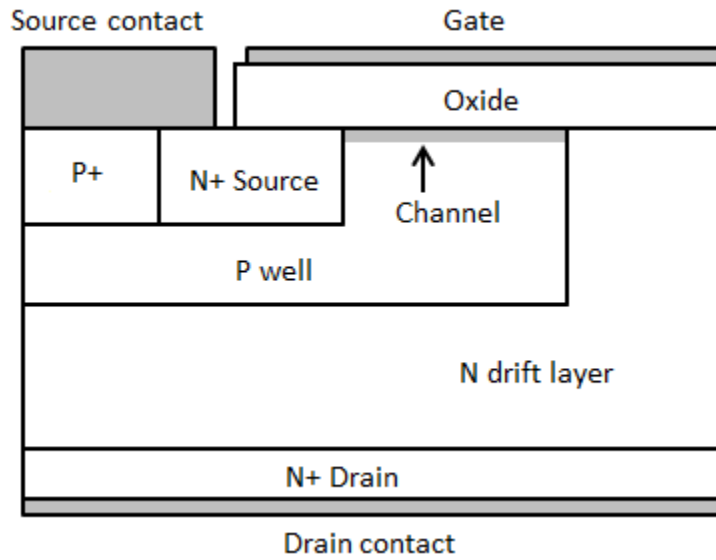


Figure 1.1: Cross-section of a 4H-SiC power MOSFET. Owing to symmetry, only one half is shown.

However, this critically important technology does not come without its own problems. The significantly high density of defects at or near the 4H-SiC/SiO<sub>2</sub> interface of MOSFETs has limited the technology from being realized to its full potential. This is generally attributed to the high temperature oxidation process of 4H-SiC to form 4H-SiC/SiO<sub>2</sub> interface, especially in the presence of carbon. Extremely high density of interface states ( $D_{it}$ ) has been measured in 4H-SiC MOSFETs resulting in poor surface electron mobility [2, 3]. Similarly, threshold voltage ( $V_{th}$ ) instabilities attributed to border hole trapping has been reported [4, 5, 6, 7, 8]. Moreover,  $V_{th}$  instability has been recently shown to worsen intolerably at higher temperatures [9]. Consequently, the efficiency and the reliability of present-day

devices are compromised – largely owing to the poor quality of the 4H-SiC/SiO<sub>2</sub> interface and other near-interfacial defects. In the following section, I outline the specific goals of this Ph.D. work in the direction of understanding and mitigating degradation mechanisms in 4H-SiC MOSFETs.

## 1.1 Research Goals

The overall goal of this PhD research is to model the atomic-level physical phenomena that are detrimental to the reliability and performance of 4H-SiC MOSFETs, in view of recent experimental observations. Additionally, suitable process modifications that could mitigate the effects of such reliability- and performance-limiting mechanisms merit investigation. Broadly, this PhD research focuses on a) physics-based modeling of the reliability-limiting aspects in 4H-SiC power MOSFETs (which includes the recently observed high-temperature effects), b) physics-based modeling of the performance-limiting aspects in 4H-SiC MOSFETs, and c) development of suitable processing techniques to improve device reliability. The specific problems are further elaborated below.

### 1.1.1 Physics-based modeling of high-temperature reliability degradation in 4H-SiC power MOSFETs

The room-temperature threshold voltage instability, which varies linearly with the logarithm of applied stress time, is typically attributed to oxygen vacancy (OV) border hole traps. A two-way tunneling model was developed previously in my lab to explain this behavior by assuming hole tunneling into and out of the OV hole traps in response to applied bias [10]. However, recent measurements of  $V_{th}$  instability carried

out at higher temperatures ( $T > 125^\circ\text{C}$ ) revealed its excessive aggravation, which was super linear with the logarithm of applied stress time [9]. This is a clear departure from the room temperature behavior, and deserves detailed investigation. One of the goals of this research is to identify the atomistic mechanisms responsible for this critical reliability-degrading effect. It is also imperative to validate the suitability of the atomistic model using transient modeling, and comparison with measurement data. In this direction, a major outcome of this thesis is the oxygen vacancy hole trap activation model, which explains the high-temperature gate bias  $V_{th}$  instability in 4H-SiC power MOSFETs. This model also supports measurement data, and a variety of other experimental observations.

#### 1.1.2 Role of Carbon-related defects in the reliability degradation of 4H-SiC power MOSFETs

Traditionally, hole trapping and associated  $V_{th}$  instability in 4H-SiC MOSFETs have been attributed to near-interfacial oxygen vacancies. While oxygen vacancies are indeed potential candidates, other defects also need to be explored. This is especially important in the context of 4H-SiC MOSFETs which are prone to contamination from carbon and its compounds during the high-temperature oxidation process involved in their fabrication. This hypothesis is further strengthened in the view of recent oxidation models which explicitly consider atomic carbon emission into the oxide during 4H-SiC oxidation (similar to Si emission in Si oxidation) [11]. This aspect of my Ph.D. entails the determination of the most stable carbon-related defect configuration in silicon dioxide, and investigations into its electrical properties and stability-providing bonding mechanisms. To this end, I investigate a basic defect

involving carbon, which is a single carbon interstitial existing in the near-interfacial oxide region. The major outcome here is the identification of single carbon interstitial, existing in carboxyl configuration, as a potential candidate for switching oxide hole traps causing  $V_{th}$  instability (in addition to oxygen vacancy centers). Additionally, its stability-providing bonding mechanisms are also presented.

### 1.1.3 Development of passivation processes for improving device reliability

Following the identification of defects and mechanisms responsible for reliability degradation, fabrication steps that could mitigate these ‘root-causes’ should be identified. The interaction between defects and various chemicals like NO, Fluorine, hydrogen etc. deserve to be studied. The stability and charge trapping behavior of resulting reaction products and associated new defect configurations can throw light on the effectiveness of various passivation schemes. Additionally, other effects of passivation like Nitrogen counter-doping during NO treatment are intensely debated currently, and warrant investigation. This Ph.D. thesis includes my findings on these important topics as well.

### 1.1.4 Identification and quantification of performance (mobility)-limiting defects at 4H-SiC/SiO<sub>2</sub> interface

A major factor that has kept 4H-SiC MOSFET technology from realizing its full potential is the high density of interface traps near the 4H-SiC conduction band edge. This is believed to adversely affect channel mobility, and hence the performance of 4H-SiC MOSFETs. It is important to know the number of distinct defects contributing to the high  $D_{it}$  spectrum, their individual concentrations, and their atomic

make-up. Such information would be helpful in designing and developing novel passivation techniques to mitigate these defects. This work addresses these issues by developing a methodology to identify and quantify mobility-limiting defects responsible for high  $D_{it}$  at 4H-SiC/SiO<sub>2</sub> interface. This was achieved by uniquely integrating 2D-device simulations (which are calibrated against experimental I-V measurements) of a sample 4H-SiC power MOSFET and density functional calculations of possible interface defects. In this direction, I have resolved the  $D_{it}$  spectrum into a summation of three distinct defects, one of which was identified to be Carbon di-interstitial in 4H-SiC substrate. The calculated trap levels were compared against experiments like C-V measurements and Deep Level Transient Spectroscopy (DLTS) for validating the methodology.

## 1.2 Key Contributions

The key contributions of this work, which could be helpful towards improving the reliability- and performance-related aspects of 4H-SiC power MOSFETs in future, are summarized below.

### 1.2.1 Towards 4H-SiC reliability improvement

- Developed a novel algorithm, called the Sequential Back-bond Break (SBB) method, for the generation of realistic amorphous silicon dioxide models.
- Identified and modeled the role of oxygen vacancy hole traps in 4H-SiC MOSFET reliability degradation.
  - Identified two energetically distinct near-interfacial oxygen vacancy hole traps in silicon dioxide, which separately contribute to room-

temperature and high-temperature gate bias stress-induced threshold voltage instability (a serious reliability concern) in 4H-SiC power MOSFETs.

- Developed an atomistic model for the excessive aggravation in  $V_{th}$  instability under High-Temperature ( $T > 125^{\circ}\text{C}$ ) and Gate Bias (HTGB) stressing (called the oxygen-vacancy border hole trap activation model).
- Identified critical stability-providing structural transformations in oxygen vacancy defects during their activation, and calculated the associated activation barriers.
- Mathematically modeled the transients of the activation of electrically ‘inactive’ oxygen vacancy defects to form electrically ‘active’ hole traps under HTGB stressing.
- Validated the oxygen-vacancy hole trap activation model by comparison with  $V_{th}$  instability measurements in 4H-SiC MOSFETs.
- Identified the role of Carbon-related defects in 4H-SiC MOSFET reliability degradation.
  - Proposed single carbon interstitial defect (existing in the carboxyl configuration), located in the oxide of 4H-SiC power MOSFETs, as a major switching oxide hole trap that causes room-temperature  $V_{th}$  instability .

- Determined the stability-providing bonding rearrangements and structural transformations that enable hole trapping by single carbon interstitial defects.
- Process modifications to improve 4H-SiC MOSFET reliability.
  - Identified Fluorine passivation to be very effective in mitigating carbon and oxygen vacancy-related reliability-limiting hole traps.
  - Identified controlled Nitric Oxide passivation to be effective in mitigating carbon-related reliability-limiting hole traps. Determined the atomic-level interactions between the NO molecule and the carboxyl defect in detail.
  - Showed that Nitrogen incorporation at 4H-SiC/SiO<sub>2</sub> interface during NO passivation– a process called counter-doping – is energetically favorable.
  - Concluded that molecular hydrogen passivation is ineffective in mitigating carbon-related reliability-limiting defects.

### 1.2.2 Towards 4H-SiC mobility improvement

- Modeled the I-V characteristics of a 1200V/50A 4H-SiC power MOSFET by numerically solving the Drift-Diffusion equations.
- Developed a novel methodology to,
  - identify the number of distinct defects involved in the density of interface trap ( $D_{it}$ ) spectrum,
  - calculate the associated trap levels,
  - calculate their individual concentrations, and

- identify their atomic make-up by incorporating Density Functional Theory.
- Identified carbon dimer defect as a possible contributor to the high density of interface traps.

### 1.3 Literature Survey

A literature survey on the reliability- and performance-related aspects of 4H-SiC MOSFETs is presented in the following sections.

#### 1.3.1 Reliability issues in 4H-SiC power MOSFETs

At present, the reliability of 4H-SiC power MOSFETs continues to be a matter of serious concern. Unfortunately, this issue has received limited attention in comparison with the large volume of work directed towards mobility enhancement in 4H-SiC MOSFETs.

Threshold voltage ( $V_{th}$ ) instability, in response to applied bias at room temperature has been experimentally observed in 4H-SiC MOSFETs [4, 5, 6, 7, 8]. Here, the threshold voltage of an n-channel 4H-SiC MOSFET shifts negatively (positively) after an applied negative (positive) bias stress. Experimentally, the measured back-and-forth  $V_{th}$  instability (which is the difference between the absolute threshold voltages measured before and after the application of bias stress) was seen to vary linearly with logarithm of applied stress time. This is characteristic of charging and discharging of oxide traps through direct tunneling [10]. However, significant aggravation of  $V_{th}$  instability has been recently reported under high temperature-gate bias (HTGB) stresses (for  $T > \sim 125^\circ\text{C}$ ) [9]. The atomic origins of

such HTGB-assisted reliability degradation effects are not completely investigated or understood.

Recently, a two-way tunneling model was developed to explain the *room-temperature*  $V_{th}$  instability in 4H-SiC MOSFETs [10]. According to this model, near-interfacial oxygen vacancies trap and de-trap holes (or electrons) in response to applied bias, causing threshold voltage instability. The origin of this model lies in the switching oxide hole trap model, where oxygen vacancies were designated as hole traps (also called the  $E'$  centers). This model was originally developed for Silicon MOSFETs [12], and a brief account of the atomic description of this model is given below.

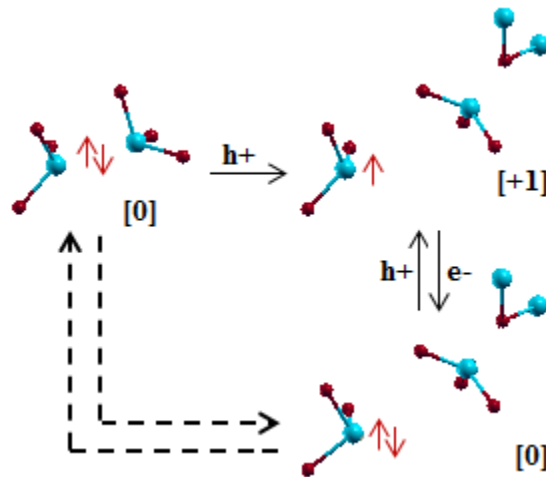


Figure 1.2: A depiction of the switching oxide hole trap model.

The ‘switching oxide hole trap’ model (also called the HDL model or Lelis model) was developed in the early 1990’s in the context of threshold voltage instabilities observed in irradiated Si MOSFETs [12]. This model is pictorially depicted in Figure 1.2. According to this model, an oxygen vacancy in SiO<sub>2</sub> results in

the formation of weak Si-Si dimer linkage – a precursor for switching oxide traps. Upon hole capture, the positively charged Si moves away from the Si with a dangling electron. In the event of hole emission (equivalently, electron capture through tunneling), the captured electron pairs with the lone electron on Si. Thus, the neutralization of defect is achieved through the formation of a dipole. Subsequent emission/capture cycle of the captured electron would preserve the structural configuration (without relapsing into the original Si-Si dimer state, which would require sufficient thermal energy to overcome a thermal barrier). Such defects were predicted to exchange charge with the substrate depending on the substrate Fermi level, thereby acting as ‘switching oxide traps’ and causing threshold voltage instability. The HDL model was subsequently validated by Conley *et. al.* through ESR measurements [13]. Additionally, the generation of E’ center was also observed under negative bias and elevated temperature using on the fly ESR measurement [14]. Recently, studies by Grasser *et. al.* attributed the origin of threshold voltage instability in Si MOSFETs to E’ centers in SiO<sub>2</sub> [15]. Thus, the HDL model appears to be a plausible model for describing  $V_{th}$  instability in 4H-SiC MOSFETs as well.

The hole trapping behavior of oxygen vacancies has been extensively investigated previously using density functional theory as well [16, 17, 18, 19, 20, 21, 22]. Rudra *et. al.* reported a puckered configuration of positively charged oxygen vacancies in crystalline SiO<sub>2</sub> [19]. Here, the hole trapped silicon was seen to back-bond with a rear-oxygen (A ‘back-bond’ is the bond between positively charged Silicon atom and an oxygen atom behind it). However, in amorphous SiO<sub>2</sub>, Uchino *et. al.* predicted three more distinct transformations apart from the puckered configuration [17].

Similarly, theoretical calculations by Lu *et. al.* revealed the existence of structurally different oxygen vacancies that responded differently to hole capture [16]. The structural transformations shown by some of them upon hole trapping was consistent with that of the switching oxide traps proposed by the Lelis model in Figure 1.2. Recent studies by Kimmel *et. al.* on doubly ionized oxygen vacancies revealed two distinct puckered configurations, where one or both of the positive Si atoms were seen to back-bond with oxygen [21]. Structural transformation like puckering was suggested to be a major stability-providing mechanism for positively charged oxygen vacancies [22]. In general, it could be concluded that the structural transformation of oxygen vacancies upon hole capture strongly depends on the local environment.

As mentioned earlier in this section, the switching oxide trap model was recently applied in the context of 4H-SiC/SiO<sub>2</sub> interfaces to explain its room-temperature threshold voltage instability [4]. Positively charged oxygen vacancies ( $E'$  centers) located close to the interface were held responsible for electron trapping and de-trapping leading to threshold voltage variations [4, 6], as in Figure 1.2. This model was further validated using the two-way tunneling model [10]. However, recently observed excessive aggravation of  $V_{th}$  instability for bias stresses at temperatures higher than 125°C is poorly understood [9].

Additionally, given the more complex oxidation process of 4H-SiC, and various post-oxidation chemical treatment of the interface, it becomes imperative to study alternate candidate defects that could behave like switching oxide traps [11, 23, 24, 25, 26]. Previous studies have pointed towards carbon interstitials as potential hole traps [23]. Additionally, while some studies have reported positive impact of Nitric

Oxide treatment on  $V_{th}$  instability [4], there are other works which suggested otherwise [27, 28].

### 1.3.2 Performance- or mobility-related issues in 4H-SiC power MOSFETs

The low performance or channel mobility ( $\sim 10\text{-}20\text{ cm}^2/\text{Vs}$ ) displayed by 4H-SiC power MOSFETs is believed to be due to the poor quality of 4H-SiC/SiO<sub>2</sub> interface. Unacceptably high density of interface traps ( $D_{it}$ ) is typically observed, especially very close to 4H-SiC conduction band edge. These centers are not only believed to trap channel electrons, but also act as Coulomb scattering centers that further reduce mobility [3]. Apart from isolated or clustered defects [29], the existence of a transition region (with low channel electron mobility) has also been reported previously [24, 25]. In general, the approach towards investigating performance- or mobility-limiting factors in 4H-SiC MOSFETs has been typically through the electrical and chemical characterization of 4H-SiC/SiO<sub>2</sub> interfaces. I will describe this briefly in the next paragraph.

The approach to explore the structural and electrical properties of the interface has been both experimental and theoretical. Experimental techniques like high-resolution Transmission Electron Microscopy (TEM), Z-contrast scanning TEM and Electron Energy-Loss Spectroscopy (EELS) have been used in the past to characterize the interface transition region [24, 25, 26]. The Carbon-to-Silicon ratio in the transition region was found to be greater than 1 and the electron mobility was found to be inversely proportional to the width of the transition region [25]. Rudenko *et al.* investigated the interface for isolated/clustered defect centers using Capacitance-Voltage (C-V) and Thermally Stimulated Current (TSC) measurements [30]. They

observed two distinguishable TSC signatures – one originating from the defects close to the interface and the other, from the defects distributed in the transition layer. Afanas'ev *et al.* used Constant-Capacitance Deep Level Transient Spectroscopy (CC-DLTS) and Internal Photoemission Spectroscopy (IPE) to study the energy distribution of interface defects and attributed high  $D_{it}$  to Carbon clusters and near-interface defects in oxide [29]. Basile *et al.* calculated three traps levels in 4H-SiC/SiO<sub>2</sub> bandgap using C-V and CC-DLTS measurements [31]. While one of them (in SiC side of the interface) had activation energy of less than 0.1 eV, the other two (in oxide) were distributed around 0.15 eV and 0.4 eV below the conduction band. Recent spin-dependent recombination (SDR) experiments indicate the presence of Silicon vacancies in 4H-SiC as a major cause of electron trapping in 4H-SiC MOSFETs [32, 33].

In contrast, theoretical studies using Density Functional Theory (DFT) have also been carried out by researchers to understand the electrical properties of the 4H-SiC/SiO<sub>2</sub> interface [34, 35, 36, 37, 38, 39, 40, 41, 42, 43]. The most common methodology is to model a realistic 4H-SiC/SiO<sub>2</sub> interface using molecular dynamics and subsequently introduce various possible defects to study their effects on the bandgap. Recently, Devynck *et al.* simulated the trap levels created by various Carbon, Oxygen and Hydrogen related defects using hybrid functional-based DFT [37]. Their calculations pointed to the oxide defect wherein a C-O unit replaces the O in Si-O-Si linkage to be responsible for poor MOS channel mobility. Such defects were shown to produce trap states very close to the conduction band (CB) and valence band (VB) edges of 4H-SiC. At the same time, Carbon di-interstitials in SiC

side of the interface were also shown to create states near 4H-SiC CB edge [36]. This is in agreement with the findings of Shen *et al.* [41, 42]. Moreover, Carbon emission into 4H-SiC during oxidation and formation of immobile C di-interstitials were also investigated [44]. However, Knaup *et al.* argued that high  $D_{it}$  near interface was a result of C pairs replacing two nearby O atoms in SiO<sub>2</sub> [39]. Silicon and Carbon vacancies were also examined in bulk 4H-SiC using DFT [43]. In essence, an agreement on the exact atomic nature of defects contributing to high  $D_{it}$  is still not reached.

Previous DFT work conducted in my lab involved investigations into the effects of near-interfacial substrate single carbon, double-carbon and silicon vacancy defects on the density of states of the 4H-SiC/SiO<sub>2</sub> interface system [40]. While the DOS corresponding to both the carbon-related defects indicated states near the conduction and valence band edges, Si vacancies were seen to introduce states near the valence band. The study suggested that nitrogen and hydrogen would effectively passivate these defects. This study was performed directly through the Kohn-Sham levels rather than the charge transition levels.

Significant efforts have been directed in the past to develop suitable passivation processes to improve 4H-SiC MOSFET mobility. In this direction, Nitric Oxide passivation is now routinely used by SiC MOSFET manufacturers, as they were observed to reduce the density of interface traps [45]. Other passivation schemes involving Phosphorous and Antimony were also seen to be promising [46, 47]. These elements like Nitrogen, Phosphorous, and Antimony are believed to act as counter-dopants which enhance the effective channel mobility through a variety of

mechanisms [46, 48]. However, the complete mechanisms of interaction between these passivants and the 4H-SiC/SiO<sub>2</sub> interface is still open to debate.

Alternately, 4H-SiC MOSFETs fabricated on the (11 $\bar{2}$ 0) face of 4H-SiC substrate (as opposed to the conventional (0001) face) are also being investigated for improved mobility [46]. In my view, the general strategy for fabricating future high-mobility power MOSFETs would involve selecting a suitable substrate orientation combined with a sequence of multiple passivation schemes after rigorous optimization. These various aspects are currently under intense research.

### 1.3.3 Device-level modeling of 4H-SiC power MOSFETs

As discussed in the previous section, efforts have been directed in the past towards understanding the microscopic nature of the 4H-SiC/SiO<sub>2</sub> interface. However, an agreement still seems distant. On the other hand, the effects of these defects on the performance of MOSFETs have been physically modeled. For example, the interface traps are known to reduce the effective channel mobility by trapping free electrons. Subsequently, these charged traps scatter the un-trapped channel electrons to introduce additional channel resistance [3]. Such coupled phenomena have been included in the description of an actual MOSFET through accurate physics-based modeling.

Previous research in our lab has resulted in the development of a 2D-device simulator for 4H-SiC devices [49, 50, 51, 52]. Accurate models for the density of interface traps ( $D_{it}$ ) and Coulomb scattering mobility have been developed for use in the device simulator [3, 49, 50]. Essentially, the simulator determines the current-voltage characteristics of a device by solving the drift and diffusion equations self-

consistently. Various other scattering mechanisms like surface roughness, surface phonons etc. have also been incorporated into the simulator [49, 52].

The advantage of such simulators is that they could be used to predict device behavior accurately without the knowledge of exact atomic make-up of the interface. For example, they have been used to study the high-temperature behavior and energy and time dependent dynamics of interface trap occupation in 4H-SiC MOSFETs [3, 51]. I will describe the 2D-device simulator in detail in the next chapter.

## Chapter 2: Modeling Tools and techniques

In this chapter, I will describe the details of important methodologies like drift-diffusion simulations and density functional theory which are extensively employed in this Ph.D. work. I will also elaborate on the nuts-and-bolts of other techniques like molecular dynamics, nudged elastic band method, and amorphous silica model generation to set a background for the forthcoming chapters in this thesis. Finally, I will outline the general computational set up for density functional calculations performed in this work. In short, this chapter is intended to provide a background on various modeling techniques employed in this work.

I begin with a description of the drift-diffusion simulations for solving the terminal characteristics of a 4H-SiC power MOSFET shown in Figure 1.1. Models pertaining to different scattering mechanisms (mobility), interface traps, and the Generation-Recombination (G-R) rates are also presented.

### 2.1 Drift-Diffusion Simulations

The terminal characteristics of semiconductor devices can be determined in detail by simultaneously solving the semiconductor equations numerically. The system of semiconductor equations constitute

$$\nabla^2 \varphi = -\frac{q(p - n + N_D - N_A)}{\varepsilon} \quad (2.1)$$

$$\mathbf{J}_n = -q\mu_n n \nabla \varphi + qD_n \nabla n \quad (2.2)$$

$$\mathbf{J}_p = -q\mu_p p \nabla \varphi - qD_p \nabla p \quad (2.3)$$

$$\frac{\partial n}{\partial t} = \frac{1}{q} \nabla \cdot \mathbf{J}_n + G_n - R_n \quad (2.4)$$

$$\frac{\partial p}{\partial t} = -\frac{1}{q} \nabla \cdot \mathbf{J}_p + G_p - R_p \quad (2.5)$$

$$\frac{D}{\mu} = \frac{kT}{q} \quad (2.6)$$

where equation (2.1) is the Poisson's equation, equations (2.2) and (2.3) are the electron and hole current equations, equations (2.4) and (2.5) are the electron and hole continuity equations and equation (2.6) is the Einstein's relation. The symbols have their usual meanings, with  $G$  and  $R$  representing electron or hole generation and recombination rates. By substituting equations (2.4) and (2.5) in (2.2) and (2.3), we can reduce the number of independent equations in the system to three. The three unknown quantities involve the potential ( $\phi$ ), electron concentration ( $n$ ) and hole concentration ( $p$ ). The terminal I-V characteristics of a device can be calculated by solving the system of these equations self-consistently. Typically, the equations are solved simultaneously and self-consistently using the iterative Newton's method, under the Scharfetter-Gummel discretization scheme for the electron/hole current-continuity equation. Further details on the methodology could be obtained from Ref. [53].

A critical aspect here is the models relating to electron and hole mobility and their generation and recombination rates. Mobility is a complex phenomenon arising from scattering of carriers. In order to model total mobility, we consider individual mobilities separately and calculate the net mobility using Matthiessen's rule, as will be described later. Various components of mobility considered in this work include those arising from surface roughness scattering, surface and bulk phonon scattering and Columbic scattering from trapped interface charges, impurities and fixed oxide

charges. Trap-assisted Generation and Recombination (G-R) of electron-hole pairs are described by Shockley-Reed-Hall and Auger theory. Apart from these, other physical phenomena like impact ionization, interface state occupation and velocity saturation need to be incorporated into the equations for accurate determination of I-V characteristics. Good models will also have to build in temperature dependence of parameters like mobility, bandgap, etc. The physical models that encapsulate these mechanisms are described later in this chapter.

Previous research in my lab has resulted in the development of a 2D-device simulator that solves the system of semiconductor equations and calculates the I-V characteristics of 4H-SiC devices [3, 49, 50, 51, 52]. This helps in probing the device in such great detail that experiments are unable to. Accurate models have been developed for mobility, recombination-generation, interface trap distribution, impact ionization and temperature effects [52]. These models have been validated by comparing simulated I-V characteristics with experimental ones for different temperatures [49, 50, 51]. Thus, the 2D-device simulator serves as an important tool to achieve the research goals mentioned in Chapter 1.

Various well-established models for mobility and G-R rates, which are embedded into the in-house 2-D device simulator, are described below.

### 2.1.1 Mobility Models

Here, I briefly introduce various scattering mechanisms and associated mobility models considered in the in-house 4H-SiC device simulator. This is intended to set a background for understanding the device simulator, and hence I do not describe the

details of various parameters. However, such information can be gathered from Ref [53].

The bulk mobility ( $\mu_B$ ) of electrons in 4H-SiC power MOSFETs due to phonon scattering and ionized impurity scattering is modeled as (Caughey-Thomas model).

$$\mu_B(T) = \frac{\mu_{max} \left(\frac{300}{T}\right)^\alpha - \mu_{min}}{1 + \left(\frac{D}{N_{ref}}\right)^\beta} + \mu_{min} \quad (2.7)$$

Here,  $D$  represents the doping concentration in the bulk region. Expectedly, the bulk mobility can be seen to decrease with increasing temperature or doping concentration.  $\mu_{max}$  represents the intrinsic bulk mobility at room temperature.  $\mu_{min}$  denotes the minimum bulk mobility.  $\alpha$  is a temperature dependent parameter, and  $\beta$  and  $N_{ref}$  are doping dependent parameters.

The effect of surface acoustic phonon scattering at the interface is encapsulated in the following mobility model that invokes deformation potentials ( $D_{ac}$ ).

$$\mu_{SP}(T) = \frac{A}{E_\perp} + \frac{B}{T(E_\perp)^{\frac{1}{3}}} \quad (2.8)$$

The surface phonon mobility is a function of the perpendicular component of the electric field and temperature. Here, A and B are given using the following expressions.

$$A = \frac{3 \hbar^3 v_s^2 \rho_{bulk}}{2 m^* m_c D_{ac}^2} \quad (2.9)$$

$$B = \left\{ \frac{q \hbar^3 v_s^2 \rho_{bulk}}{m^* m_c D_{ac}^2 k_b} \right\} \left\{ \frac{9 \hbar^2}{4 q m_\perp} \right\}^{1/3} \quad (2.10)$$

Here,  $m^*$ ,  $m_c$ , and  $m_\perp$  respectively represent the 2D-density of states effective mass, the conductivity effective mass, and perpendicular effective mass.  $v_s$  and  $\rho_{bulk}$

denote the velocity of sound and bulk 4H-SiC density. Other symbols have their usual meanings.

As mentioned in the previous chapter, very high density of interface traps has been typically observed in 4H-SiC MOSFETs. These defect centers not only trap carrier electrons, but also scatter them through Coulomb scattering. A model was developed in my lab previously to account for the presence of charged scattering centers at and/or near the interface [3]. This Coulomb mobility ( $\mu_c$ ) model was included in the device simulator, and is given below.

$$\mu_c(T) = \left\{ \frac{16 \pi \varepsilon^2 \hbar k_b T}{m^* q^3 (N_{it} + N_{ot})} \right\} \left( \frac{1}{F(z, z_i, T)} \right) \quad (2.11)$$

Here  $N_{it}$  and  $N_{ot}$  represent the number of charged interface traps and fixed oxide traps, respectively.  $\varepsilon$  is the dielectric constant of 4H-SiC and  $k_b$  is the Boltzmann's constant. The function  $F$  account for depth-dependent screening effects, and is detailed in Ref [3].

The scattering of free carriers due to surface roughness at the 4H-SiC/SiO<sub>2</sub> interface is calculated in detail in Ref. [53] using the Fermi's Golden rule (with a rectangular perturbation potential). The surface is envisaged to be composed of triangular steps of height  $\Delta$  that repeats after length  $L$ . The surface roughness mobility, which depends on the perpendicular electric field  $\mathbf{E}_\perp$ , is given as

$$\mu_{SR}(T) = \left( \frac{1}{(E_\perp(z))^2} \right) \left\{ \frac{\hbar^3}{2 q m_c m^* \Delta^2 L^2} \right\} \left( \frac{1}{\Omega_{SR}} \right) \quad (2.12)$$

Clearly, the extent of scattering due to surface roughness depends on the depth at which the free carriers are located from the 4H-SiC/SiO<sub>2</sub> interface. Further details

regarding the derivation of surface roughness mobility and its implementation in the device simulator is provided in Ref. [53].

The mobility of carriers at high lateral electric fields ( $E_{\parallel}$ ) is provided in terms of the saturation velocity ( $v_{sat}$ ). The Thornber's model, which estimates the net field-dependent mobility, is given below. Here, the subscript  $LF$  stands for Low Field, and  $\delta$  is a field-dependent parameter.

$$\mu_{field}(T) = \frac{\mu_{LF}(T)}{\left\{ 1 + \left( \frac{\mu_{LF}(T) E_{\parallel}}{v_{sat}(T)} \right)^{\delta} \right\}^{1/\delta}} \quad (2.13)$$

In a 4H-SiC power MOSFET, all the scattering mechanisms (or mobility) described above are simultaneously in action. However, their relative dominance is a strong function of the operating conditions of the device (like electric field, temperature, doping etc.). The total mobility arising from these individual mechanisms is calculated using Matthiessen's rule, which is mathematically stated below.

$$\frac{1}{\mu_{tot}} = \frac{1}{\mu_B} + \frac{1}{\mu_{SP}} + \frac{1}{\mu_C} + \frac{1}{\mu_{SR}} + \frac{1}{\mu_{field}} \quad (2.14)$$

In the device simulator, the total mobility appearing in the current equations are calculated using the above equation. Thus, the accuracy of the simulator is critically dependent on the validity of individual mobility models.

### 2.1.2 Generation-Recombination Models

The drift-diffusion simulator developed in my lab estimates the Generation-Recombination rates for holes and electrons (appearing in the continuity equations

(2.4) and (2.5)) using the Shockley-reed-Hall (SRH) and Auger models. According to the SRH model, the G-R rates for electrons/holes in the presence of traps is given by,

$$(G - R)_{SRH} = \frac{np - n_i^2}{\tau_p (n + n_i) + \tau_n (p + n_i)} \quad (2.15)$$

where  $\tau_p$  and  $\tau_n$  represent the minority carrier lifetimes of holes and electrons, respectively (which are typically a few hundred nanoseconds long in 4H-SiC). Other symbols have their usual meanings. The SRH recombination rates in Silicon Carbide are expected to be very small, mainly due to its wide bandgap.

On the other hand, Auger recombination represents the direct recombination between a conduction band electron with a valence band hole. Here, the momentum is conserved by its transfer to a third particle which could be an electron or a hole. Since 4H-SiC is an indirect bandgap material, the probability of such direct band-to-band recombination is very low. However, this model is built in to the simulator using the following expression.

$$(G - R)_{Auger} = (np - n_i^2)(C_n n + C_p p) \quad (2.16)$$

Here,  $C_n$  and  $C_p$  are coefficients of interaction with the third particle, which could be an electron or a hole.

## 2.2 A Brief Introduction to Density Functional Theory

In this section, I present a brief introduction to the basics of Density Functional Theory (DFT). For a more extensive account, the reader is referred to Ref. [54], or other similar dedicated books on DFT.

The electronic properties of a semiconductor (for example, its band structure) are derived in principle by solving the fundamental multi-body Schrodinger wave

equation (SWE). For a crystal with M atoms and N electrons, the total Hamiltonian is given as

$$\begin{aligned} & \hat{H}\psi(x_1, y_1, z_1, \dots, x_N, y_N, z_N, x'_1, y'_1, z'_1, \dots, x'_M, y'_M, z'_M) \\ & = E\psi(x_1, y_1, z_1, \dots, x_N, y_N, z_N, x'_1, y'_1, z'_1, \dots, x'_M, y'_M, z'_M) \end{aligned} \quad (2.17)$$

where the Hamiltonian operator  $\hat{H}$  is given as,

$$\begin{aligned} \hat{H} = & -\frac{1}{2} \sum_{i=1}^N \nabla_i^2 - \frac{1}{2} \sum_{j=1}^M \frac{1}{M_j} \nabla_j^2 - \sum_{i=1}^N \sum_{j=1}^M \frac{Z_j}{r_i - r_j} + \frac{1}{2} \sum_{i=1}^N \sum_{k=1}^N \frac{1}{r_i - r_k} \\ & + \frac{1}{2} \sum_{j=1}^M \sum_{j'=1}^M \frac{1}{r'_j - r'_{j'}} \end{aligned} \quad (2.18)$$

In the above Hamiltonian, the first two terms represent the kinetic energies of electrons ( $T$ ) and nuclei. The third term is for the attractive potential energy between nuclei and electrons ( $V_{ne}$ ). The last two terms account for the repulsive electron-electron ( $V_{ee}$ ) and nucleus-nucleus ( $V_{nn}$ ) interactions. The Hamiltonian is in atomic units which sets the coefficients of the kinetic energy and potential energy operators to one. As is evident from equation (2.17), the total wavefunction has  $3N+3M$  degrees of freedom making the simplification of the problem necessary to solve it.

The first simplification that can be made is called the Bonn-Oppenheimer approximation. Because the nuclei are much heavier than the electrons, their kinetic energy terms can be neglected in the Hamiltonian, In other words, nuclear motions are much slower that they can be treated as static. The potential energy due to the nuclei can be separately calculated by considering them as classical charges. Thus, we are only interested in the multi-particle electronic Hamiltonian henceforth. This is given as

$$\widehat{H}_{elec} = -\frac{1}{2} \sum_{i=1}^N \nabla_i^2 - \sum_{i=1}^N \sum_{j=1}^M \frac{Z_j}{r_i - r_j} + \frac{1}{2} \sum_{i=1}^N \sum_{k=1}^N \frac{1}{r_i - r_k} \quad (2.19)$$

So far, we have reduced the problem by considering electrons to move in the sum of a static field created by fixed nuclei and a mean field created by other electrons. The electronic energies can be obtained by the eigenvalues of the electronic Hamiltonian and total energy of the system can be calculated by adding nuclear potential energy (calculated separately) to electronic energy.

Solving the above quantum mechanical problem would lead to a situation where one deals with  $3N$  variables in the total electronic wavefunction. This is the traditional Hartree-Fock approach used in Chemistry for studying isolated molecules. However, for a large material system, such an approach is extremely demanding. Density Functional Theory (DFT) provides formalism that enables one to solve the problem through electron density,  $n(r)$ , and reduced the number of variables to three. Fundamentally, the electron density is defined as the square of the total electron wavefunction. This enormous simplification has made DFT a popular tool for analyzing material systems in recent years.

The electronic Hamiltonian in equation (2.19) has more subtleties involved. What is explicitly not shown is the effect of Pauli's exclusion. This effect is difficult to model and impact the total kinetic energy of the interacting system. One way of looking at it is as the introduction of additional repulsive potential energy term in the Hamiltonian since Pauli's exclusion prevents two electrons of same spin from being in the same region of space. In DFT, the energy resulting from Pauli's exclusion is classified as exchange energy. Similarly, the component of energy that arises from the

correlated movement of interacting electrons is not explicitly seen. This is called correlation energy. However, it is worth noting that equation (2.19) is exact until this point of discussion (without any approximation).

As mentioned before, DFT revolves around electron density as opposed to the actual  $3N$ -variable wavefunction. DFT is based on the theorems proposed by Hohenberg, Kohn and Sham, which are described briefly in the following sections.

The first Hohenberg-Kohn theorem states that the ground state energy of a multi-body system (equation 2.17) is a unique functional of the electron density,  $n(r)$ . In other words, the electron density uniquely determines ground state properties like wavefunctions, energy and the external potential.

The second Hohenberg-Kohn theorem predicts an important property of the energy functional. It states that the ground state energy can be obtained by minimizing the functional with respect to electron density function. Thus, the electron density that minimizes the functional corresponds to the true ground state electron density and the corresponding energy is the true ground state energy. This minimization can be achieved through variational principles.

Unfortunately, while the two theorems collectively predict the existence of an energy functional in terms of the electron density and the method to calculate the ground state energy from it, they do not provide the exact form of the functional. Here is where the Kohn-Sham formalism-based DFT comes into play.

In the Kohn-Sham formulation, the system of  $N$  interacting electrons is replaced by a system of  $N$  non-interacting electrons. This allows the energy functional to be defined as

$$E[n(r)] = T_{non\_int}[n(r)] + \int V_{ion} n(r)dr + E_H[n(r)] + E_{xc} \quad (2.20)$$

The various terms in the equation and their relevance are mentioned below.

The external potential due to atomic nuclei and core electrons,  $V_{ion}$ , is typically modeled using pseudopotentials in DFT calculations. They are representative potentials defined in such a manner that they coincide with the actual potential as we approach the valence electrons from the nucleus (for  $r > r_{cut}$ ). Such pseudopotentials are developed after rigorous optimization and validation. The key advantage of pseudopotentials is that they enable one to perform DFT calculations by including a computationally manageable set of basis functions in the total wave function.

Another major advantage of Kohn-Sham system is that it allows the Kinetic energy to be written as the sum of individual electronic kinetic energies (as electrons are non-interacting, with a single-particle wavefunction  $\psi_i$ ).

$$T_{non\_int}[(n(r))] = -\frac{1}{2} \sum_{i=1}^N \langle \psi_i | \nabla_i^2 | \psi_i \rangle \quad (2.21)$$

Similarly, the potential energy term,  $E_H$ , simply reduces to the classical mean field term (called the Hartree potential).

$$E_H[n(r)] = \frac{1}{2} \iint \frac{n(r')n(r)}{r - r'} dr dr' \quad (2.22)$$

All the other “unknown” quantum effects and self-interaction energy are lumped into a third term called the exchange correlation term. This is given as

$$E_{xc} = T_{real} - T_{non\_int} + E_{eereal} - E_H \quad (2.23)$$

The major challenge in Kohn-Sham DFT is the accurate representations of  $E_{xc}$ . Approximate methods for calculating exchange-correlation involve Local density Approximation (LDA) and Generalized Gradient Approximation (GGA).

Now that the Kohn-Sham ansatz has provided us with the ‘elusive’ energy functional predicted by Hohenberg-Kohn theorems, we can use variational methods to minimize the functional with respect to electron density and arrive at the ground state properties. The main challenge is in the identification of accurate exchange-correlation energy.

For the minimization of energy functional based on variational principles, we define a functional,  $G(n(r), \mu)$ , as

$$\left[ E[n(r)] - \mu \left( \int n(r) dr - N \right) \right] = G(n(r), \mu) \quad (2.24)$$

In the above equation, the constraint used for minimization is that the integral of electron density over volume is equal to the number of electrons.  $\mu$  represents the Lagrange multiplier. Using Lagrange multiplier optimization method, we get

$$\mu = \frac{\delta E[n(r)]}{\delta n(r)} \quad (2.25)$$

Here,  $\delta$  represents derivative with respect to a function; in this case  $n(r)$ . In other words, from equation 2.20 and 2.25,

$$\mu = \frac{\delta T_{nonint}[n(r)]}{\delta n(r)} + V_{KS} \quad (2.26)$$

where, the Kohn-Sham potential  $V_{KS}$  is

$$V_{KS} = V_{ion} + V_H + \frac{\delta E_{xc}}{\delta n(r)} \quad (2.27)$$

$V_H$  is the classical Hartree potential obtainable from the Poisson equation, and is given as

$$V_H = \frac{\delta E_H}{\delta n(r)} = \int \frac{n(r')}{r - r'} dr \quad (2.28)$$

Thus, equation (2.26) will leave us with a single particle Schrodinger-like wave equation called the Kohn-Sham equation. To reiterate, this is the equation for the particles in the non-interacting Kohn-Sham system, whose electron density equals that of the real system. For a crystal system, the ‘Schrodinger-like’ Kohn-Sham equation in (2.29) can be solved using Bloch theorem by exploiting the crystal periodicity.

$$-\left(\frac{1}{2}\nabla^2 + V_{KS}\right) \psi_i = \varepsilon_i \psi_i \quad (2.29)$$

This method of DFT, where we use plane wave basis functions in combination with Bloch’s theorem, is typically used for material systems involving solids. This is henceforth called the plane-wave Density Functional Theory (pw-DFT). Fundamentally, the solutions of equation (2.29) are calculated using the well-known ‘central method’, which is described in many graduate-level text-books in solid state physics [55].

In practice, we begin by an initial guess of electron density. The idea is to solve Kohn-Sham equations self-consistently to obtain the electron density and external potential. Evidently, the ground state electron density is calculated from the square of Kohn-Sham wave functions,  $\psi_i$ .

$$n(r) = 2 \sum_i \psi_i^* \psi_i \quad (2.30)$$

A brief summary of the Kohn-Sham DFT is provided as a flowchart in Figure 2.1.

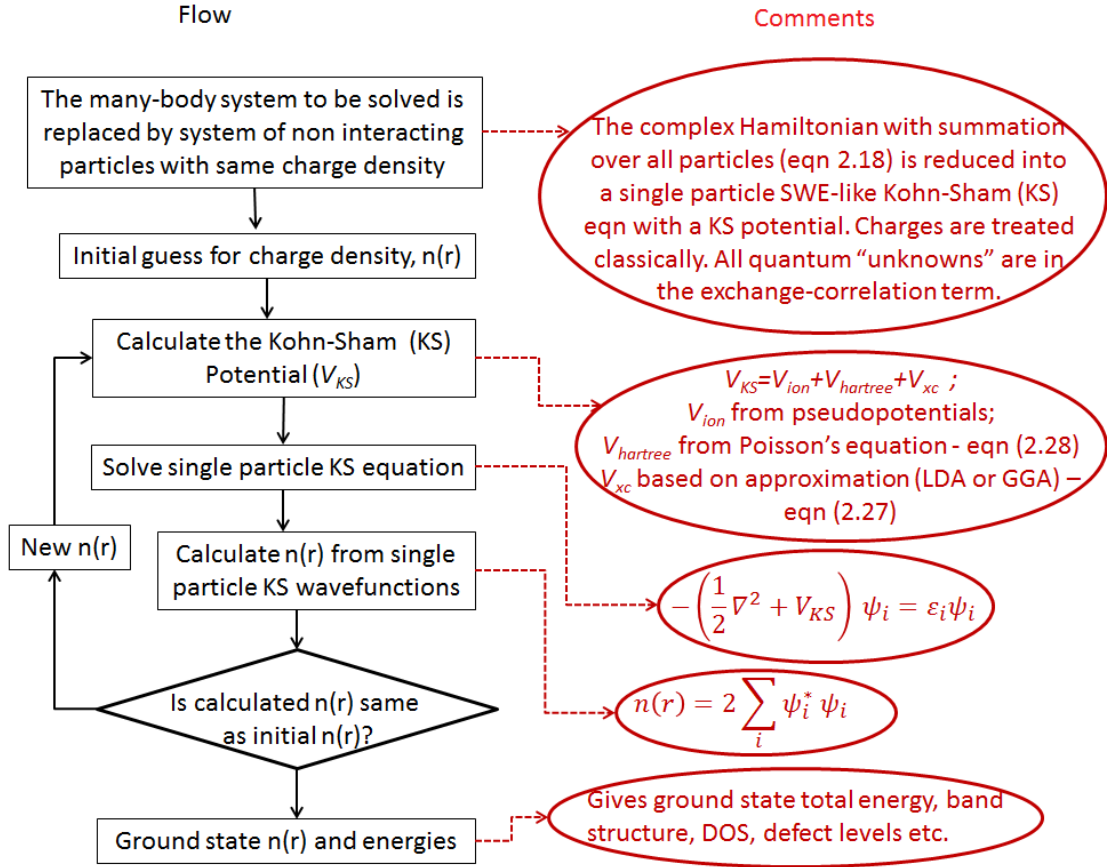


Figure 2.1: A summary of Kohn-Shan Density Functional Theory as a flow chart.

In this work, I will use plane-wave density functional theory, as implemented in the open software Quantum Espresso [56], to study the electronic properties of mobility and reliability-limiting defects in 4H-SiC MOS systems.

In the following sections, I continue my presentation on various techniques of analyses that are based on DFT. This includes Quantum Molecular Dynamics and Nudged Elastic Band methods.

## 2.3 Quantum Molecular Dynamics

Quantum Molecular Dynamics (QMD) is a technique used to study the time-evolution of atomic motion in a material system [54]. Here, the forces acting on individual atoms (say,  $i$ ) in a configuration (or material system) at a given instant is calculated from the gradient of its ground state energy ( $E$ ) (equation 2.20).

$$F_i = -\frac{\partial E}{\partial R_i} \quad (2.31)$$

where  $R_i$  is the coordinates of the  $i^{\text{th}}$  atom. The force calculation is typically implemented using Hellman-Feynman theorem [54].

Subsequently, the atoms in the system are moved based on the forces acting on them, according to classical mechanics, using the Verlet algorithm described below.

The equation of motion is given as [54],

$$M_i \frac{d^2 R_i}{dt^2} = F_i \quad (2.32)$$

The left-hand side of the above equation is discretized in time. The new coordinates of the atoms in the system after a time interval  $\Delta t$  (typically, a couple of femtoseconds) is calculated as,

$$R_i(t + \Delta t) = 2R_i(t) + R_i(t - \Delta t) + \frac{(\Delta t)^2}{M_i} F_i \quad (2.33)$$

The forces acting on the new configuration is then re-calculated using the Hellman-Feynman theorem, and the process is repeated for the desired time scale.

In DFT-based molecular dynamics, the effect of temperature could be introduced externally using feedback loops. One such method is velocity rescaling. Here, the kinetic energy (equivalently, the velocity) of the atoms is repeatedly rescaled to

match its thermal energy at a specified temperature after every given number of QMD iterations. Several other techniques also exist to maintain a constant temperature in QMD.

Applications of the QMD method include analysis of chemical reactions and diffusion mechanisms. It could also be used to generate realistic models of material systems for DFT analysis. These applications would be further explained in the later sections of the dissertation. However, it is worth mentioning that QMD is extremely computationally intensive.

## 2.4 Minimum Energy Pathway Calculations

Nudged Elastic Band (NEB) method provides a formalism to determine the Minimum Energy Pathway (MEP) between two minimum energy (stable) atomic configurations on a Potential Energy Surface (PES) [57]. The MEP is defined as the lowest energy pathway that could rearrange the atomic configuration of the initial stable state to form the final stable state. The saddle point maximum of the MEP with respect to the initial minimum gives a measure of the activation barrier within the transition state theory. The MEP on a PES is indicated in Figure 2.2. In this work, I used NEB to calculate the Arrhenius activation barriers for processes like chemical reactions, diffusion and structural transformations in solids.

In the NEB method, the initial and final atomic configurations of the process under study are first identified through structural relaxations. Subsequently, an initial guess of the intermediate configurations (or images) that constitute the MEP chain is calculated by linear interpolation between the two end states (Figure 2.2). Here, each adjacent image is assumed to be connected through a spring, analogous to a chain of

equally spaced mass-spring system. MEP is calculated by minimizing the force of the chain of images through DFT-based structural relaxations (eventually leading to the deformation of the initial chain). The perpendicular component of the force vanishes for the MEP on a potential energy surface (Figure 2.2).

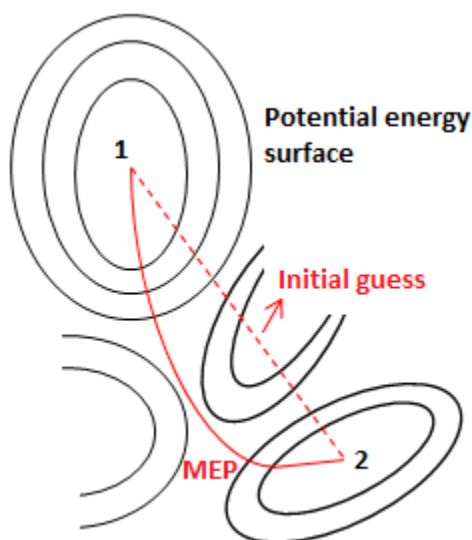


Figure 2.2: A schematic illustration of the minimum energy pathway (MEP) between two stable states on a potential energy surface (PES). The dotted line indicated the initial guess in a NEB calculation.

Clearly, the total force acting on a spring-mass chain on a potential energy surface is the sum of the spring force and the gradient of the potential. This force need to be minimized to calculate the MEP. However, this straight-forward force minimization has been observed to fail to identify the saddle point, mainly because the perpendicular component of the spring force pulls the pathway off the saddle point. Additionally, the parallel component of the true force (due to PES) makes the saddle point configuration to ‘slide off’. This difficulty is overcome in the NEB method by

considering only the parallel component of the spring force and the perpendicular component of the true force in the algorithm. Thus, the force on an image ( $\vec{F}_i$ ) in the NEB method is defined as,

$$\vec{F}_i = -\vec{\nabla}V(R_i)_{perp} + (\overline{F}_i^{spr} \cdot \hat{r}) \hat{r} \quad (2.34)$$

Here, the first term is the perpendicular component of the true force, and the second term is the parallel component of the spring force.  $V(R_i)$  represents the potential energy, and  $R_i$  represents the atomic configuration for the  $i^{th}$  image.  $\hat{r}$  is the unit vector in the direction parallel or tangential to the path.

In equation (2.34), the perpendicular component of the true force is calculated by subtracting the parallel component of the true force from the total true force, as given below.

$$\vec{\nabla}V(R_i)_{perp} = \vec{\nabla}V(R_i) - (\vec{\nabla}V(R_i) \cdot \hat{r}) \hat{r} \quad (2.35)$$

Additionally, the spring force on the  $i^{th}$  image is calculated as,

$$\overline{F}_i^{spr} = k_{i+1}(R_{i+1} - R_i) - k_i(R_i - R_{i-1}) \quad (2.36)$$

where  $k_i$  denotes the spring constant of the  $i^{th}$  spring. However, in this work, all the springs are considered to be the same.

The nudged elastic band method minimizes the force  $\vec{F}_i$  in equation (2.34) using DFT-based structural relaxations. The perpendicular component of the force acting on the images reduces to zero as the NEB force is completely minimized, resulting in the determination of the minimum energy pathway, saddle point and the activation barrier of the physical process.

## 2.5 Methodologies for Generating Amorphous Silica Models

In order to study the properties of a material system using plane-wave Density Functional Theory, it is very important to have a realistic model of the material in the first place. Such models, on which the plane-wave DFT is applied under the periodic boundary conditions, are called ‘supercells’. While larger supercells provide more accurate results, they make the computational resources to scale up dramatically. Thus, the idea here is to generate a supercell of reasonable size (strategies for determining this will be discussed later) that is physically as close to the actual material system as possible.

In the following chapters of this dissertation, I will consider three material systems for DFT analysis. They are a) bulk  $\text{SiO}_2$ , b) bulk 4H-SiC and c) 4H-SiC/ $\text{SiO}_2$  interface. Bulk 4H-SiC is crystalline. Hence, its model is ‘deterministic’, and could be directly generated. However, the oxide structure in a MOSFET is amorphous. Thus, bulk  $\text{SiO}_2$  and the interface model generation require the use of special methods like Monte-Carlo bond-switching or melt-and-quench molecular dynamics.

In the past, realistic models of amorphous silica supercells were typically generated using molecular dynamics (MD) [58, 59] or the Monte-Carlo (MC) bond-switch method (Wooten-Winer-Weaire (WWW) algorithm [60, 61]). In this work, I have used two methods to generate amorphous silicon dioxide models. The first method, which I call the ‘Sequential Back-bond break (SBB)’ method, is fundamentally a variant of the MC bond-switch method. The second method is the conventional molecular dynamics method. I explain both the methods in further detail in the following sections.

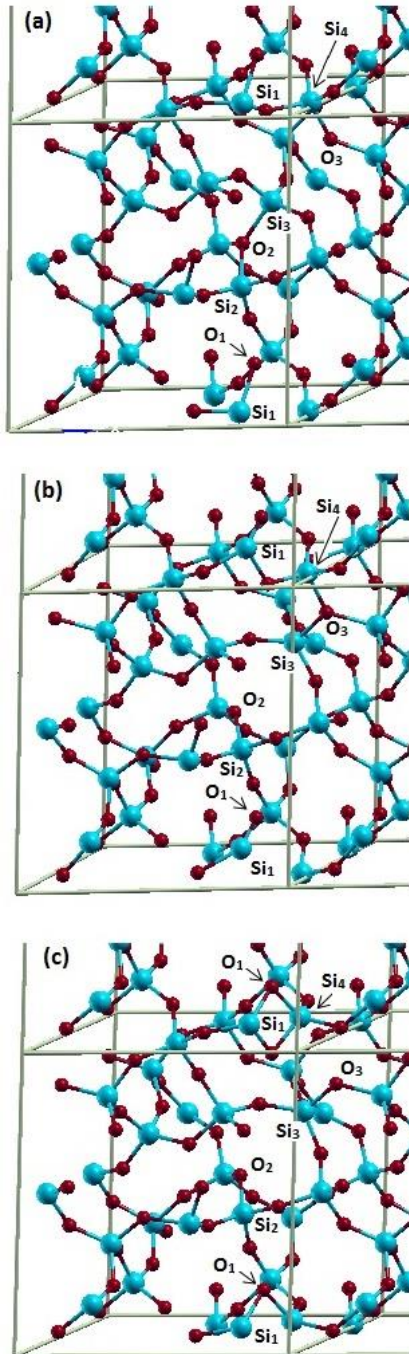


Figure 2.3: (a) Step 1, (b) Step 2, and (c) Step 3, in an iteration of the Sequential Back-bond Break methodology for generating 72-atom amorphous  $\text{SiO}_2$  model. The individual atoms involved in the iteration are indicated. Each supercell in the periodic array is enclosed within the box marked by solid lines.

### 2.5.1 Sequential Back-bond Break Method

The Sequential Back-bond break method presents a novel methodology for generating amorphous silica models. The method works by exploiting the inherent periodicity of  $\text{SiO}_2$  supercells used in plane-wave DFT calculations. I explain this using a 72-atom  $\text{SiO}_2$  supercell. The steps involved in a single iteration of the methodology are also schematically represented in Figure 2.3.

- 1) I begin with a 72-atom supercell of  $\alpha$ -quartz, the properties of which are adopted from Ref. [62]. I randomly select a  $\text{Si}_1\text{-O}_1\text{-Si}_2$  linkage, which is then broken between  $\text{O}_1$  and  $\text{Si}_2$  (Figure 2.3(a)). (Here, the subscripts are labels to the O and Si atoms in the supercell of Figure 2.3.) This is achieved by appropriately puckering the  $\text{Si}_2$  atom (by  $\sim 1.6 \text{ \AA}$ ) to backbond with a lattice oxygen ( $\text{O}_2$ ), making it triply coordinated as shown in Figure 2.3(a). However,  $\text{O}_1$  is left dangling from  $\text{Si}_1$ .
- 2) One of the two ‘original’ bonds of the triply coordinated  $\text{O}_2$  atom - in this case,  $\text{O}_2\text{-Si}_3$  - is then broken by puckering  $\text{Si}_3$  as shown in Figure 2.3(b). This forms a new triply coordinated oxygen atom, labelled  $\text{O}_3$  (Figure 2.3(b)).
- 3) In Figure 2.3(c), one of the ‘original’ bonds of  $\text{O}_3$ , namely  $\text{O}_3\text{-Si}_4$ , is shown to be broken through  $\text{Si}_4$  puckering. Owing to the periodicity of the supercell, puckered  $\text{Si}_4$  would bond with the dangling  $\text{O}_1$  atom from step 1 forming  $\text{Si}_1\text{-O}_1\text{-Si}_4$  linkage and repairing the damage caused by initial bond breaking. This maintains the local coordination of Si and O atoms.
- 4) The resultant geometry is relaxed using DFT-based energy minimization.

5) Steps 1 to 4 are repeated for a different Si-O-Si linkage for further amorphousness.

The propagation of the triply coordinated oxygen in this process was constrained to be directional to ensure efficiency of the algorithm. In this dissertation, the above methodology was implemented by visual inspection, owing to the relatively small size of the SiO<sub>2</sub> supercell (72 atoms) considered.

The structural properties such as bond angles and bond lengths were analyzed in a representative sample and were found to be in excellent agreement with amorphous models generated previously using MD [58]. This is given in Figure 2.4. The initial result on the calculated partial pair-correlation function, which is given in Figure 2.5, is also in reasonable agreement with previous reports [59, 63].

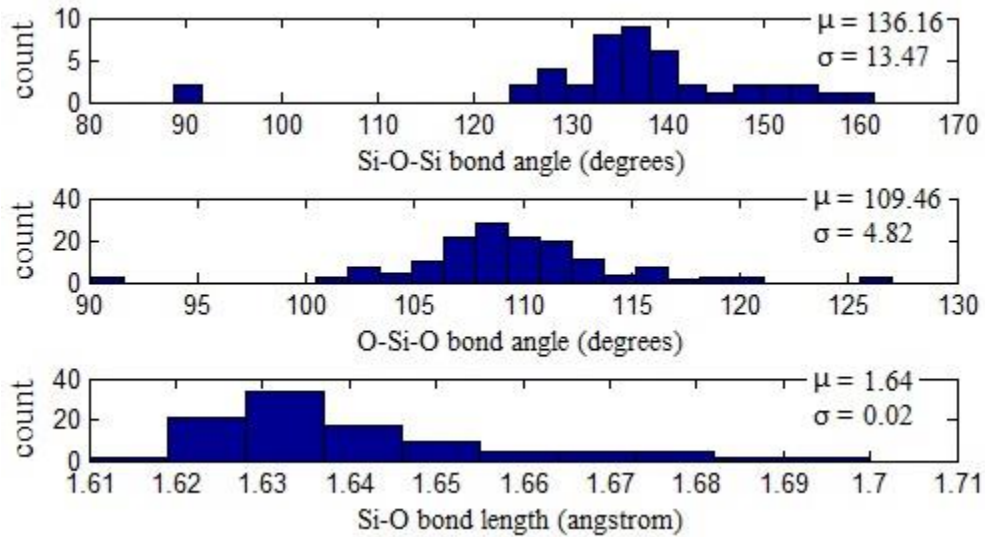


Figure 2.4: The bond angle and bond length distributions in a representative amorphous SiO<sub>2</sub> model generated using the SBB method. The isolated bond angle data points originate from two-membered rings.

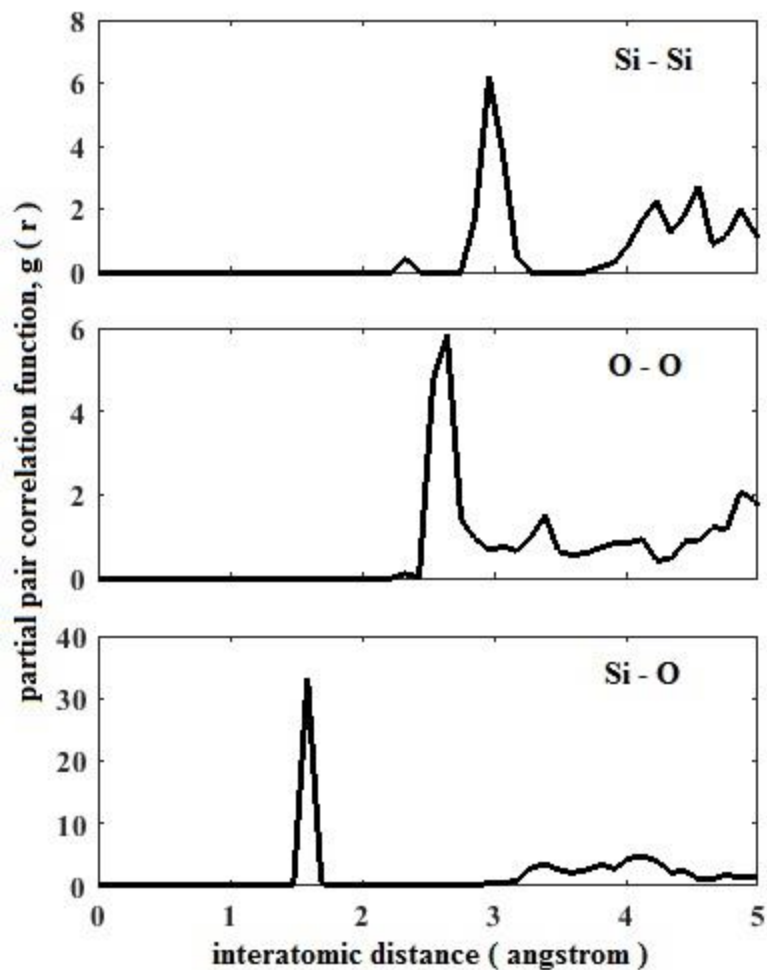


Figure 2.5: The calculated partial pair correlation function for the amorphous SiO<sub>2</sub> model generated using the SBB method.

Expectedly, the SiO<sub>2</sub> models generated using this methodology had Si-O bonds reorganized or ‘switched’ in comparison with crystalline  $\alpha$ -quartz. Thus, they were observed to have higher ground state energies, and represent higher degree of disorder (with respect to crystalline  $\alpha$ -quartz). In the rest of the paper, I refer to these supercell models as Type 1 models.

Traditional Monte-Carlo bond-switch algorithms like the WWW algorithm scan a large part of the configuration energy space before settling into a local minima based

on Metropolis criterion. This could be very time consuming. Additionally, the implementation of inter-ion interaction potential model could have inaccuracies. In the SBB method, we generate a configuration with a low energy, without having to search the entire energy space. This is because we begin from the most stable  $\alpha$ -quartz configuration, and arrive at a realistic local minimum after a few SBB iterations. Here, the structural optimizations are performed using first principles, overcoming the need for empirical inter-ion potentials.

It can be argued that the complete randomization in the structure would be eventually achieved (without any ‘memory’ of the original  $\alpha$ -quartz), after sufficient number of iterations. Thus, SBB method is expected to overcome the inaccuracies related to inter-atomic potentials in WWW method, and be faster. A computer implementation of this method, which is expected to be much faster than traditional WWW algorithm, for larger supercells needs to be developed in future. Additionally, further validation of this method is required with the help of much larger models of amorphous silica.

### 2.5.2 Melt-and-Quench Molecular Dynamics

The alternative methodology used in this dissertation for amorphous oxide model generation involves first-principles molecular dynamics, which was described in Section 2.3. This method, called the melt-and-quench technique, is outlined below.

I begin my QMD simulation by melting a 72-atom  $\alpha$ -quartz model at 4000K for 1ps. A time-step of 2fs was used in the Verlet’s algorithm for atomic displacements. After one pico-second, the model was rapidly quenched (cooled) to 3000K, where the system was further allowed to evolve in time for an additional pico-second. This

sequence of rapid quenching followed by a pico-second long time-evolution was progressively carried out at temperatures 2000K, 1000K and 300K. At the end of the complete process which lasted for 5ps, I arrived at a 72-atom amorphous silica model.

In the models generated using this method, the Si and O atoms were seen to be displaced from their corresponding  $\alpha$ -quartz positions, but without any bonding rearrangement [64]. I envisage such models, with lower ground state energies, to represent the less amorphous regions of a-SiO<sub>2</sub>. They are henceforth designated as Type 2 models.

The density of a-SiO<sub>2</sub> models used here in the context of 4H-SiC MOSFETs is  $\sim 2.65\text{g/cm}^3$ . This is higher than the typical density of amorphous SiO<sub>2</sub> ( $\sim 2.1\text{-}2.4\text{g/cm}^3$ ) [58, 65]. I justify the higher oxide density used in this work using the following argument: The areal density of Si atoms on the (0001) plane in 4H-SiC is higher than that of (100) plane in Silicon. Thus, the near-interfacial oxide in 4H-SiC MOSFETs, where the border oxygen vacancies addressed in this work are likely to exist, is envisaged to be denser than the oxide grown on Silicon. Experimental data related to the exact density of such border regions in 4H-SiC MOSFETs is not available to my knowledge.

## 2.6 Computational Setup

In this work, I have used Quantum Espresso package [56] to carry out plane-wave DFT simulations. The details of the computational setup used in this work are given below.

The defects in a-SiO<sub>2</sub> were simulated using 72-atom models, unless explicitly stated otherwise. The plane-wave basis functions with energies up to 1900 eV were

included in the calculations, with the Brillouin zone sampled at the Gamma point. The effect of core electrons (or the ionic potentials) was brought in through norm-conserving pseudopotentials [66]. The ground state energy was ensured to converge for the above setup. The exchange-correlation energy, discussed in Section 2.2, was approximated using the Generalized Gradient Approximation (GGA) under the Perdew-Burke-Ernzerhof (PBE) scheme [67].

However, the PBE scheme is well-known to underestimate the bandgap of the material system under consideration [68]. In order to overcome this problem, I used a flavor of DFT called the hybrid functional DFT. This method allows us to mix a specified fraction of exact Hartree-Fock exchange energy with the approximate exchange-correlation energy, thereby improving the accuracy of the bandgap calculations. Hybrid functional DFT that uses the GGA approximation under the PBE scheme is typically denoted as PBE0, and the default mixing fraction is set as 25%.

For the ground state energy calculations in SiO<sub>2</sub> models, I used unscreened hybrid functionals at PBE0 level with 35% of exact Hartree-Fock exchange. This mixing fraction was determined to be appropriate to reproduce the experimental bandgap of SiO<sub>2</sub> (8.9 eV).

However, such hybrid functional DFT calculations are computationally very intensive. Thus, long molecular dynamics simulations and energy minimizations involving SiO<sub>2</sub> models were performed at a regular PBE level without hybrid functionals. In this work, structural relaxations in SiO<sub>2</sub> supercell were performed until the forces on the atoms were less than 0.07 eV/Å.

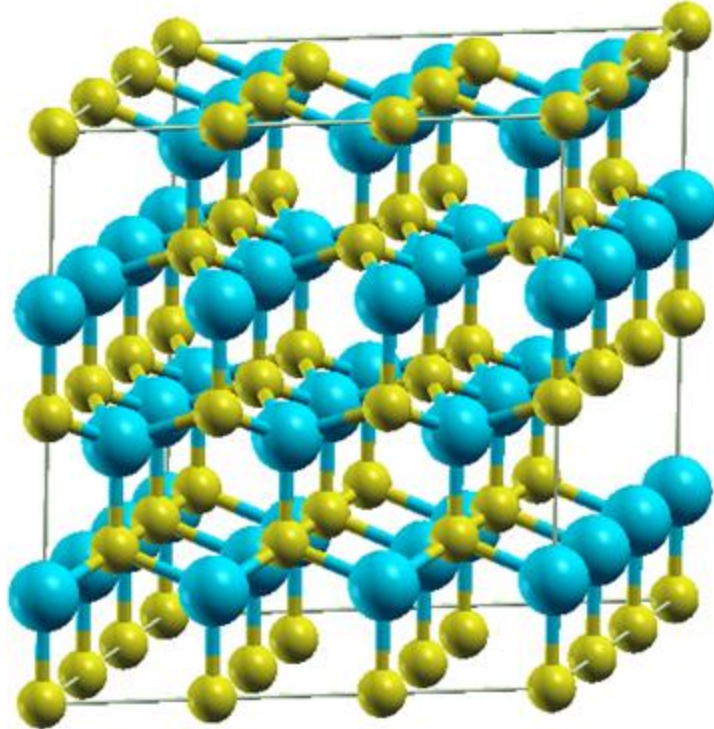


Figure 2.6: A 72-atom supercell of 4H-SiC used in this work. Blue and yellow spheres represent Silicon and carbon atoms, respectively.

For the ground state energy calculations in 4H-SiC, a 72-atom supercell, the structural properties of which were adopted from Ref. [69], was used in this work. This is shown in Figure 2.6. A plane-wave energy cutoff of 950 eV was used, with the Brillouin zone sampled at the Gamma point. As in a-SiO<sub>2</sub>, the core electron interactions were accommodated through norm-conserving pseudopotentials [66]. In order to approximate the exchange and correlation energy, I used the PBE0 scheme under the Generalized-Gradient Approximation (GGA) with a mixing fraction of 11%. This mixing reproduced the experimental bandgap of 4H-SiC (3.25 eV).

In the following chapters, I integrate hybrid functional DFT and other physics-based modeling techniques described in this chapter to understand the role of defects in the reliability and performance degradation of 4H-SiC power MOSFETs.

# Chapter 3: High Temperature-and-Gate Bias Stress-assisted Reliability Degradation in 4H-SiC Power MOSFETs

## 3.1 Background and Motivation

High Temperature and Gate Bias (HTGB) stress-induced threshold voltage ( $V_{th}$ ) instability is a serious reliability concern in 4H-Silicon Carbide (4H-SiC) power MOSFETs. Specifically, negative and positive shifts in  $V_{th}$  respectively lead to unpredictable increase in off-state drain-leakage current and on-state resistance, and adversely impact reliable device operation [4]. At room temperature,  $V_{th}$  instability is generally attributed to the bias-dependent charging and discharging of near-interfacial oxygen-vacancy hole traps in the gate oxide ( $\text{SiO}_2$ ) [4, 6, 7]. However, recent experiments show excessive aggravation of  $V_{th}$  instability when 4H-SiC power MOSFETs are bias-stressed under increasing temperatures,<sup>9</sup> suggesting possible Negative Bias-and-Temperature Stress (NBTS)-dependent activation of additional switching oxide hole traps [9, 14, 70].

In the past, oxygen vacancy-related switching oxide hole traps (called the  $E_y'$  centers) have been successfully invoked to model experimentally observed threshold voltage shifting in irradiated and/or bias-temperature-stressed Si MOSFETs [12, 13, 15, 71, 72, 73]. Similarly, this model, known as the Harry-Diamond Lab (HDL) model, was recently used to explain  $V_{th}$  instability in 4H-SiC MOSFETs bias-stressed at room temperature [4, 6]. At an atomic level, the HDL model envisaged electrons to directly tunnel into and out of  $E_y'$  centers in response to the polarity of the applied

bias stress. This model was subsequently validated using Electron Spin Resonance (ESR) spectroscopy [13, 28, 72, 74].

In 4H-SiC MOSFETs, the room temperature back-and-forth  $V_{th}$  instability (that is, the difference between the absolute threshold voltages measured after bias-stressing a MOSFET with opposite polarities) was experimentally observed to depend linearly on the logarithm of bias-stress duration [4]. This behavior was explained using a WKB approximation-based two-way direct tunneling model, which was consistent with the HDL model [10]. However, very recently, the back-and-forth threshold voltage instability was seen to increase super-linearly in many state-of-the-art 4H-SiC MOSFETs when they were bias-stressed under higher temperatures [9]. Given the weak dependence of direct tunneling on temperature, this behavior is reconciled with the two-way tunneling model by considering the NBTS-assisted activation of additional oxygen vacancy-related switching oxide hole traps. Furthermore, this view is supported by ESR and EDMR measurements in Silicon [14] and 4H-SiC MOSFETs [70], where significant increase in oxygen vacancy signatures was recorded under high temperature and negative bias stress. Additionally, recent electrical experiments indicated practically inappreciable aggravation in  $V_{th}$  instability when MOSFETs were temperature-stressed in the absence of applied bias [14, 75]. On the other hand, generation of electron trapping centers was also observed under very high operating temperatures [9], although the significant component of back-and-forth  $V_{th}$  instability is currently believed to be due to hole trap activation during negative bias stress [9, 14, 70, 75, 76, 77].

Theoretically, oxygen vacancies have been observed to assume diverse structural configurations in their neutral and hole trapped states in amorphous SiO<sub>2</sub> (a-SiO<sub>2</sub>), using Density Functional Theory (DFT)-based *ab-initio* simulations [17, 18, 21, 78, 79, 80, 81, 82, 83, 84]. This includes the Si-Si dimer (also called the  $E_{\delta}'$  center), and the positive and neutral puckered configurations ( $E_{\gamma}'$ ), which are consistent with the HDL model [18, 78, 79]. While the structural, energetic and electrical properties of these structures have received considerable attention in the past [17, 18, 21, 78, 79, 80, 81, 82], other configurations like the back-projected  $E_{\gamma}'$  center [21, 82, 83, 84] and their role in  $V_{th}$  instability (or equivalently, the HDL model) are less understood. Additionally, previous *ab initio* studies have focused largely on generating and studying these configurations in isolation [39, 85]. Their inter-conversions due to HTGB stressing of 4H-SiC MOSFETs and the resultant changes in their electrical activities, to our knowledge, have received limited attention in the past [18, 73, 78, 79].

In this chapter, I use DFT calculations to propose an oxygen-vacancy hole trap activation model to explain HTGB stress-assisted back-and-forth  $V_{th}$  instability in 4H-SiC MOSFETs. Subsequently, I perform transient simulation of the activation process by integrating the insights derived from DFT with Arrhenius rate equations. The model is then validated by comparison with  $\Delta V_{th}$  measurements. I also use the model to explain the recent Electrically Detected Magnetic Resonance (EDMR) spectroscopy observations [14, 70].

## 3.2 Analysis Techniques

In this section, I provide an overview of the approach used in analyzing material defects using DFT. The electrical activity and the stability of defects in various charge states is generally analyzed through its Charge Transition Levels (CTL). However, instantaneous processes like tunneling are understood through its Optical Transition Levels. The fundamental difference between CTL and OTL is that CTL calculations consider the structural relaxation effects occurring in the defect following its charging/discharging, while OTL does not. This is because processes like tunneling and photo-absorption are faster than the structural relaxation processes in defects. As a result, the same atomic defect in a material could present different defect levels before and after charging/discharging due to structural relaxations. The CTL and OTL are further elucidated below.

### 3.2.1 Charge Transition Levels

The first step towards understanding the electrical activity and stability of defects in a material involves the estimation of their formation energies in various charge states using plane-wave density functional simulations [18, 78, 86, 87]. The following defect formation reaction is considered.



In the above chemical reaction, the reaction product includes the material with defect that is charged. The reactants separately include the Bulk material,  $n$  defect atoms from a reservoir at chemical potential  $\mu$ , and  $q$  number of electronic charges

from a reservoir at its chemical potential  $E_F$  (which is also the Fermi level in a MOSFET).

In general, the formation energy (or the enthalpy change) for the defect formation reaction could be expressed in terms of the Fermi level  $E_F$  using DFT as [88]

$$E_{f,q}(E_F) = E_{tot,q} - E_{tot}^{bulk} - \sum_i n_i \mu_i + q(E_{vo} + \delta V + E_F) + E_{corr,q} \quad (3.2)$$

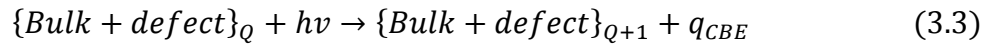
Here,  $E_{tot,q}$  and  $E_{tot}^{bulk}$  denote the total ground state energies of geometry optimized, defect-containing a-SiO<sub>2</sub> (charged  $q$ ) and bulk a-SiO<sub>2</sub> respectively, as calculated by DFT.  $n_i$  represents the number of respective impurity atoms added at its chemical potential  $\mu_i$ .  $E_{vo}$  refers to the SiO<sub>2</sub> valence band edge (which serves as the reference to the Fermi level).  $\delta V$  and  $E_{corr,q}$  indicate DFT-related correction terms. The correction term  $\delta V$  is used for aligning the electrostatic potential existing far away from the neutral vacancy with that of defect-free a-SiO<sub>2</sub> bulk. This was found to be small in silica. The second correction term, denoted as  $E_{corr,q}$ , accounts for the artificial energy arising from the electrostatic interactions between images of charged defects in periodic supercells. Multiple methods for correcting such finite-size supercell errors have been proposed previously, with no general consensus [37, 88, 89, 90]. Therefore, I generally perform my calculations without including them unless stated otherwise, and later introduce them as error bars [18]. However, I will explicitly mention the type of correction used wherever required.

The electrical activity of defects in a-SiO<sub>2</sub> in response to applied bias was deduced using their thermodynamic charge transition levels (CTL) [86, 87]. This equilibrium quantity is defined as the Fermi level (with respect to the SiO<sub>2</sub> valence

band edge) required to match the formation energies of a defect in its two different charge states,  $q$  and  $q'$ . Thus, in this dissertation, CTL is represented as the graphical solution of equation (3.2) for these charge states. In equilibrium, the defect is regarded as stable in charge state  $q$  (or  $q'$ ) for Fermi levels below (or above) the  $q/q'$  CTL. In the case of the 4H-SiC/SiO<sub>2</sub> MOS system, we argue that the near-interfacial oxide defects, with CTLs existing within the bandgap of 4H-SiC, could be charged/discharged depending on the Fermi level in the 4H-SiC substrate.

### 3.2.2 Optical Transition Levels

In order to understand the role of defects in instantaneous processes like tunneling and photo-absorption, I resort to the calculation of Optical (or Vertical) Transition Levels (OTL). For the purpose of elucidating OTLs, consider the following photo-absorption reaction in a defect.



Here, the reactants separately include the defect in the bulk in charge state  $Q$ , and a photon of energy  $hv$ . The photon knocks out an electron  $q$  from the defect, and typically places it at the conduction band edge ( $CBE$ ) (shown as a reaction product). Additionally, the positively charged defect in charge state  $Q+1$  On the product side remains structurally unrelaxed as the relaxation time is greater than the photo-absorption process itself. (Please note that such structural relaxations in defects are called Frank-Condon relaxations.)

For the reaction in equation (3.3), the location of the ( $Q/Q+1$ ) OTL with respect to the CBE is given as,

$$\varepsilon(Q/Q + 1) = E_{Q+1}^{unrelaxed} - E_Q^{relax} + E_{CBE} \quad (3.4)$$

In addition, the finite-size supercell correction, described in Section 3.2.1, should be applied to the above equation.

In the context of transient modeling of 4H-SiC MOSFET reliability, OTLs are the natural choice for understanding the energy levels of defects involved in tunneling. For example, hole trapping by an oxide defect from the 4H-SiC Valence Band Edge (VBE) will be visualized as a photo-absorption process, where the oxide defect located at its (0/+1) OTL emits an electron into the VBE of 4H-SiC.

### 3.3 Bandgap Alignment

In the context of the 4H-SiC/SiO<sub>2</sub> MOS system, the near-interfacial oxide defects, whose CTLs exist within the bandgap of 4H-SiC, could be charged/discharged depending on the Fermi level in the 4H-SiC substrate. This entails accurate lining up of 4H-SiC bandgap with respect to that of SiO<sub>2</sub>, which we achieved using the methodology proposed by Van de Walle *et. al.* [91]. This method is described below.

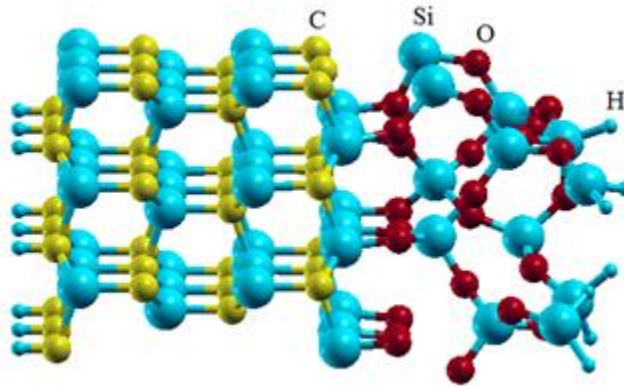


Figure 3.1: A Model of 4H-SiC/SiO<sub>2</sub> interface.

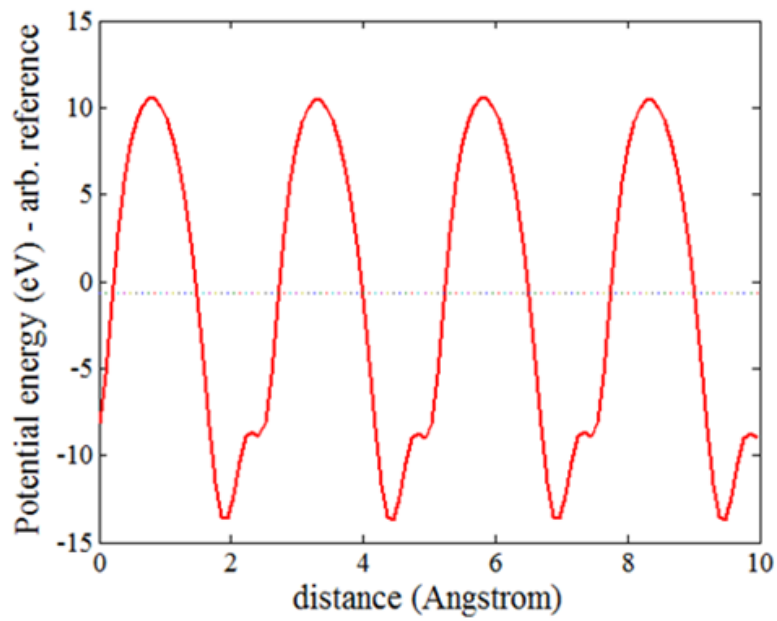


Figure 3.2: Plane-average electrostatic potential in 4H-SiC bulk as calculated using DFT.

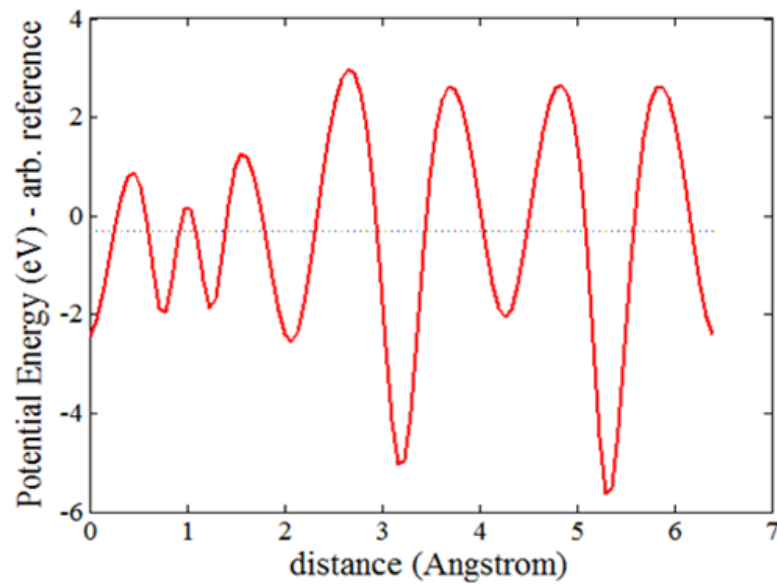


Figure 3.3: Plane-average electrostatic potential in a-SiO<sub>2</sub> bulk as calculated using DFT.

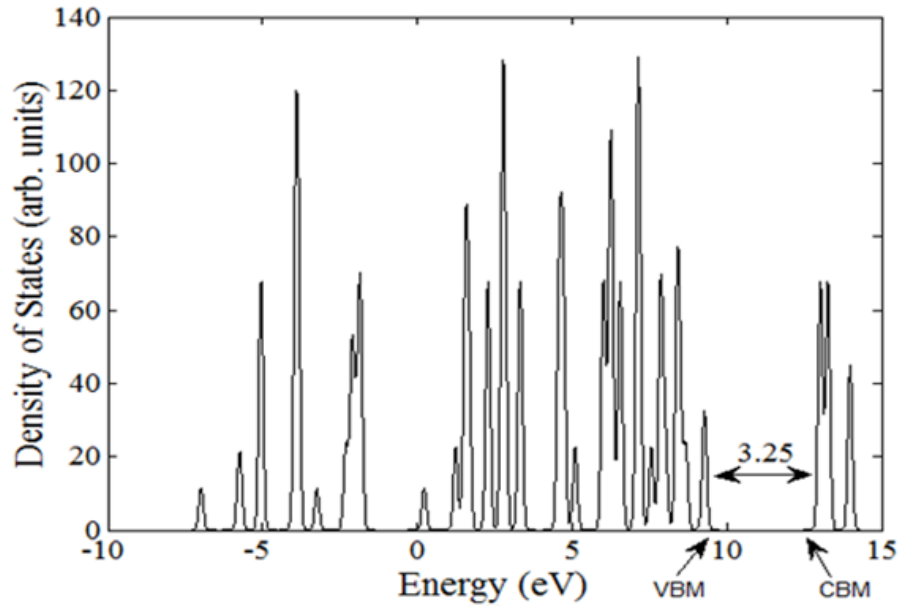


Figure 3.4: Density of states for 4H-SiC bulk as calculated using DFT. The bandgap is indicated.

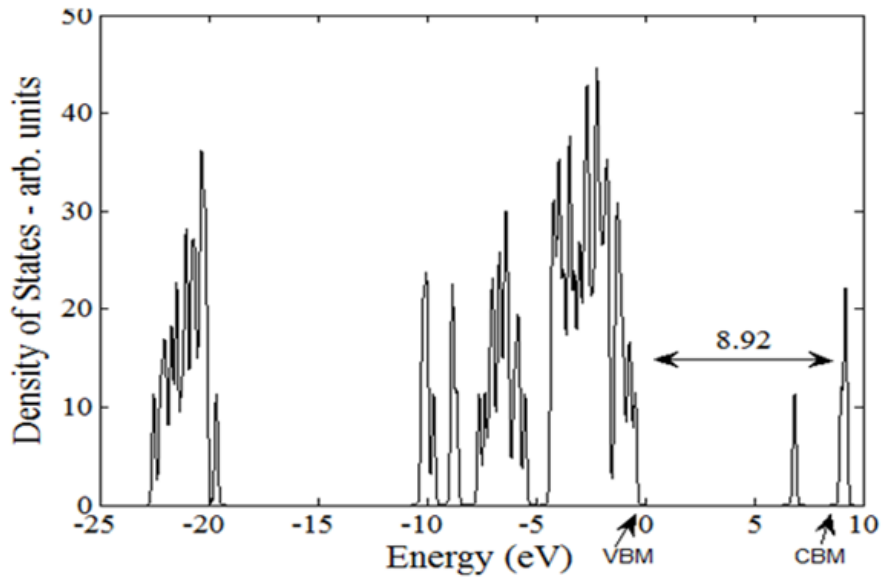


Figure 3.5: Density of states for a-SiO<sub>2</sub> bulk as calculated using DFT. The bandgap is indicated. The additional state within the bandgap is likely to be due to additional strain.

Firstly, a realistic amorphous silica model was generated using first-principles melt-and-quench molecular dynamics. This was done on a 36-atom supercell, using the procedure described in Section 2.5.2.

The SiO<sub>2</sub> model generated above was then placed carefully over a 72 atom 4H-SiC unit cell, whose crystal properties were obtained from literature [69]. Density functional geometry optimization was performed on the combined system until the force acting on each atom was less than 0.05eV/Å. At the end of the simulation, I obtained an ideal 4H-SiC/SiO<sub>2</sub> interface devoid of any dangling bond as shown in Figure 3.1. The surface dangling bonds were terminated using Hydrogen atoms.

Subsequently, I performed separate hybrid-functional DFT calculations on bulk 4H-SiC (72 atoms supercell) and bulk amorphous SiO<sub>2</sub> (36 atoms) to determine three landmark potentials for each of them – a) the mean Electrostatic Potential (EP) in the bulk, b) the Valence Band Maximum (VBM), and c) the Conduction Band Minimum (CBM). The mean EP in the bulk was calculated from the plane-averaged electrostatic potential in the bulk (in the z-direction). The plane-averaged electrostatic potential for 4H-SiC and silica are given in Figures 3.2 and 3.3, respectively. The VBM and CBM, with EP as the reference, are identified from the calculated density of states (DOS). The calculated DOS for 4H-SiC and silica are shown in Figures 3.4 and 3.5, respectively. Next, I calculated the plane-averaged potential variation in the interface. This is given in Figure 3.6. The shift observed in the mean EP between 4H-SiC and SiO<sub>2</sub> in the interface structure is applied to the mean EPs obtained from individual supercell calculations to determine the bandgap lineup (Figure 3.7). The resulting bandgap alignment [92] that agrees well with previous experimental [93]

and theoretical predictions [37] help to validate my computational setup described in Section 2.6.

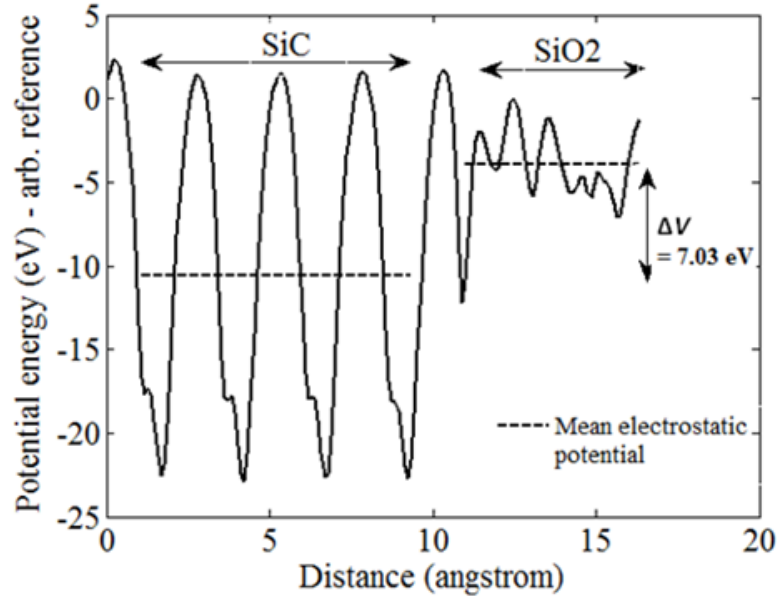


Figure 3.6: Plane-average electrostatic potential across the 4H-SiC/SiO<sub>2</sub> interface as calculated using DFT.

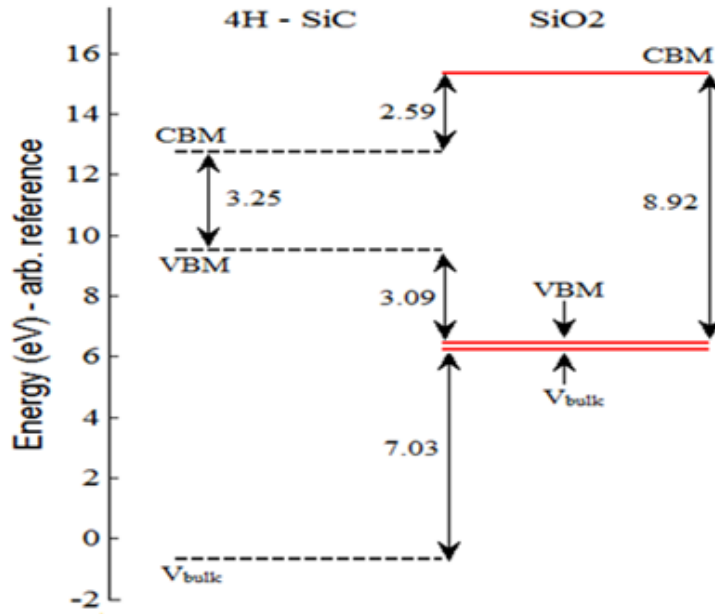


Figure 3.7: Bandgap alignment between 4H-SiC and SiO<sub>2</sub> at their interface.

### 3.4 Oxygen Vacancy Hole Traps

In this section, I investigate the electrical and structural properties of near-interfacial oxygen vacancies in 4H-SiC MOSFETs using DFT. The computational setup used in these calculations is described in Section 2.6. As regards DFT correction factors, the Lany-Zunger [90] and Makov-Payne [89] schemes will lower the CTL values reported in this section by  $\sim 0.3$  eV and  $\sim 0.6$  eV, respectively.

I introduced and studied oxygen vacancy in five models of amorphous SiO<sub>2</sub>. Four of them were generated using the SBB methodology, described in Section 2.5.1 (Type 1 supercells). The remaining one was generated using the melt-and-quench quantum molecular dynamics, described in Section 2.5.2 (Type 2 supercells). The relative total formation energies of neutral vacancies were found to vary over approximately a 5 eV range. This approach allowed me to gauge the effects of local environment on the electrical and structural behavior of oxygen vacancies.

By virtue of their local atomic environment, oxygen vacancies were seen to exhibit two distinct behaviors in terms of the location of their charge transition levels. The first category – which I term as ‘permanently electrically active’- was readily seen to create a CTL within the 4H-SiC bandgap. The other category, designated in this dissertation as ‘electrically inactive’, did not have a CTL within the 4H-SiC bandgap. It is worth mentioning that this nomenclature is strictly within the context of BTS as applied to the 4H-SiC/SiO<sub>2</sub> interface, and might not hold for a different bandgap alignment (interface system) or processes like irradiation. The ‘permanently electrically active’ and ‘electrically inactive’ oxygen vacancies and their diverse

BTS-induced structural and electronic transformations in 4H-SiC MOSFETs are further explained below.

### 3.4.1 ‘Permanently Electrically Active’ Oxygen Vacancy

The ‘permanently electrically active’ oxygen vacancies were generally observed in Type 1 supercells that represent regions of relatively high amorphousness in comparison with  $\alpha$ -quartz. The overall sequence of its structural and electrical transformations in a representative sample is depicted in Figure 3.8. The individual defect structures, their electrical properties, and dynamics are explained below.

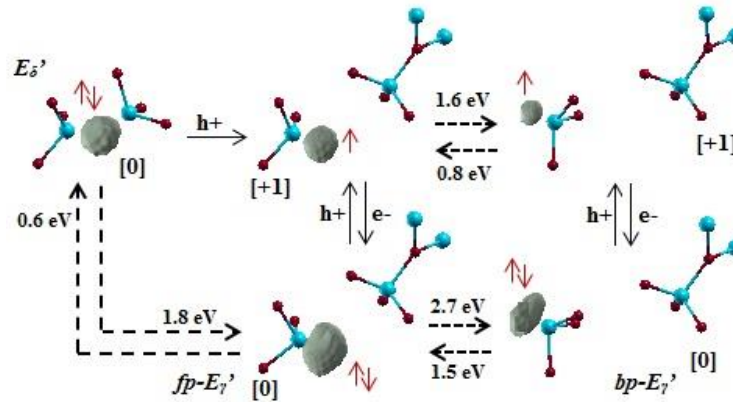


Figure 3.8: Sequence of structural transformations of ‘permanently electrically active’ near-interfacial oxygen vacancies seen in highly amorphous oxide regions in 4H-SiC MOSFETs. Bias-dependent tunneling and thermal processes (barriers) are depicted as solid and dashed lines, respectively. Large blue spheres and small red spheres represent Si and O atoms, respectively. The shaded regions represent the calculated Electron Localization Function (ELF) isosurfaces at ELF=0.89, with the adjacent red arrow/s showing the type of localization (unpaired/paired). fp- and bp- stand for forward-projected and back-projected, respectively. The sequence involving dimer and forward-projected configurations resemble the HDL model.

The Si-Si dimer:

In their neutral states under equilibrium, ‘permanently electrically active’ oxygen vacancies manifested themselves as Si-Si dimers (neutral  $E_\delta$ ), with an inter-silicon distance of 2.5 Å. The electron pair was seen to be spatially localized between the Si atoms, as indicated by the calculated Electron Localization Function (ELF) in Figure 3.8. ELF is directly related to the probability of finding an electron in the vicinity of another electron with the same spin. [94]. It is defined in such a manner that its values closer to one or zero denote regions of high (lone/paired electrons) or low electron localization, respectively. In this work, the distinction between ELF’s representing lone or paired electrons is interpreted from the context of the DFT simulation (positive of neutral defect).

Formation of the forward-projected, backbonded configuration:

Electrically, the Si-Si dimer in Figure 3.8 was seen to readily trap a hole in response to an applied negative bias because of the +1/0 charge transition level (Section 3.2.1) within the 4H-SiC bandgap (at  $\sim E_v + 1.4$  eV) as shown in Figure 3.9. Upon hole capture, the dimer configuration was seen to spontaneously transform into a forward-projected, backbonded configuration (positive  $E_\gamma$  center) as shown in Figure 3.8. Here, the trapped hole is seen to reside on the Si atom which backbonds with a suitably placed oxygen atom behind it. However, the lone electron continues to remain on the other Si atom, as indicated by the calculated ELF shown in Figure 3.8. The Si-Si distance for this configuration was measured to be 4.21 Å. These lattice relaxations are in agreement with previous reports [79], and such mechanisms have been identified to stabilize the defect in its positively charged state [22]. Also, the

geometric rules that allow puckering and backbonding of Si atoms have been identified previously [16].

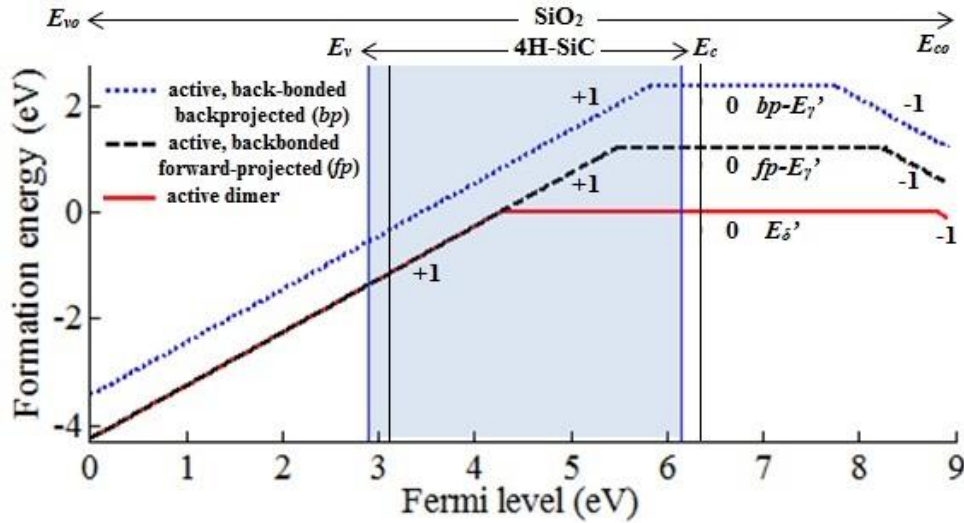


Figure 3.9: Most stable charge states as a function of Fermi level for various ‘permanently electrically active’ oxygen vacancy configurations seen in highly amorphous oxide regions in 4H-SiC MOSFETs. The shaded region represents the experimental bandgap line up between 4H-SiC and SiO<sub>2</sub>. Solid vertical lines represent theoretical bandgap lineup. The kinks represent charge transition level for the respective configuration, which is seen to move towards right as the vacancy accesses higher energy structures. All the configurations are permanent switching oxide traps due to their +1/0 CTL within the 4H-SiC bandgap.

However, upon detrapping of the hole, the positive  $E_{\gamma}'$  center structurally transforms into a new higher energy configuration - the neutral forward-projected, backbonded  $E_{\gamma}'$  center as in Figure 3.8 - instead of the original neutral dimer state ( $E_{\delta}'$ ). The inter-silicon distance is 3.99 Å. The ELF indicates that the captured

electron pairs with the lone electron on Si, forming a dipole with the positively charged backbonded Si atom. The +1/0 CTL for switching between positive and neutral  $E_{\gamma}'$  ( $E_v + 2.6$  eV), is seen to be closer to the 4H-SiC conduction band in comparison with the previous neutral  $E_{\delta}'$  to positive  $E_{\gamma}'$  CTL. During subsequent hole trapping/de-trapping cycles, the center was seen to switch between positive and neutral  $E_{\gamma}'$  structures at the new shifted CTL ( $E_v + 2.6$  eV), without relapsing into original  $E_{\delta}'$  configuration which would be a thermally-assisted process. This observation is consistent with previous *ab-initio* studies [18, 79].

We now analyse the temperature-assisted transition between neutral  $E_{\gamma}'$  and neutral original dimer  $E_{\delta}'$  structure (indicated with the dotted arrows in Figure 3.8). We calculated the minimum energy pathway (MEP) for this transformation using DFT-based climbing-image Nudged Elastic Band (NEB) method, which is described in Section 2.4 [57]. Due to the exorbitant computational costs involved in hybrid-functional DFT, the following approach was adopted. The reaction coordinates, which includes the saddle point, were first estimated using DFT under the regular PBE scheme. Following this, the ground state energies of the initial, final and saddle point configurations were recalculated using hybrid functionals. The NEB-based reaction pathway for neutral dimer  $E_{\delta}'$  to neutral  $E_{\gamma}'$  is given in Figure 3.10 (a). The forward and reverse activation energies (1.8 eV and 0.6 eV, respectively) for the transitions are also indicated in Figure 3.8 for better clarity.

The electrical and corresponding structural transformations outlined above agree with the ‘switching oxide trap’ model of oxygen-vacancy hole traps (or the Harry-Diamond Lab (HDL) model) proposed previously for silicon MOSFETs [12,

73] and extended recently to include 4H-SiC MOSFETs [4, 6]. This model has also found support in ESR and EDMR studies [13, 70, 71, 72]. Also, our observations are consistent with previous density functional studies on oxygen-vacancy hole traps [18, 79], which also supported the HDL model.

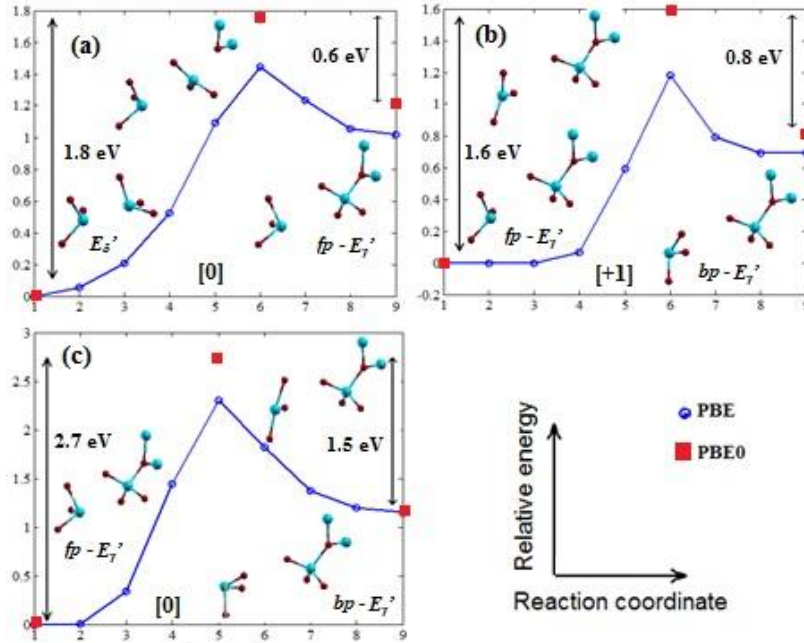


Figure 3.10: Minimum energy pathways, calculated using standard DFT-based nudged elastic band (NEB) method, for thermally-assisted transition between various ‘permanently electrically active’ oxygen vacancy configurations in 4H-SiC MOSFETs. (a) neutral dimer  $E_{\delta}'$  to neutral forward-projected (fp)  $E_{\gamma}'$ , (b) positive forward-projected  $E_{\gamma}'$  to positive back-projected (bp)  $E_{\gamma}'$ , and (c) neutral forward-projected  $E_{\gamma}'$  to neutral back-projected  $E_{\gamma}'$ . The atomic arrangements of initial, final and saddle point structures are indicated. Hybrid functional DFT was used to recalculate the energies at these special reaction coordinates (indicated as red squares) to determine the activation barriers.

Formation of the back-projected, backbonded configuration:

An additional high energy structural configuration of the oxygen-vacancy defect in SiO<sub>2</sub> - the back-projected  $E_{\gamma}'$  structure - was investigated previously by Mukhopadhyay *et. al.* [83, 84]. Here, I extend the HDL model to include this configuration as well.

Under negative bias, the conversion from positive, forward-projected  $E_{\gamma}'$  to positive, back-projected  $E_{\gamma}'$  structures is assisted by temperature. The MEP, including the saddle point configuration, for this process is depicted in Figure 3.10(b). The ELF for the positive, back-projected  $E_{\gamma}'$  structure (Figure 3.8) indicates the spatial localization of a lone electron pointing away from the vacancy. The positively charged Si atom continues to remain back-bonded, with an inter-silicon separation of 5.08 Å.

The neutralization of the charge state of the back-projected  $E_{\gamma}'$  structure under applied positive bias is seen to occur when the Fermi level sweeps the +1/0 CTL of  $E_{\nu}$  + 2.9 eV (Figure 3.9). This CTL is shifted further towards the 4H-SiC conduction band in comparison with the forward-projected  $E_{\gamma}'$  +1/0 CTL. Additionally, ELF calculation indicates that the added electron pairs with the lone electron, leaving the positively charged Si atom backbonded. Thus, the structural transformations upon neutralization is minimal with a new Si-Si distance of 5.27 Å. Under AC bias stressing, the back-projected  $E_{\gamma}'$  center cycles between the positive and neutral configurations at its new CTL, and does not relapse to the forward-projected  $E_{\gamma}'$  or the dimer  $E_{\delta}'$  structures.

We also calculated the activation barrier for the temperature-assisted transformation between neutral forward-projected and back-projected  $E_{\gamma}'$  centers, as depicted in Figure 3.10(c) and Figure 3.8. Comparison of the activation barriers under positive and neutral conditions indicates that the back-projected configuration is more easily reached from the forward-projected  $E_{\gamma}'$  structure under negative bias (hole-trapped) and temperature.

In conclusion, various configurations of oxygen vacancy centers discussed in the above sections can be termed as electrically active hole traps as they introduce +1/0 CTLs within the bandgap of 4H-SiC. A large number of such diverse defect configurations is likely to be separately created during the high temperature fabrication and passivation processes encountered in 4H-SiC technology, as indicated by the statistics presented previously [79]. On the other hand, as the above results indicate, these diverse configurations could also be derived from a common and basic ‘permanently electrically active’ Si-Si dimer defect through a combination of negative bias and temperature stresses. This interesting result is attributable to the significantly lower energy differences (and activation barriers) between positively charged structures in contrast to corresponding neutral configurations, as evidenced by Figure 3.9. This also explains the regular shift in the respective +1/0 CTLs towards the 4H-SiC conduction band, as the defect accesses higher energy structures through structural transformations.

### 3.4.2 ‘Electrically Inactive’ Oxygen Vacancies

The ‘electrically inactive’ oxygen vacancies were found to occur in Type 2 supercells that represent oxide regions with relatively low disorder. The overall

reaction pathways involved in its structural and electrical transformations in a representative sample is given in Figure 3.11. The details of the individual defect structures are separately elaborated below.

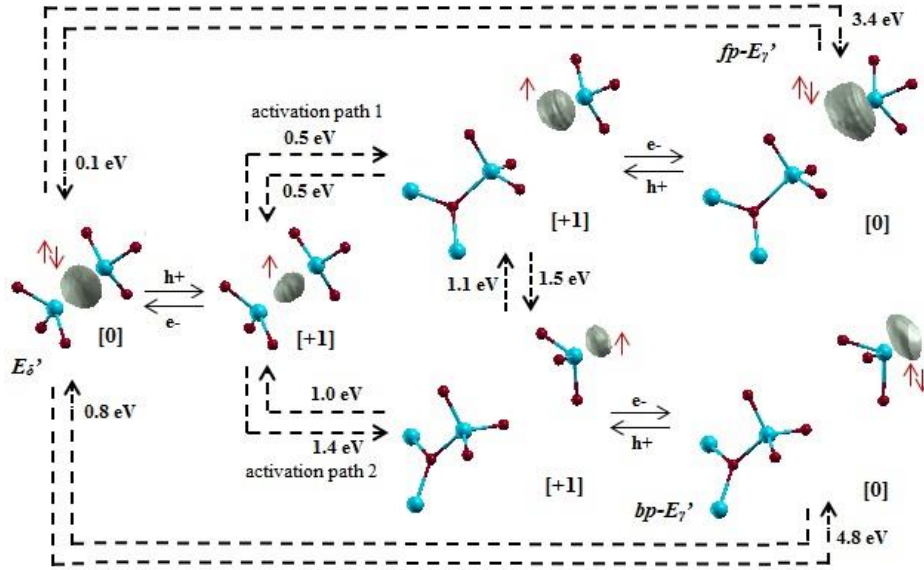


Figure 3.11: Sequence of structural transformations involved in the negative bias-and-temperature-assisted activation of ‘electrically inactive’ near-interfacial oxygen vacancies seen in less amorphous oxide regions to form ‘electrically active’ hole traps in 4H-SiC MOSFETs. The  $E_{\delta}'$  dimers are ‘electrically inactive’, as opposed to the ‘electrically active’ forward-projected (fp) and back-projected (bp)  $E_{\gamma}'$  structures. Bias-dependent tunneling and thermal processes (barriers) are depicted as solid and dashed lines, respectively. However, the final barrier for trap activation also depends on the 4H-SiC/SiO<sub>2</sub> bandgap alignment (see text). Large blue spheres and small red spheres represent Si and O atoms, respectively. The shaded regions represent the calculated Electron Localization Function (ELF) isosurfaces at ELF=0.89, with the adjacent red arrow/s showing the type of localization (unpaired/paired).

### The Si-Si dimer:

Under equilibrium, neutral ‘electrically inactive’ oxygen vacancies were observed to exist as Si-Si dimers (neutral  $E_\delta'$ ), with silicon atoms separated by 2.44 Å. This is shown in Figure 3.11. The calculated ELF indicates the sharing of electrons between the Si atoms. Upon capture of a hole, no major structural reorganization of the defect was observed with the inter-silicon distance increasing by ~16% (positive  $E_\delta'$ ), unlike the ‘permanently active’ defect where the positive Si atom backbonded with the rear oxygen with ~68% increase in Si-Si distance. Also, the lone electron appears to be localized between the two Si atoms as shown by its ELF in Figure 3.11 [16]. However, the +1/0 CTL for the neutral  $E_\delta'$  to positive  $E_\delta'$  switching described above is located 0.8 eV *below* the 4H-SiC valence band edge (Figure 3.12). This indicates that the equilibrium concentration of the positively charged  $E_\delta'$  state is comparatively small for all substrate Fermi levels within its bandgap (equivalently, for all applied gate bias stress, unlike irradiation). Thermodynamically, the equilibrium concentration of the positively charged  $E_\delta'$  center as a function of Fermi level ( $E_F$ ), with  $\Delta H$  (~ 0.8 eV) given from Figure 3.12, is

$$[E_\delta']_{+1} = [E_\delta']_0 \exp\left(\frac{-(\Delta H + E_F - E_v)}{k_b T}\right) \quad (3.5)$$

In other words, due to their relatively low equilibrium density, these defects are unlikely to significantly shift the threshold voltage negatively at room temperature.

However, despite their relatively small concentrations, the positive  $E_\delta'$  centers could transform into two possible positively charged configurations – the forward-projected (path 1) or the back-projected  $E_\gamma'$  (path 2), as depicted in Figure 3.11 - in presence of high temperature. I now consider each of them separately.

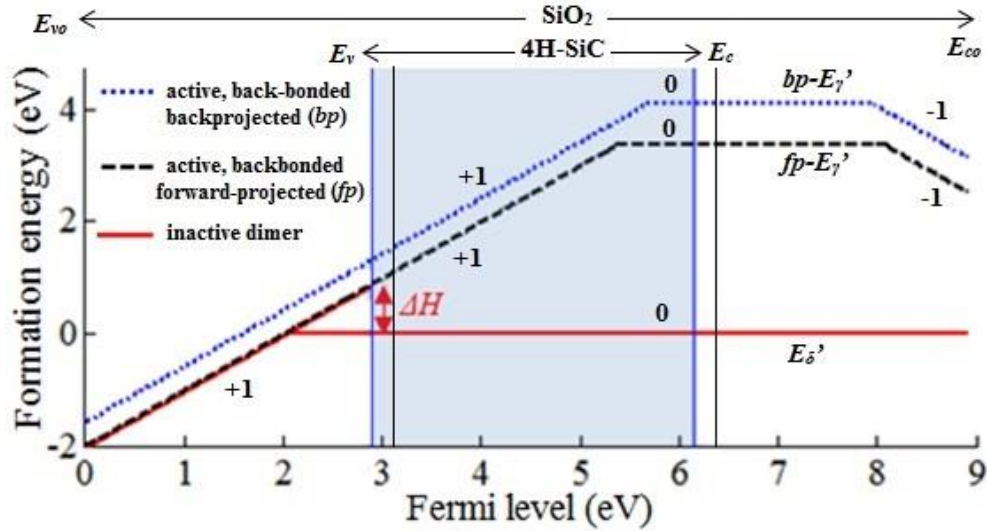


Figure 3.12: Most stable charge states as a function of Fermi level for ‘electrically inactive’ Si-Si dimer seen in less amorphous oxide regions in 4H-SiC MOSFETs, and its subsequent NBTS-activated configurations. The shaded region represents the experimental bandgap line up between 4H-SiC and SiO<sub>2</sub>. Solid vertical lines represent theoretical bandgap lineup. The kinks represent charge transition level (CTL) for the respective configuration, which is seen to move towards right as the vacancy accesses higher energy structures leading to hole trap activation. The initial Si-Si inactive dimer with +1/0 CTL below 4H-SiC bandgap is activated to form switching oxide hole traps with +1/0 CTL within the bandgap during NBTS.

Formation of the forward-projected, backbonded configuration:

Firstly, the conversion of the positive  $E_{\delta}'$  center to the positive forward-projected  $E_{\gamma}'$  center (path 1) requires a NEB-calculated activation barrier of  $E_b$  ( $= 0.5$  eV), as shown in Figure 3.13(a) and Figure 3.11. The energetics and kinetics of this reaction are in reasonable agreement with previous DFT study which calculated a barrier of 0.38 eV [18]. If we neglect the time dependence of the concentration of positive  $E_{\delta}'$

centers and the much slower path 2, then the Arrhenius rate of formation of positive forward-projected  $E_\gamma'$  is given as

$$\begin{aligned} \frac{d[E_\gamma']_{+1}}{dt} &= k_p [E_\delta']_{+1} \exp\left(\frac{-E_b}{k_b T}\right) \\ &= k_p [E_\delta']_0 \exp\left(\frac{-(\Delta H + E_F - E_v + E_b)}{k_b T}\right) \end{aligned} \quad (3.6)$$

Here,  $k_p$  is the constant of proportionality and  $k_b$  represents the Boltzmann constant. In other words, the Fermi level dependence of the above equation suggests that the rate of *activation* of additional hole traps is directly proportional to the concentration of free holes at the interface (as in the case of NBTI in Si pMOSFETs [95]). Equivalently, in the context of  $V_{th}$  instability in 4H-SiC MOSFETs where the Fermi level is restricted to vary within the bandgap, the overall activation barrier for the formation of *positive* forward-projected  $E_\gamma'$  from the ‘electrically inactive’ *neutral*  $E_\delta'$  becomes a function of the 4H-SiC Fermi level ( $E_F - E_v$  in Figure 3.12), and is given as

$$E_{b\_net} = \Delta H + E_F - E_v + E_b \quad (3.7)$$

Structurally, this defect has the lone electron localized on the forward-projected Si atom (see ELF in Figure 3.11) while the positively charged Si is backbonded to the rear oxygen. The Si-Si distance is 4.3 Å.

Interestingly, the +1 forward-projected  $E_\gamma'$  configuration exhibits a +1/0 CTL against neutralization, which lies *within* the 4H-SiC bandgap (at  $E_v + 2.5$  eV). Upon neutralization, the captured electron pairs with the lone electron on silicon, forming a dipole structure (see ELF in Figure 3.11) similar to the forward-projected  $E_\gamma'$  center discussed in the context of ‘permanently active’ vacancies. The Si-Si separation in the

neutral configuration is  $3.95 \text{ \AA}$ . The defect is now allowed to switch between positive and neutral states under AC bias making it ‘electrically active’ as opposed to the original ‘electrically inactive’ dimer ( $E_\delta$ ). Evidently, the overall thermal barrier for this activation, given as  $\Delta H + E_F - E_v + 0.5 \text{ eV}$  by equation (3.7), decreases as the Fermi level approaches the 4H-SiC valence band under negative biasing. Additionally, the activation rate is also enhanced by increasing temperature ( $k_bT$ ). These observations suggest that significant trap activation could be achieved through a combination of temperature *and* negative bias. However, the neutral  $E_\gamma$  configuration is expected to be short-lived due to the low thermal barrier ( $\sim 0.1 \text{ eV}$ ) for its transformation to the original inactive Si-Si dimer state (deactivation), as shown in Figure 3.13(b) and Figure 3.11.

*Formation of the back-projected, backbonded configuration:*

Next, we consider the second pathway for trap activation (path 2) where the positive  $E_\delta$  center turns into the positive back-projected  $E_\gamma$  configuration (Figure 3.11), overcoming a thermal barrier of  $E_b = 1.4 \text{ eV}$  (Figure 3.13(c) and Figure 3.11). However, due to the bounds imposed on the 4H-SiC Fermi level in the context of a MOSFET, the relevant reaction in this case is the formation of the positive back-projected  $E_\gamma$  from the stable ‘electrically inactive’ neutral  $E_\delta$ . By applying equation (3.7), the Fermi level-dependent activation barrier for this reaction is approximately calculated as  $\Delta H + E_F - E_v + 1.4 \text{ eV}$ , where  $\Delta H \sim 0.8 \text{ eV}$  from Figure 3.12. Structurally, in the +1 back-projected  $E_\gamma$  defect, the lone electron on Si is spatially oriented away from the vacancy as shown by its ELF (Figure 3.11). The Si-Si separation is  $5.24 \text{ \AA}$ .

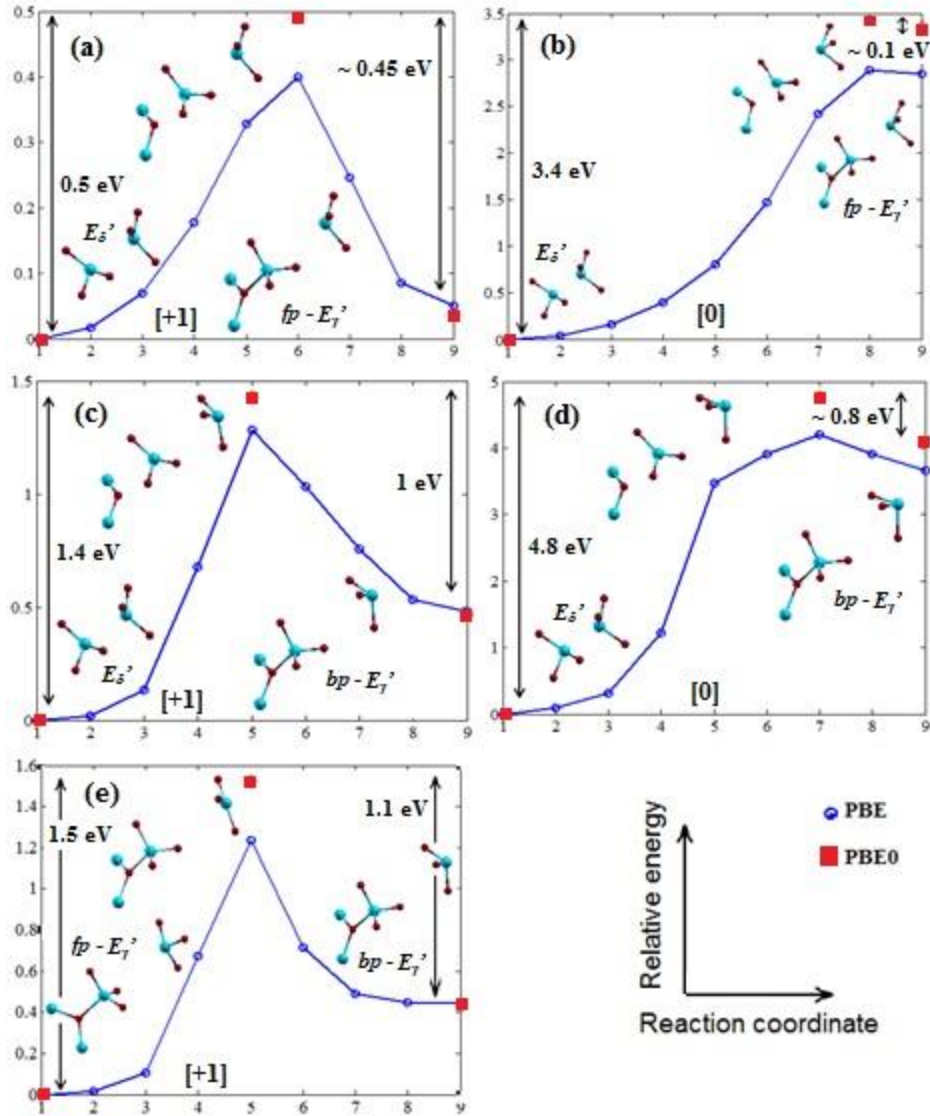


Figure 3.13: Minimum energy pathways, calculated using standard DFT-based nudged elastic band (NEB) method, for thermally-assisted inter-conversions between various oxygen vacancy configurations seen in less amorphous oxide regions in 4H-SiC MOSFETs. (a) positive dimer  $E_{\delta}'$  to positive forward-projected (fp)  $E_{\gamma}'$ , (b) neutral dimer  $E_{\delta}'$  to neutral forward-projected  $E_{\gamma}'$  (c) positive dimer  $E_{\delta}'$  to positive back-projected (bp)  $E_{\gamma}'$ , (d) neutral dimer  $E_{\delta}'$  to neutral back-projected  $E_{\gamma}'$ , and (e) positive forward-projected  $E_{\gamma}'$  to positive back-projected  $E_{\gamma}'$ . The atomic

arrangements of initial, final and saddle point structures are indicated. Hybrid functional DFT was used to recalculate the energies at these special reaction coordinates (indicated as red squares) to determine the activation barriers. However, the final barrier for trap activation also depends on the 4H-SiC/SiO<sub>2</sub> bandgap alignment (see text).

The +1 back-projected  $E_{\gamma}'$  structure is also seen to readily trap an electron for 4H-SiC Fermi levels above  $E_v + 2.8$  eV, as depicted in Figure 3.12, making it electrically ‘active’. In the neutral state, the defect is seen (in Figure 3.11) to pair the added electron along with the lone electron of the back-projected Si atom with no major structural rearrangements. The Si atoms, in this case, are separated by 5.45 Å. Also, the defect readily transforms back-and-forth between positive and neutral back-projected  $E_{\gamma}'$  configurations upon hole trapping and de-trapping, in response to applied AC (Figure 3.11) bias. As in the case of path 1, the trap activation rate *via* path 2 is enhanced with the application of negative bias *and* temperature. However, in contrast to the neutral forward-projected  $E_{\gamma}'$  configuration, neutral back-projected  $E_{\gamma}'$  configuration requires a much higher thermal barrier of  $\sim 0.8$  eV for its conversion (deactivation) to the original ‘inactive’ dimer structure, as indicated in Figure 3.13(d) and Figure 3.11. Thus, this state is more durable unlike its forward-projected form, as reported previously [96].

We also calculated the thermal barriers for the inter-conversion between positive forward-projected and positive back-projected  $E_{\gamma}'$  configurations. The results, given

in Figure 3.13(e) and Figure 3.11, are in reasonable agreement with previously reported activation barriers [84, 96].

### 3.4.3 Additional Structural Transformations in Hole-trapped Oxygen Vacancies - Secondary Back-bonding:

In this section, I consider additional structural transformations in the positively charged, back-bonded oxygen vacancy hole trap configurations. This includes the migration of the triply coordinated oxygen atom, as shown in Figure 3.14 (a). Here, one of the original Si-O bonds of the triply coordinated oxygen atom breaks under NBTS. Following this, the detached Si atom puckers and back-bonds with an oxygen atom behind it through a process which is henceforth referred to as ‘secondary back-bonding’. Such structural transformations were observed in both ‘permanently electrically active’, and ‘activated’ back-bonded hole traps. The resulting secondary back-bonded structure could add extra stability to the hole-trapped defect depending on the local atomic arrangements. This is analyzed below.

The geometric atomic arrangement that facilitates secondary back-bonding was studied in terms of the parameters  $\alpha$ ,  $\phi$ , and  $d$ , in Figure 3.14(a). I generated thirteen 143-atoms SiO<sub>2</sub> supercells generated using both melt-and-quench and sequential back-bonding methods. I then studied the energy gain during secondary back-bonding in these models using Density Functional Theory. Here, regular PBE-based generalized gradient approximations were used for Exchange-Correlation energy due to computational limitations for large 143-atom supercells. Brillouin zone was sampled at the Gamma point by including plane-waves until ~1000 eV in the wavefunction basis.

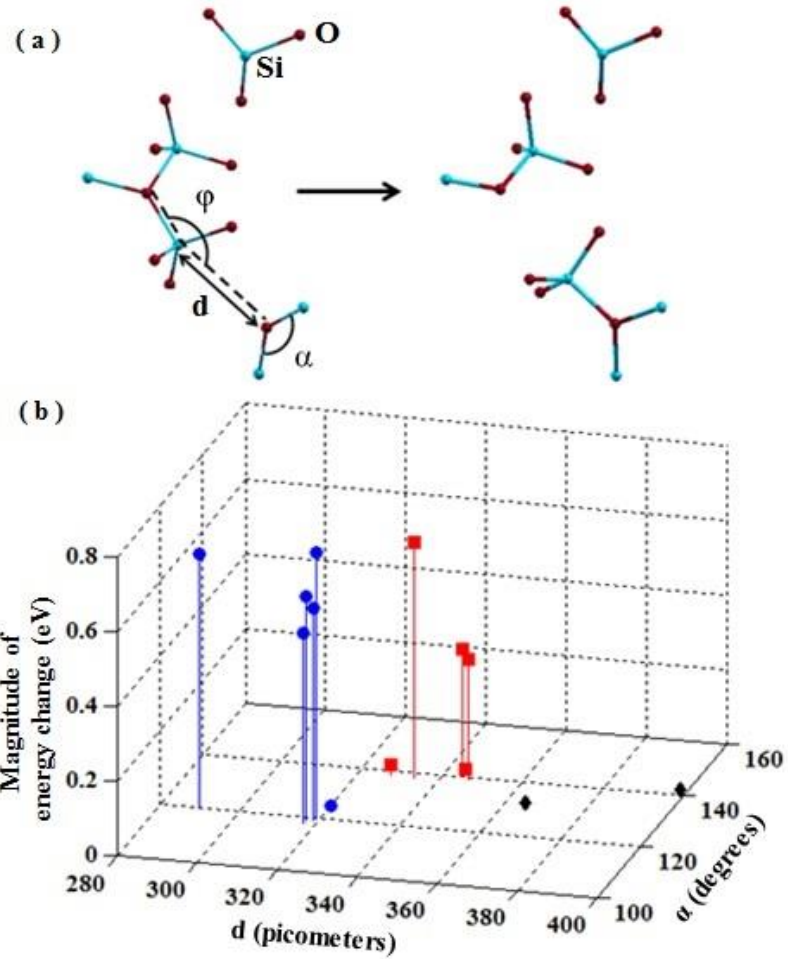


Figure 3.14: Additional structural transformations in hole trapped oxygen vacancies.  
 a) Secondary back-bonding leading to the migration of positively charged Si center,  
 b) energy gained through secondary back-bonding based on a statistics of oxygen vacancy hole traps. Red and blue represents positive and negative energy changes, respectively.

The results of the calculations are provided in Figure 3.14(b). The extent of stabilization achieved by the defect through secondary back-bonding depends on the local geometry of atoms. Based on our statistics, three distinct regions are seen in Figure 3.14(b), depending on  $\alpha$ , and  $d$  (independent of  $\phi$ , which ranges from  $161^\circ$  to

165°). Firstly, the defects could gain additional stability through secondary back-bonding (with *negative* energy change, up to  $\sim -0.7$  eV) for  $d < 3.2\text{\AA}$  and  $\alpha \sim 120^\circ$ . In general, this trend was observed in the ‘permanently electrically active’ oxygen vacancies. The thermal barrier for secondary back-bonding was found to be  $\sim 0.5$  eV (calculated at PBE level).

Secondly, the defects formed stable/metastable states (with energy change varying between 0 eV and +0.6 eV) for  $3.3\text{\AA} < d < 3.5\text{\AA}$ , and  $\alpha \sim 140^\circ$ . In general, this trend was seen in the ‘activated’ oxygen vacancies, discussed in Section 3.4.2. The NEB-calculated barrier for secondary back-bonding in hole-trapped vacancies was calculated to be  $\sim 0.8$  eV. Thirdly, secondary back-bonding was seen to be disallowed in oxygen vacancies for larger  $d$  ( $d > 3.5\text{\AA}$ ).

The +1/0 charge transition level of the secondary back-bonded structure was invariably seen to fall within the 4H-SiC bandgap (close to the conduction band edge). This suggests that the secondary back-bonded structure remains electrically active (switching oxide hole trap) similar to their back-bonded precursors. A direct comparison between the CTLs of back-bonded and secondary back-bonded structures is not made here due to the different supercell sizes and DFT levels used in their calculations. Additionally, the electron acquired during neutralization was seen to pair with the dangling lone electron of Si.

We now extend the NBTS-assisted trap activation model by including the secondary back-bonded states. The *complete* structural transformations of the ‘electrically inactive’ oxygen vacancies under hole and electron trapping are depicted in Figure 3.15. Further migration of the triply coordinated oxygen atom through

higher degree back-bonding is, however, assumed to be insignificant in the grand scheme of things during NBTS (due to the involved thermal barriers and typical NBTS duration).

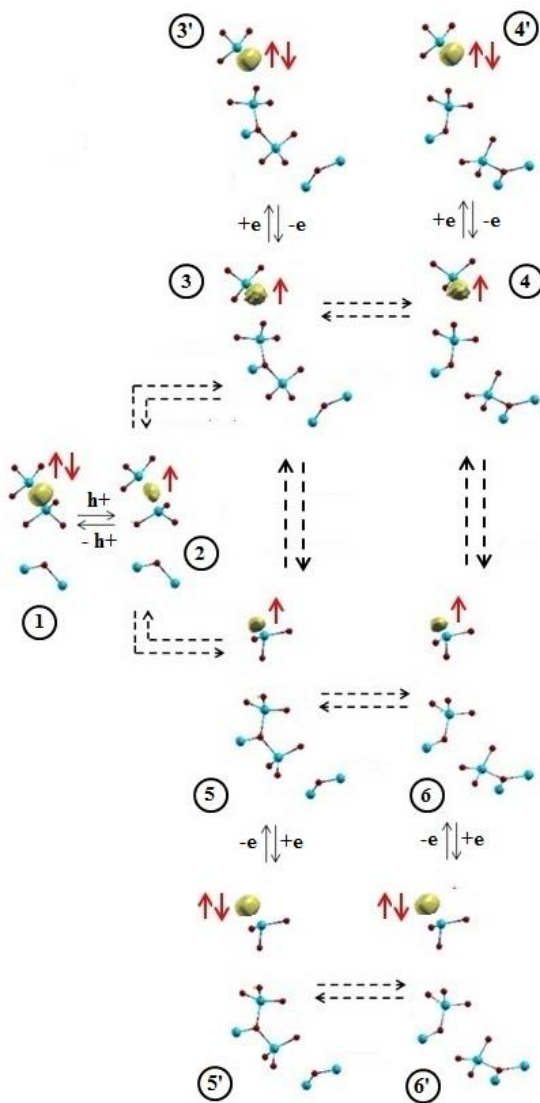


Figure 3.15: Comprehensive model for the activation of electrically inactive oxygen vacancies, including secondary back-bonding. The structural transformations during neutralization (electron capture) are also indicated. The shaded regions represent the calculated Electron Localization Function (ELF) isosurfaces at ELF=0.89, with the adjacent red arrow/s showing the type of localization (unpaired/paired).

### 3.5 Transient Modeling of Oxygen vacancy Hole Trap Activation

In this section, I perform detailed and quantitative transient simulations of the HTGB-induced threshold voltage instability in 4H-SiC MOSFETs. The Bias-stress-and-measurement sequence used is  $V_{th}$  measurements is given in Figure 3.16. The measurements were performed by the researchers at the Army Research Laboratory, Adelphi, MD [9].

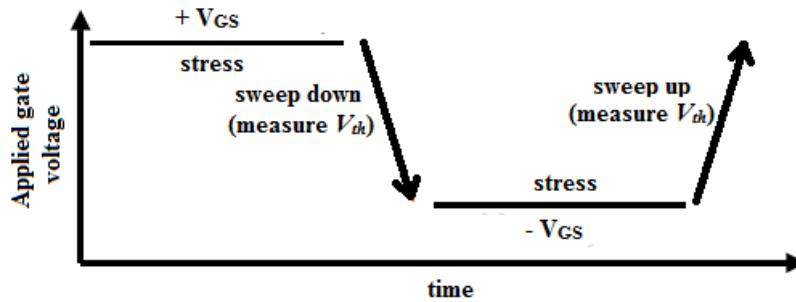


Figure 3.16: The HTGB stress-and-measure sequence used in the experimental measurement of threshold voltage instability in 4H-SiC power MOSFETs. The absolute threshold voltages are measured during the sweep up/down sequences, after a course of bias stress. The difference between the measured absolute threshold voltages is defined as the threshold voltage instability ( $\Delta V_{th}$ ).

During the application of the negative bias cycle of Figure 3.16, the electrically ‘inactive’ oxygen vacancies are converted into positively charged ‘electrically active’ hole traps, as described the hole-trap activation modeled described in the previous sections. This is accompanied by structural changes in the oxygen vacancies. During the positively bias stress cycle of Figure 3.16, the ‘activated’ oxygen vacancies are

neutralized immediately. Thus, the rates at which various positively charged states in the oxygen-vacancy hole trap activation model (shown in Figure 3.17) are populated would correlate with the measured  $V_{th}$  transients under NBTS. Additionally, during the PBTS cycle, they are instantaneously neutralized. It is worth mentioning that this work assumes the recently observed electron trapping during PBTS cycle (and associated positive  $V_{th}$  drifting) to be decoupled from hole trapping.

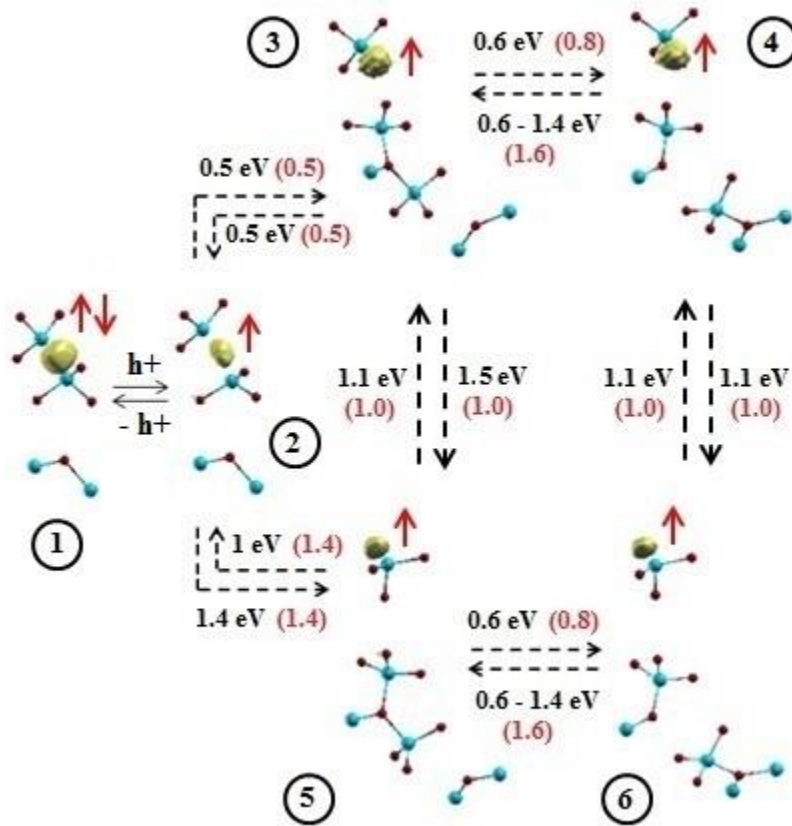


Figure 3.17: The hole trap activation model during NBTS. The thermal transformations in hole-trapped oxygen vacancies are indicated by dotted lines. The NEB-calculated barriers are indicated in black. The barriers used in the rate equation-based modeling are indicated within parenthesis in red. The various states are labelled within the circles.

The various positively charged states of oxygen vacancies that are activated during NBTS stressing is given in Figure 3.17. We model the kinetics of their formation using the following coupled differential equations.

$$\frac{dx_1}{dt} = -k_{12} \left\{ \exp \left( \frac{-E_{12}}{k_b T} \right) \right\} x_1 + k_{21} \left\{ \exp \left( \frac{-E_{21}}{k_b T} \right) \right\} x_2 \quad (3.8)$$

$$\begin{aligned} \frac{dx_2}{dt} = & - \left( k_{21} \left\{ \exp \left( \frac{-E_{21}}{k_b T} \right) \right\} + v_0 \left\{ \exp \left( \frac{-E_{23}}{k_b T} \right) \right\} + v_0 \left\{ \exp \left( \frac{-E_{25}}{k_b T} \right) \right\} \right) x_2 \\ & + k_{12} \left\{ \exp \left( \frac{-E_{12}}{k_b T} \right) \right\} x_1 + v_0 \left\{ \exp \left( \frac{-E_{32}}{k_b T} \right) \right\} x_3 \\ & + v_0 \left\{ \exp \left( \frac{-E_{52}}{k_b T} \right) \right\} x_5 \end{aligned} \quad (3.9)$$

$$\begin{aligned} \frac{dx_3}{dt} = & - \left( v_0 \left\{ \exp \left( \frac{-E_{32}}{k_b T} \right) \right\} + v_0 \left\{ \exp \left( \frac{-E_{34}}{k_b T} \right) \right\} + v_0 \left\{ \exp \left( \frac{-E_{35}}{k_b T} \right) \right\} \right) x_3 \\ & + v_0 \left\{ \exp \left( \frac{-E_{23}}{k_b T} \right) \right\} x_2 + v_0 \left\{ \exp \left( \frac{-E_{43}}{k_b T} \right) \right\} x_4 \\ & + v_0 \left\{ \exp \left( \frac{-E_{53}}{k_b T} \right) \right\} x_5 \end{aligned} \quad (3.10)$$

$$\begin{aligned} \frac{dx_4}{dt} = & - \left( v_0 \left\{ \exp \left( \frac{-E_{43}}{k_b T} \right) \right\} + v_0 \left\{ \exp \left( \frac{-E_{46}}{k_b T} \right) \right\} \right) x_4 + v_0 \left\{ \exp \left( \frac{-E_{34}}{k_b T} \right) \right\} x_3 \\ & + v_0 \left\{ \exp \left( \frac{-E_{64}}{k_b T} \right) \right\} x_6 \end{aligned} \quad (3.11)$$

$$\begin{aligned}
\frac{dx_5}{dt} = & - \left( v_0 \left\{ \exp \left( \frac{-E_{52}}{k_b T} \right) \right\} + v_0 \left\{ \exp \left( \frac{-E_{56}}{k_b T} \right) \right\} + v_0 \left\{ \exp \left( \frac{-E_{53}}{k_b T} \right) \right\} \right) x_5 \\
& + v_0 \left\{ \exp \left( \frac{-E_{25}}{k_b T} \right) \right\} x_2 + v_0 \left\{ \exp \left( \frac{-E_{65}}{k_b T} \right) \right\} x_6 \\
& + v_0 \left\{ \exp \left( \frac{-E_{35}}{k_b T} \right) \right\} x_3
\end{aligned} \tag{3.12}$$

$$\sum_{i=1}^6 x_i = 1 \tag{3.13}$$

Here, the initial trapping of the holes by the electrically ‘inactive’ Si-Si dimers is considered to be through Shockley-Reed-Hall tunneling. The thermally-assisted structural transformation process occurring in the hole-trapped vacancies is modeled as Arrhenius processes.

Since tunneling is an instantaneous process, the trap level associated with the ‘inactive’ Si-Si dimer defect is interpreted through its (0/+1) optical transition level [97], which is described in Section 3.2.2. I used hybrid DFT to evaluate the (0/+1) OTL to be located  $\sim 1.6$  eV ( $= E_{12}$ ) below the 4H-SiC valence band edge using equation (3.4). This could increase by  $\sim 0.3$  eV upon the application of the Lany-Zunger DFT correction (Section 3.2.1). In general, the coefficient  $k_{12}$  in equation (3.8) was calculated as [97]

$$k_{12} = k_p^c + k_n^e \tag{3.14}$$

where, the hole capture coefficient  $k_p^c$ , is given as,

$$k_p^c = p v_p^{th} \sigma_p T(z, E) \tag{3.15}$$

Here,  $p$  is the hole concentration in the channel,  $v_p^{th}$  is the hole thermal velocity ( $10^7$  cm/s), and  $\sigma_p$  is the hole trap cross-section of the Si-Si dimer ( $\sim 3 \times 10^{-14}$  cm<sup>2</sup> [97]).  $T$  ( $= 2.5 \times 10^{-2}$ ) is a coefficient that includes the field and depth dependence of hole tunneling into the trap. In this work, this is used as a fitting parameter, and I do not consider the variation in tunneling rate as a function of the distance of the trap from the interface. A relatively large value is chosen here to indicate that the oxide traps are located close to the interface. The hole concentration in the channel for the fermi level located at the Valence band edge of 4H-SiC substrate is assumed to be  $10^{21}$ /cm<sup>3</sup>. Overall,  $k_{12}$  is calculated to be  $7.5 \times 10^{12}$  per second. Here, the emission of electrons into the conduction band edge of 4H-SiC substrate from the deep oxide trap level is ( $k_n^e$  in equation (3.14)) considered to be negligible. Furthermore, hole emission from the oxide hole trap into the substrate ( $k_{21}$  in equation (3.8)) is considered to be negligible during the NBTS cycle.

The thermally-assisted structural transformation processes in hole-trapped oxygen vacancies are modeled using Arrhenius rate equations. The activation barriers pertaining to the structural transformations are first calculated using the NEB method described in Section 2.4. These NEB-calculated barriers are in reasonable agreement with the barriers used in the rate equations-based modeling (equations (3.8) to (3.13)). The NEB-calculated barriers, and those used in the rate equations are indicated in Figure 3.17.

In order to obtain the transients of the formation of various structural configurations of electrically ‘inactive’ oxygen vacancies under NBTS, I solved equations (3.8) to (3.13) simultaneously. The net time-dependent concentration of

accumulated positive charge was converted into shifts in threshold voltage using the following expression.

$$|\Delta V(t)| = \frac{q N (\sum_{i=2}^6 x_i(t))}{C_{ox}} \quad (3.16)$$

Here,  $N$  is the total density of electrically ‘inactive’ oxygen vacancies ( $\sim 2 \times 10^{18}/\text{cm}^3$ ) in the border region, and  $C_{ox}$  represents the oxide capacitance corresponding to a thickness of 50 nm.

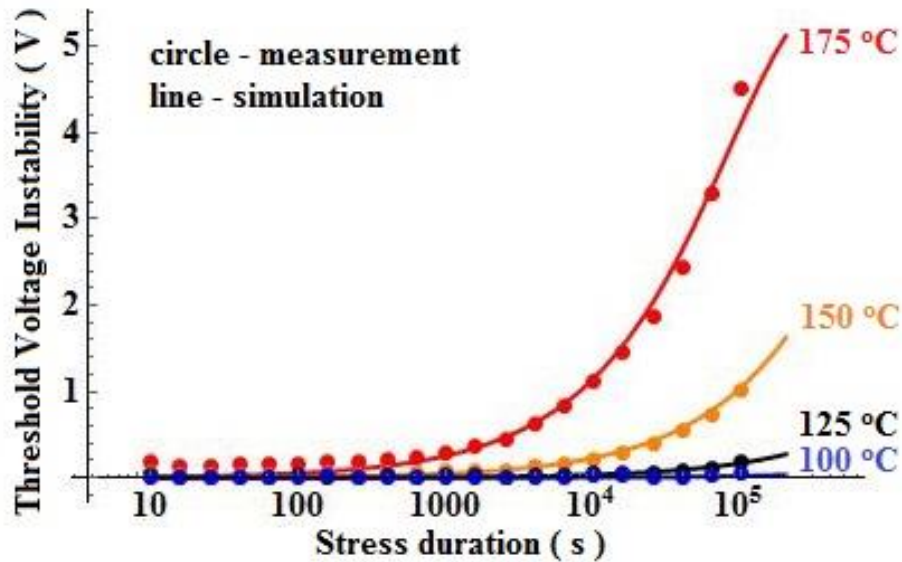


Figure 3.18: Simulation of the HTGB stress-assisted  $\Delta V_{th}$  transients in 4H-SiC MOSFET using the oxygen vacancy hole trap activation model. Circles represent experimental data points. The room-temperature contribution is subtracted from the measured threshold voltage instability at the indicated temperatures.

The calculated transients of  $\Delta V(t)$  in 4H-SiC power MOSFETs were seen to be in good agreement with the measured  $\Delta V(t)$  over time, for different temperatures [9].

This is depicted in Figure 3.18. This agreement serves to validate the HTGB-assisted oxygen vacancy hole trap activation model developed in this work.

### 3.6 Comparison with other Experimental Observations

In this section, I apply the oxygen-vacancy hole trap activation model to explain other electrical and Electrically Detected Magnetic Resonance (EDMR) results in 4H-SiC power MOSFETs. I also compare the model in 4H-SiC MOSFET with respect to that in Silicon MOSFETs.

#### 3.6.1 Long-term Threshold Voltage Instability

A fraction of the ‘electrically inactive’ dimer defects is expected to transform via path 2, overcoming a thermal barrier of  $\sim 2.2$  eV under high negative bias (when  $E_F=E_v$  in equation (3.7)), to form the ‘electrically active’ back-projected  $E_\gamma$ ’ hole traps (Figure 3.11). Again, DFT corrections [90] introduce an error bar of  $\sim 0.3$  eV. Upon neutralization (positive bias), these structures face a moderately high reverse barrier ( $\sim 0.8$  eV) to relapse to the ‘electrically inactive’  $E_\delta$ ’ configurations, unlike their forward-projected counterparts. We argue that these relatively long-lived defects are likely to manifest themselves in room temperature  $V_{th}$  instability measurements performed on 4H-SiC MOSFETs which are cooled rapidly to room temperature post HTGB stressing. Interestingly, recent experiments [9, 98] performed under similar conditions revealed increased  $V_{th}$  instability, which is in qualitative agreement with our model of generation of durable ‘electrically active’ back-projected  $E_\gamma$ ’ centers. Thus, it could be inferred that the NBTS-induced formation of back-projected  $E_\gamma$ ’

hole traps (path 2) plays a significant role in deteriorating the long-term reliability of 4H-SiC MOSFETs.

### 3.6.2 EDMR Observations in 4H-SiC Power MOSFETs

Recent Electrically Detected Magnetic Resonance (EDMR) results on negative bias-and-temperature stressed 4H-SiC MOSFETs have indicated considerable enhancement in oxygen-vacancy hole trap signatures with increasing temperatures [9, 70]. Additionally, the signature was seen to weaken when the sample was cooled to room temperature. Similar results were also observed in on-the-fly electron spin resonance experiments for negative bias-and-temperature stressed Si MOS [14]. Interestingly, the increase in  $E'$  signatures was seen only with *simultaneous* application of *both* bias and temperature stresses, and not with temperature stress alone [14]. In addition, recent electrical measurements on 4H-SiC MOSFETs also point to the inability of temperature stress alone (without bias) to cause significant worsening of  $\Delta V_{th}$  [9, 75]. In short, EDMR and electrical experiments indicate that *both* temperature and negative bias stresses are crucial for activation of additional hole traps in 4H-SiC MOSFETs.

The aforementioned behavior could be explained by the trap activation and deactivation model proposed in Section 3.4.2. From Figure 3.12, the low energy ‘inactive’ dimer ( $E_\delta$ ) centers are electrically activated as they access higher energy configurations like the  $E_\gamma$ . Negative bias enhances the trap activation process by monotonically lowering the Fermi level ( $E_F$ )-dependent activation barrier as  $E_F$  approaches the 4H-SiC valence band edge in accordance with equation (3.7). On the other hand, temperature enhances the activation rate by increasing the internal

thermal energy ( $k_bT$ ). However, temperature stress alone is unlikely to activate oxygen-vacancy hole traps as their various *neutral* structural configurations ( $E_\delta'$ ,  $E_\gamma'$ ) are relatively widely spaced in their energies, as shown in Figure 3.12. This model embodies the experimental observation that *both* temperature and negative-bias stresses are essential to activate additional oxygen-vacancy hole traps in 4H-SiC MOSFETs, as opposed to temperature alone [9, 14, 70, 75].

### 3.6.3 Comparison with Silicon MOSFETs

The types of oxygen vacancy defects described in this work are also expected to be present in Silicon MOSFETs. However, the alignment of Si bandgap with respect to that of SiO<sub>2</sub> is different from 4H-SiC. Specifically, Si valence band maxima (VBM) is reported to be located 4.4 eV above SiO<sub>2</sub> VBM [18, 99] as opposed to 2.9 eV in 4H-SiC [93]. This directly affects the electrical activities of various types of oxygen vacancies in Si MOSFETs.

The initial +1/0 CTL of the vacancies observed in Type 1 supercells, where neutral dimer  $E_\delta'$  centers spontaneously transform to positive forward-projected  $E_\gamma'$  structures, is located at 4.3 eV (Figure 3.9). This is 0.1 eV below Si valence band edge. Therefore, these defects are rendered ‘electrically inactive’ in Si MOSFETs unlike their 4H-SiC counterparts, where they are ‘permanently electrically active’. Using equation (3.7), the activation barrier for these ‘electrically inactive’ defects in Si MOSFETs is calculated as 0.1 eV. Application of Lany-Zunger DFT correction will increase this barrier by  $\sim 0.3$  eV. This is in reasonable agreement with previous observations [100]. On the other hand, the vacancies observed in Type 2 supercells (which are ‘activated’ during NBTS in 4H-SiC MOSFETs) are unlikely to be

‘activated’ in Si MOSFETs due to an extremely high activation barrier. In short, NBTS in 4H-SiC and Si MOSFETs *activates* oxygen-vacancy hole traps in low (Type 2) and high (Type 1) amorphous regions of SiO<sub>2</sub>, respectively.

### 3.7 Chapter Summary

In this chapter, I employed hybrid-functional Density Functional Theory to investigate the influence of local atomic environment on the electrical activity of near-interfacial oxygen vacancy centers in 4H-SiC MOSFETs. I classified these vacancies (Si-Si dimers) into ‘permanently electrically active’ and ‘electrically inactive’ centers, based on the location of their charge transition levels (CTL). Specifically, these vacancies introduced +1/0 CTL within and below the 4H-SiC bandgap, respectively.

The ‘permanently electrically active’ dimers and its higher energy configurations readily trap and de-trap holes in response to applied bias. Thus, these defect structures can be responsible for room temperature  $V_{th}$  instability observed in 4H-SiC MOSFETs.

On the other hand, ‘electrically inactive’ Si-Si dimers were seen to be unlikely to trap holes to cause significant  $V_{th}$  instability in 4H-SiC MOSFETs at room temperature. However, they could be converted into ‘electrically active’ higher-energy forward-projected and back-projected  $E_y$ ’ structures by the application of negative bias and temperature stress. Additional structural transformations like secondary back-bonding are also feasible. These excited configurations introduced +1/0 CTLs within the 4H-SiC bandgap which turned them into switching oxide hole traps. This explains the recently observed excessive aggravation of  $V_{th}$  instability in

4H-SiC MOSFETs which are bias-stressed at elevated temperatures ( $T > 100^\circ\text{C}$ ). I performed a transient modeling of this hole trap activation process, which correlated well with the measured time-dependence of HTGB-assisted  $V_{th}$  instability in 4H-SiC MOSFETs. This model also underlines the *simultaneous* role of both temperature and negative bias in the activation of oxygen-vacancy hole traps, which is in qualitative agreement with recent EDMR measurements.

## Chapter 4: Additional Reliability-limiting Defects, and Passivation Processes for Reliability Improvement

### 4.1 Background and Motivation

Oxygen vacancies are traditionally regarded as the key border hole traps responsible for  $V_{th}$  instability in 4H-SiC MOSFETs. However, given the more complex oxidation process of 4H-SiC and various post-oxidation chemical treatment of the interface, it becomes imperative to study additional candidate defects for possible hole trapping. Recently, single carbon interstitials at the 4H-SiC/SiO<sub>2</sub> interface in carboxyl configuration, where the interstitial C atom is double-bonded to a dangling oxygen and connected to two silicon atoms, have been proposed to be hole traps [23]. Such defects could arise from the carbon atoms that are released during high-temperature oxidation of 4H-SiC [11]. Alternatively, carboxyl defects could be formed through the trapping of CO molecules by oxygen vacancies in SiO<sub>2</sub> [101]. Previous density functional studies on the energetics of single carbon interstitials have found the carboxyl arrangement to be stable with low formation energy [23, 102]. While the electron trapping properties of this defect have been studied in the past [37], its hole trapping behavior has received limited attention to my knowledge. Experimentally, the existence of C-O bonds and Si-C-O linkages (a possible precursor to carboxyl defect [102]) at the 4H-SiC/SiO<sub>2</sub> interface has been suggested by XPS measurements [103]. Similarly, TEM and EELS studies have shown the interface to have a transition layer rich in Si-C-O bonds [24].

However, the post-oxidation annealing of 4H-SiC/SiO<sub>2</sub> MOS structures in Nitric oxide (NO) environment has been reported to mitigate threshold voltage instability [4, 6]. A possible reason for this could be the passivation of hole traps. However, other reports suggested increased hole trapping in nitrided 4H-SiC MOSFETs [27, 28]. Thus, the complete understanding on the effect of NO passivation on the device reliability continues to be elusive. Passivation processes like Hydrogen treatment comes with the risk of generating mobile H atoms or protons under NBTS, as described by the well-known Reaction-Diffusion model in Si MOSFETs.

In this chapter, I will use hybrid-functional DFT to investigate the role of alternative near-interfacial defects in 4H-SiC power MOSFET reliability. In this context, I propose a candidate defect – a single carbon interstitial in SiO<sub>2</sub> – that could act as a border hole trap leading to room-temperature Bias-Temperature Instability (BTI). I also present its structural and chemical bonding characteristics.

I will also investigate various passivation processes that could contain the effects of reliability-limiting defects in 4H-SiC power MOSFETs. More specifically, I will investigate the interaction between reliability-limiting defects (carbon interstitial and oxygen vacancy) and a host of chemicals like Nitric Oxide, molecular Hydrogen, and Fluorine. Other side-effects of these chemical treatments, like counter-doping, will also be discussed.

## 4.2 Hole Trapping by Carboxyl Defects

Recent models of 4H-SiC oxidation consider the emission of single carbon atoms into SiO<sub>2</sub>. Experiments have suggested the presence of a 4 to 5 nm long silicon oxycarbide (Si-O-C) interlayer between 4H-SiC and SiO<sub>2</sub> [24]. In this chapter, single carbon

interstitials in the SiO<sub>2</sub> side of the interface were considered. The generation of  $\alpha$ -SiO<sub>2</sub> was achieved through melt-and-quench molecular dynamics of  $\alpha$ -quartz crystal, as discussed in Section 2.5.2. The computational setup used in our calculations is outlined in Section 2.6. Additionally, the analysis carried out below is inclusive of the Lany-Zunger [90] finite-size DFT corrections.

#### 4.2.1 Formation and Charge Transition Levels of Carboxyl Defects

Since we are focusing on potential defect formation during the growth of SiO<sub>2</sub> on 4H-SiC, we begin by tracking a carbon atom that diffuses into SiO<sub>2</sub> during 4H-SiC oxidation using DFT-based molecular dynamics. This configuration is shown in Figure 4.1(a). Carbon atoms were seen to rapidly (within a pico-second) form Si-O-C-Si linkages in the oxide, due to negligible activation barrier, as shown in Figure 4.1(b). The presence of such linkages has been reported previously [23, 24, 103]. These linkages can then be converted to an energetically favorable carboxyl configuration, where carbon displaces oxygen and binds to two adjacent Si atoms. The displaced oxygen continues to be attached to carbon through a double bond. The Si-O-C-Si linkage and the carboxyl structure are shown on the left and right sides of Figure 4.2, respectively. The minimum energy pathway for the conversion of the Si-O-C-Si structure to the more stable carboxyl configuration, as calculated by nudged elastic band method [57] is also shown in Figure 4.2. The process was found to be exothermic with an energy release of 2 eV and activation energy of 0.5 eV. These thermodynamic and kinetic parameters support the existence of single carbon interstitials in carboxyl configuration in SiO<sub>2</sub>.

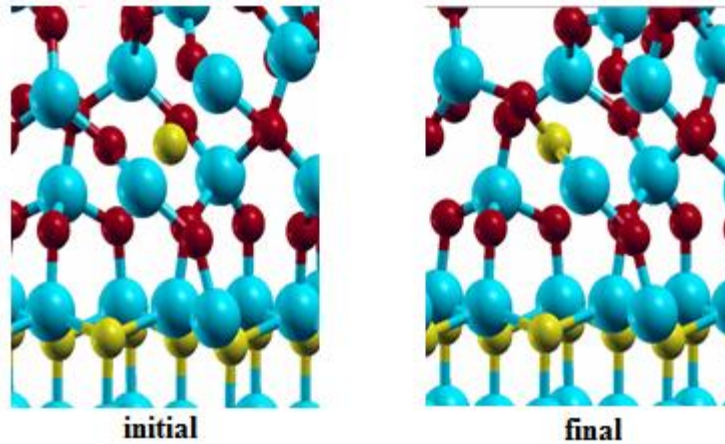


Figure 4.1: a) Configuration with a single carbon interstitial located at the 4H-SiC/SiO<sub>2</sub> interface, at the start of the quantum molecular dynamics (QMD) simulation, b) Si-O-C-Si bridge, which is rapidly formed, by the end of 1ps long QMD run.

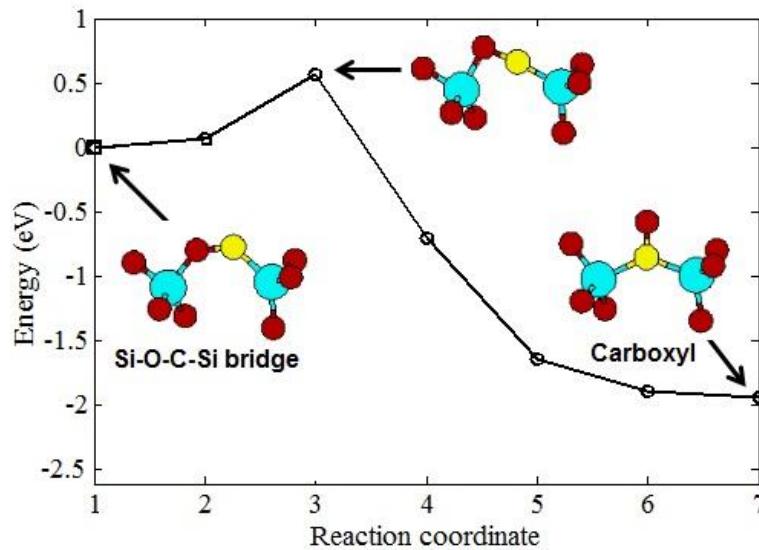


Figure 4.2: Minimum energy pathway for the formation of carboxyl defect from silicon oxycarbide (Si-O-C-Si) bridge in amorphous SiO<sub>2</sub>. The initial, saddle point and final configurations are given in the inset. Silicon - blue, Carbon - yellow, Oxygen - red.

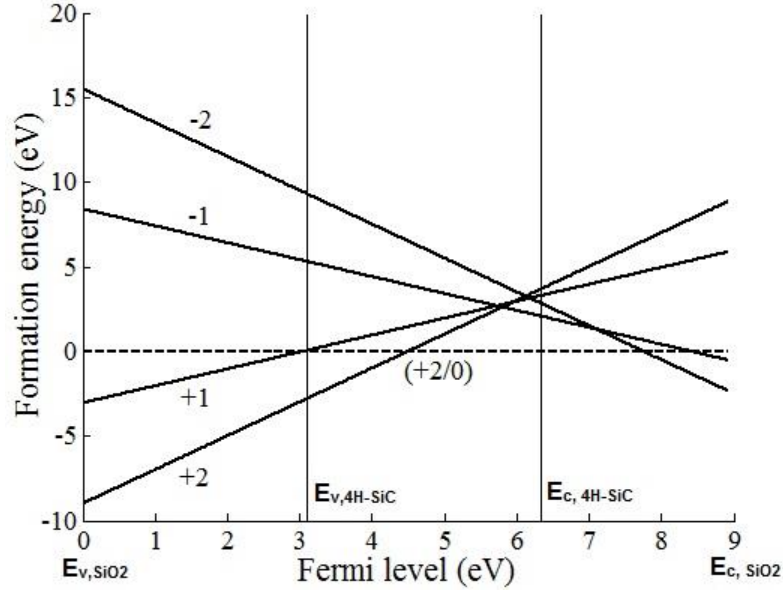


Figure 4.3: Formation energy of the carboxyl defect for various charge states in  $\text{SiO}_2$ . Energies are relative to the neutral state (dotted line). The (+2/0) charge transition level is shown. Theoretical 4H-SiC/ $\text{SiO}_2$  bandgap alignment, achieved in Section 3.3, is used here.

I then simulated the carboxyl defect in bulk  $\text{SiO}_2$  in various charge states  $-0, \pm 1$  and  $\pm 2$  – and calculated their formation energies as a function of Fermi level using equation (1). The result is given in Figure 4.3 with the formation energy of the neutral state taken as the reference, which is indicated by the horizontal dotted line. Makov-Payne scheme [89] has been applied for DFT finite-cell correction. The CTL between +2 and neutral charge state (indicated as (+2/0)) is seen in the 4H-SiC bandgap at  $E_v$  + 1.4 eV. The vertical lines in the figure indicate the location of the 4H-SiC bandgap with respect to  $\text{SiO}_2$  bandgap. The bandgap alignment details are mentioned in Section 3.3. Thus, the defect appears to be stable in a +2 state (trapped hole), and in a neutral state, for Fermi levels below and above (+2/0) CTL, respectively. This

suggests the role of the carboxyl defect as a border (near-interfacial) hole trap responsible for threshold voltage instability in 4H-SiC MOSFETs. The behavior of this defect is consistent with previous experiments which show a positive (negative) shift in 4H-SiC MOSFET threshold voltage after positive (negative) bias stress [4, 5, 7]. However, it is worth noting that due to the amorphous nature of SiO<sub>2</sub>, variations in atomic relaxations could lead to a spread in the calculated trap energy level.

#### 4.2.2 Structural Transformations of Carboxyl Defects upon Hole Trapping

We studied the structural transformations of the carboxyl defect during hole trapping. The structural parameters of the carboxyl defect in neutral, +1 and +2 charge states are shown in Figure 4.4. If we start with the neutral carboxyl defect as shown in Figure 4.4 (a), a hole capture leads to the singly positive intermediate state shown in Figure 4.4 (b); this is followed by a second hole capture which gives rise to the doubly positive state shown in Figure 4.4 (c). The structural changes upon hole capture like puckering and back-bonding, observable in Figure 4.4 (c), were seen to resemble that of oxygen vacancies (*E'* centers) in SiO<sub>2</sub> [16, 21]. Details of the structural and bonding transformations of the defect are discussed below.

The electron density distribution and chemical bonding in the carboxyl defect during hole capture was studied with the help of the Electron Localization Function (ELF), which was described in Section 3.4.1.

The ELF isosurfaces for the carboxyl defect in neutral, +1 and +2 charge states are given in Figure 4.5. In the neutral configuration of the defect, two distinct isosurfaces (at ELF = 0.88) can be seen on oxygen and pointing away from carbon as shown in Figure 4.5 (a). I interpret them to represent the localization domains of two

lone pairs. By comparison with the Lewis perspective of chemical bonding, I argue that the carbon-oxygen linkage is a double bond. In addition, the bond length is calculated to be 125 pm, which is consistent with a double C=O bond (Figure 4.4 (a)). The isosurface representing the localization domain of bonding electrons in the C=O bond is visible along the bond line for a lower ELF at 0.8, as shown in Figure 4.5 (b). These observations are in agreement with previous ELF studies on C=O [104]. Moreover, the electrons involved in Si-C bond appear to be localized along its bond line.

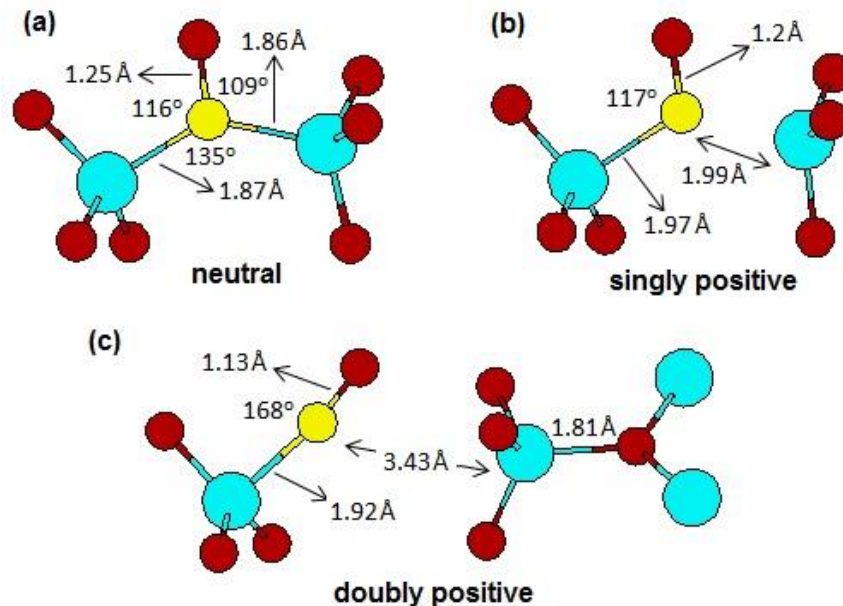


Figure 4.4: Structural transformations in carboxyl defect upon hole capture. a) Neutral state, b) +1 charged state, and c) +2 charged state. Silicon - blue, Carbon - yellow, Oxygen - red.

Upon the capture of first hole, the Si atom was seen to move away from the carbon during structural relaxation as shown in Figure 4.4 (b). Nevertheless, appreciable structural rearrangement was not observed. It seems reasonable here that

the carbon is likely to share its unpaired electron with Si. However, this configuration is intermediate as indicated by its formation energy in Figure 4.3.

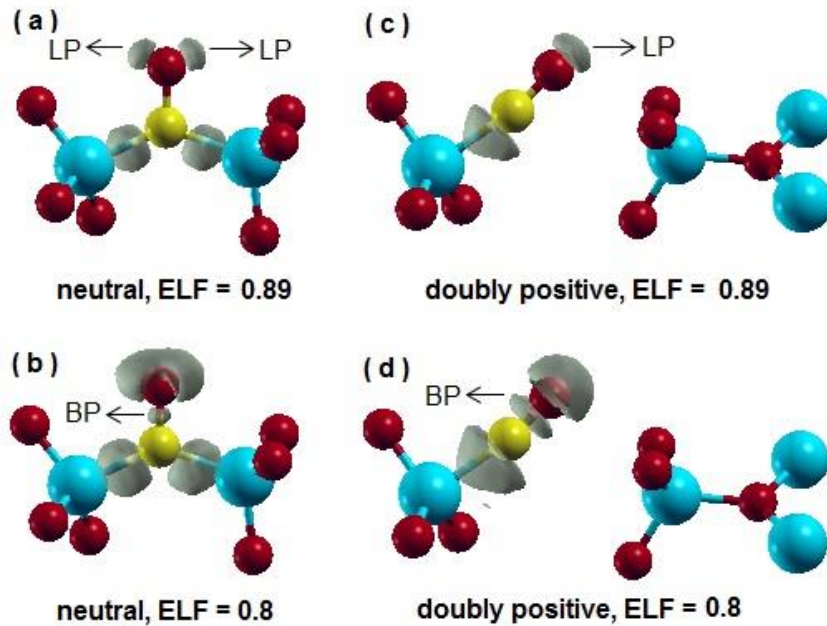


Figure 4.5: Electron localization function isosurfaces at two isovalues for the carboxyl defect in its stable neutral and doubly positive charge states. High isovalue is chosen to identify the localization domains of lone pairs (LP) on oxygen. Low isovalue reveals the localization of bonding pairs (BP) in the carbon-oxygen bond. a) ELF = 0.89 and neutral state, b) ELF = 0.8 and neutral state, c) ELF = 0.89 and +2 state, and d) ELF = 0.8 and +2 state. Only the ELF around the carboxyl defect is shown. Silicon - blue, Carbon - yellow, Oxygen - red. Isosurfaces are in grey.

The defect was seen to capture a second hole to achieve stability through significant structural relaxation. The resulting bonding in the defect is analyzed through its ELF. At ELF=0.88, a single isosurface could be observed on oxygen in

Figure 4.5 (c), which I interpret as the localization domain of a lone pair. Thus, it can be inferred that the carbon is bonded to oxygen through a triple bond in +2 state of the defect. This conclusion is supported by the calculated carbon-oxygen bond length of 113 pm, which compares well with the  $C\equiv O$  bond length in carbon monoxide. Furthermore, the calculated  $Si-C\equiv O$  angle is almost linear indicating a  $sp$  hybridized carbon. For  $ELF=0.8$ , an isosurface representing the localization domain of bonding electrons could be seen along the bond line in Figure 4.5 (d). In short, we argue that the carboxyl oxygen atom donates one of its lone pair of electrons to form a triple bond with the carbon atom upon double hole capture. This satisfies the basic octet rule which typically implies stability. In addition to this bonding rearrangement, the positively charged Si was seen to move away significantly from the carbon atom and backbond with an electronegative lattice oxygen atom (Figure 4.4 (c)). This gives rise to a puckered configuration, as described previously in the case of positively charged oxygen vacancies, resulting in structural relaxation. We propose that the triple bond formation and puckering serve to lower the energy of the carboxyl defect allowing its +2 charge state to be energetically favorable.

It is worth mentioning that the carboxyl defect in its stable +2 charge state has no unpaired electron. This makes the defect invisible to electron spin resonance (ESR) spectroscopy [74]. In contrast, oxygen vacancies, which are stable or metastable in +1 state with an unpaired electron, are detected in ESR measurements [13, 14].

### 4.3 Mitigation of Reliability-limiting Defects

In this section, I investigate the interactions between carbon- and oxygen-related hole traps and various passivants like Nitric Oxide (NO), molecular hydrogen, and

Fluorine. This is done using quantum molecular dynamics simulations, which is described in Section 2.3. The implications of these chemical treatments on the reliability of 4H-SiC MOSETs are also discussed.

#### 4.3.1 Effect of Nitric Oxide on Carboxyl Hole Traps

During 4H-SiC MOS processing, 4H-SiC/SiO<sub>2</sub> interfaces are annealed, typically in Nitric Oxide (NO), post oxidation to passivate interface defects and improve effective channel electron mobility [45]. In this section, I describe the effect of NO passivation on near-interfacial carboxyl defects located in the oxide. Using quantum molecular dynamics (QMD) simulations, I directly observed the removal of carboxyl defects through the formation of isocyanate (NCO) molecules.

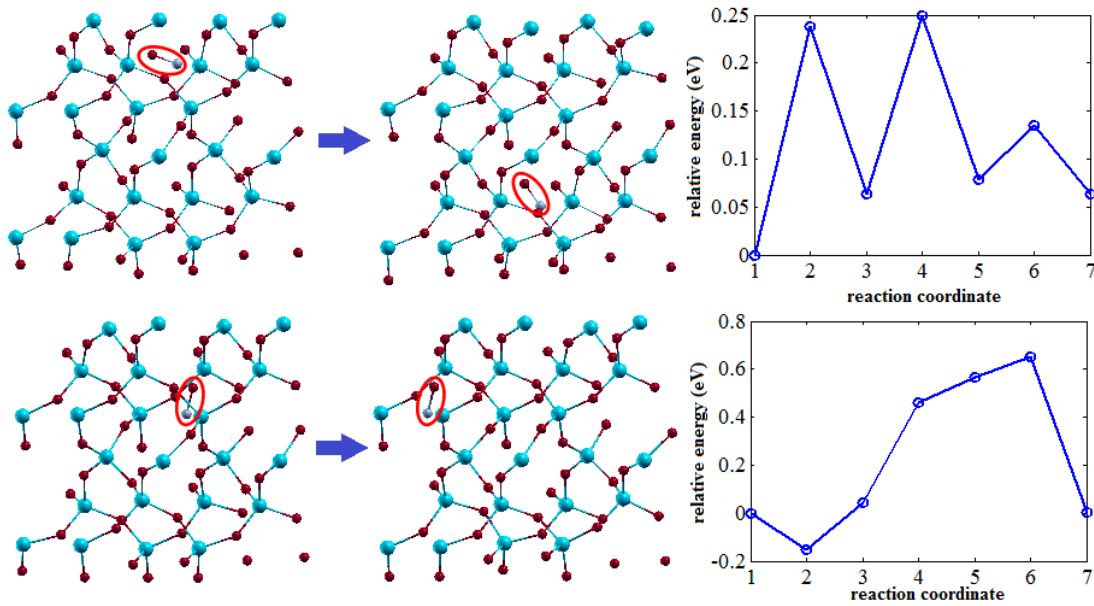
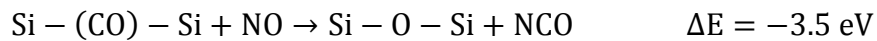


Figure 4.6: Diffusion of NO in along two paths in a-SiO<sub>2</sub>, and its NEB-calculated minimum energy pathways. The NO molecule is circled.

Firstly, I used NEB calculations to study the diffusion of NO molecule in a-SiO<sub>2</sub>. Owing to the amorphous nature of SiO<sub>2</sub>, two different directions were chosen for studying NO diffusion, as shown in Figure 4.6. The NEB-calculated diffusion barriers were seen to vary from 0.25-0.7 eV. Subsequently, I used canonical ensemble QMD simulations to track the initial stages of chemical reactions between the defect and nitric oxide molecule. Considering the computational time required for a reasonably long QMD simulation, I used regular PBE functionals in my calculations instead of hybrid functionals. The interaction between the defect and NO molecule was studied for 5 ps in steps of 2 fs at typical NO anneal temperature of 1400 K. Owing to the ‘large’ diffusion barrier of NO molecule in a-SiO<sub>2</sub> (in view of the difficulty to observe NO diffusion in the short duration of 5 ps for which QMD is carried out), the time required for it to find the right orientation for the reaction could be large. In order to overcome this difficulty and avoid prohibitively long QMD simulations, I tracked the nitric oxide molecule in the proximity of the carboxyl defect in four different configurations. Among them, two configurations, which are shown in Figures 4.7(a) and 4.7(b), readily initiated reactions with the carboxyl defect. The arrangement in Figure 4.7(a) added N and O separately between the two Si-C bonds (Figure 4.7(c)). On the other hand, the configuration in Figure 4.7(b) advanced *via* the incorporation of NO molecule between Si and C atoms, as shown in Figure 4.7(d). However, both the reaction routes resulted in the elimination of carboxyl defect through isocyanate (NCO) formation, as shown in Figure 4.7(e). The overall reaction was determined to be exothermic as



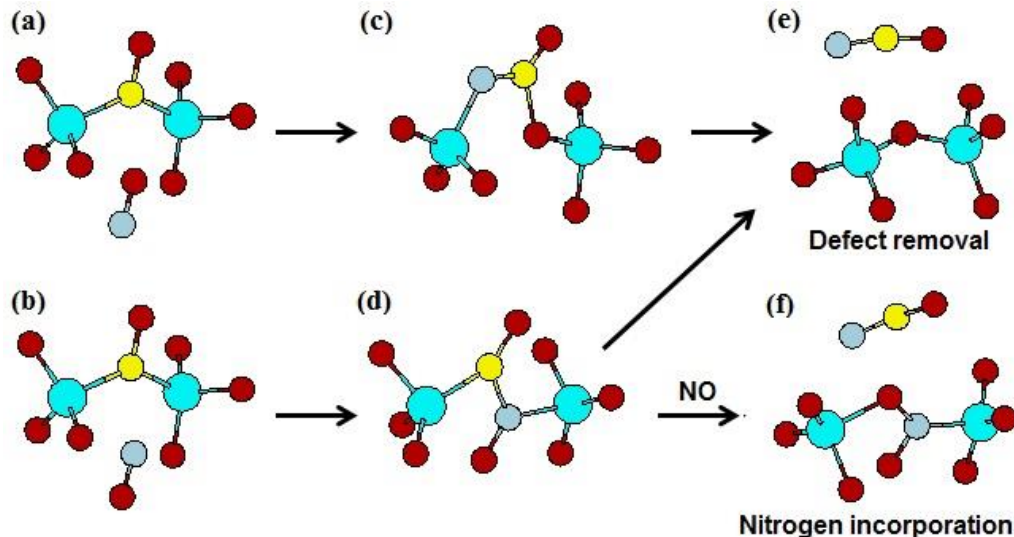


Figure 4.7: The mechanism of NO passivation of carboxyl defect. (a) - (e) represents various structural configurations during the defect removal. (f) shows Nitrogen incorporation in the SiO<sub>2</sub> lattice. Silicon - blue, Carbon - yellow, Oxygen - red, Grey - Nitrogen.

In short, the mechanism of carboxyl defect removal by NO strongly depends on the local atomic environment. The process was seen to occur rapidly, indicating that passivation is limited by the diffusion of NO molecules in SiO<sub>2</sub>.

Under NO rich conditions, the configuration in Figure 4.7(d) was observed to interact with a second NO molecule to incorporate Nitrogen in SiO<sub>2</sub> lattice. This is accompanied by NCO emission, as seen in Figure 4.7(f).



NCO Removal: I tracked the fate of NCO molecule released into the SiO<sub>2</sub> interstitial space during the carboxyl defect passivation. While the NCO molecule has been observed to hop between Si atoms in the interstitial space with an activation barrier of ~ 0.2 eV, it is unlikely to diffuse out owing to its large size. A more likely

scenario would be the reaction between NCO and NO inside the interstitial space to give N<sub>2</sub> and CO<sub>2</sub> [105, 106]. I studied the energetics and kinetics of this reaction in SiO<sub>2</sub> using NEB calculations. The calculated minimum energy pathway for the reaction is given in Figure 4.8. The formation of nitrosyl isocyanate (ONNCO), followed by a cyclic intermediate in a-SiO<sub>2</sub> interstitial space was observed during the process [105, 106]. The configurations of these complexes are shown in Figure 4.8. The overall reaction was found to be exothermic with an energy release of ~ 3.2 eV.

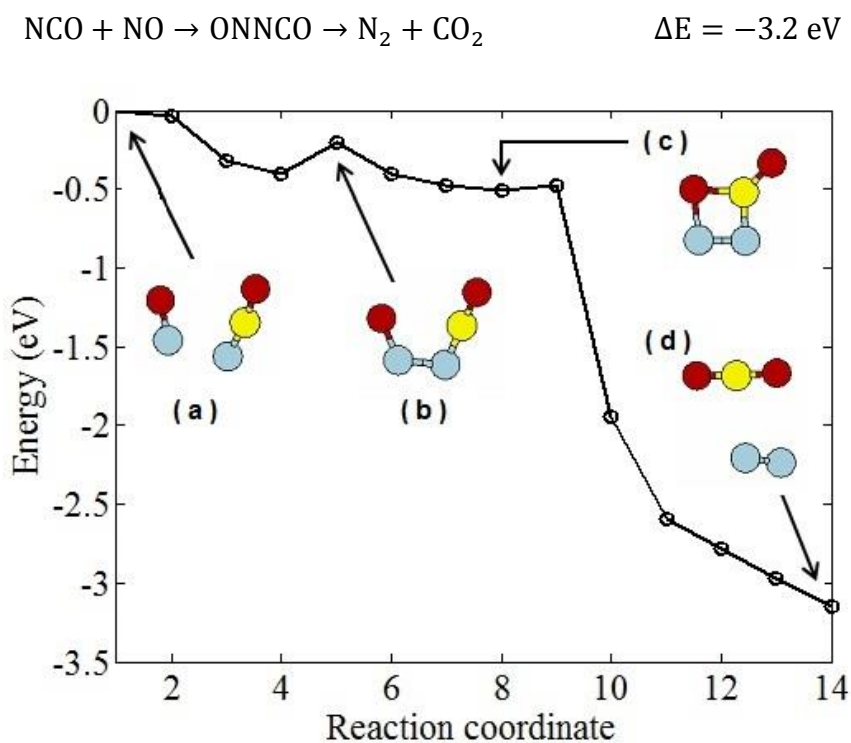


Figure 4.8: The NEB-calculated minimum energy pathway for the reaction between NCO and NO to give N<sub>2</sub> and CO<sub>2</sub> in SiO<sub>2</sub> void. Lattice atoms are not shown. (a) initial configuration with NCO and NO, b) intermediate nitrosyl isocyanate (ONNCO), (c) configuration of cyclic intermediate, and (d) final products, N<sub>2</sub> and CO<sub>2</sub>. All the components are unconnected to the SiO<sub>2</sub> lattice. Silicon - blue, Carbon - yellow, Oxygen - red, Grey- Nitrogen.

The activation barrier for the above reaction was calculated to be  $\sim 0.2$  eV (Figure 4.8). While this barrier could increase upon the use more accurate hybrid functional NEB-calculations, the reaction is generally inferred to be relatively rapid during post-oxidation annealing. This minimizes the possibility of NCO molecules introducing new defects.

In general, NO passivation appears to be effective in mitigating threshold voltage instability arising from carboxyl defects in 4H-SiC MOSFETs.

#### 4.3.2 Effect of Nitric Oxide on Oxygen Vacancy Hole Traps

In my QMD simulations, oxygen vacancies were seen to readily trap NO molecules to form Si-[NO]-Si structures in a-SiO<sub>2</sub>. Here, the nitrogen atom, with dangling oxygen, is connected to two Si atoms, as shown in Figure 4.9. In this dissertation, I call such configurations as ‘Nitroxyl’ structures, (in keeping with the nomenclature for carboxyl defects). Furthermore, similar structural configurations could also originate by the spontaneous incorporation of atomic Nitrogen into the oxide lattice. The minimum energy pathway for this process is depicted in Figure 4.10. I argue that, near the interface, such structures could manifest themselves as a Silicon-oxynitride interlayer, as observed in recent XPS measurements [107].

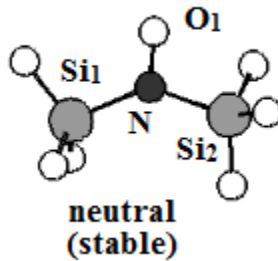


Figure 4.9: The basic nitroxyl defect configuration in its neutral state.

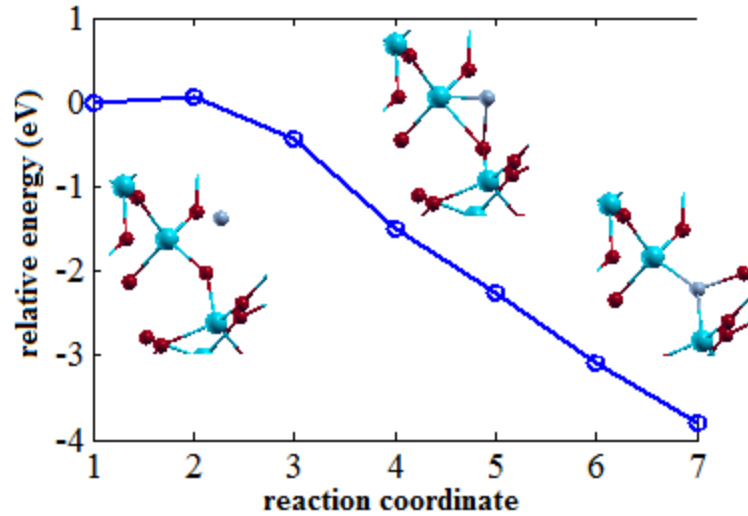


Figure 4.10: Minimum energy pathway for the rapid formation of nitroxyl configuration from a nitrogen interstitial in bulk  $\alpha$ -SiO<sub>2</sub>.

Next, I investigate the structural and electrical properties of ‘nitroxyl’ and other derivative structures through their CTLs, and analyze their implications on 4H-SiC MOSFET reliability. Upon hole capture during NBTS, the basic nitroxyl structure (in Figure 4.9) could transform into various higher energy derivative configurations through Si back-bonding and subsequent back-bond migration (secondary back-bonding), as in oxygen vacancy defects. These derived configurations are depicted in Figure 4.11. I calculated the formation energies of these excited states as a function of device Fermi level, which is also shown in Figure 4.11. Clearly, the higher energy configurations (which involve secondary back-bonded hole-trapped states) prefer to remain in positively charged state for all Fermi levels or applied bias (indicated as black lines in Figure 4.11). Thus, they tend to act like fixed positive charges that shift the threshold voltage negatively. However, lower energy configurations (which are singly back-bonded when positive, but do not relapse to basic neutral nitroxyl upon

neutralization) are seen to switch charge states depending on the Fermi level, as indicated in red in Figure 4.11. Thus, NO passivation could adversely affect device reliability [27, 28] although they are effective in removing other reliability-limiting defects like the carboxyl defects.

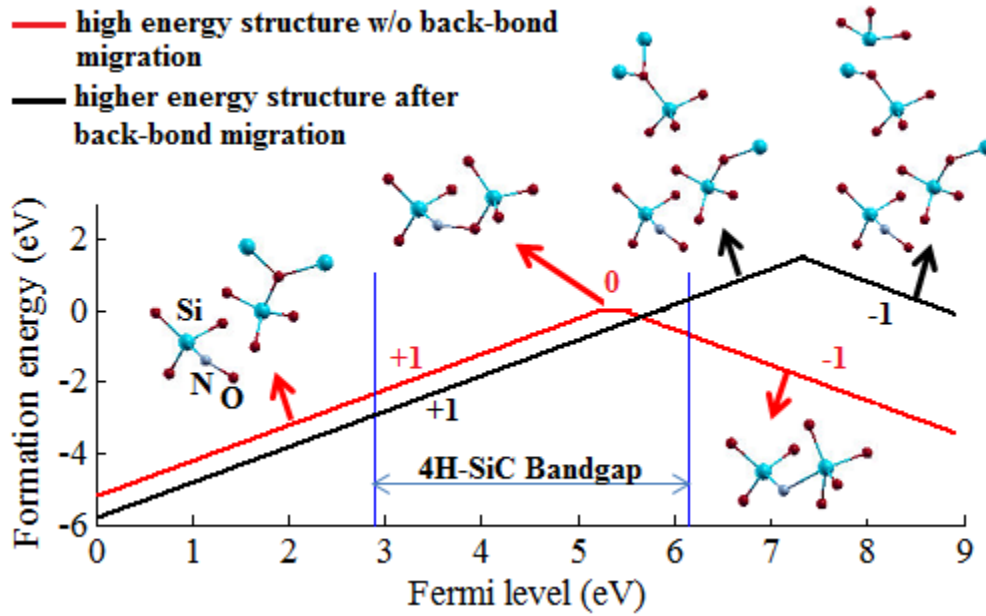


Figure 4.11: Higher energy configurations of the nitroxyl structure achieved during NBTS, and their formation energies in various charge states as a function of Fermi level.

#### 4.3.3 Implications of NO Treatment on 4H-SiC MOSFET Reliability

Above analysis could throw some light on the conflicting results reported on the reliability of NO passivated 4H-SiC MOSFETs. For example, recent electrical experiments have revealed improvements in threshold voltage instability in NO-annealed 4H-SiC MOSFETs [4, 6]. This is potentially due to the mitigation of

carboxyl defects during NO passivation. A reduction in the near-interfacial carbon concentration due to NO treatment was also recently observed in XPS measurements by Prof. Salamanca-Riba's group at UMD [108]. Additional reasons for this improvement could also be the reduction of interface traps in nitrated 4H-SiC MOSFETs.

However, other reports have indicated increased hole trapping, and potential reliability worsening in nitrated 4H-SiC MOSFETs [27, 28]. This is potentially because of a large number of nitroxyl-derived configurations, shown in Figure 4.11. They introduce varying amounts of  $V_{th}$  instability depending on the experimental conditions. For example, measurements done at extreme conditions like very high voltage and radiations are likely to create more of these high energy nitroxyl-derived configurations, which could form additional nitrogen-related fixed positive charges or switching oxide traps.

In short, the net effect of NO treatment on the reliability of 4H-SiC MOSFETs appears to depend on the relative dominance of various competing mechanisms. Further efforts are required to quantify such mechanisms arising from NO treatment.

#### 4.3.4 Other Effects of NO Treatment on 4H-SiC MOSFETs – Nitrogen Counter-doping

Nitrogen incorporation at the 4H-SiC/SiO<sub>2</sub> interface has been experimentally observed in recent XPS experiments [107]. This process - by which Nitrogen atoms form a very thin layer of donor dopants at the 4H-SiC surface - is called counter-doping. This process is believed to improve the effective channel mobility in NO-

passivated 4H-SiC MOSFETs [46]. I investigated this phenomenon using DFT, and my observations are given below.

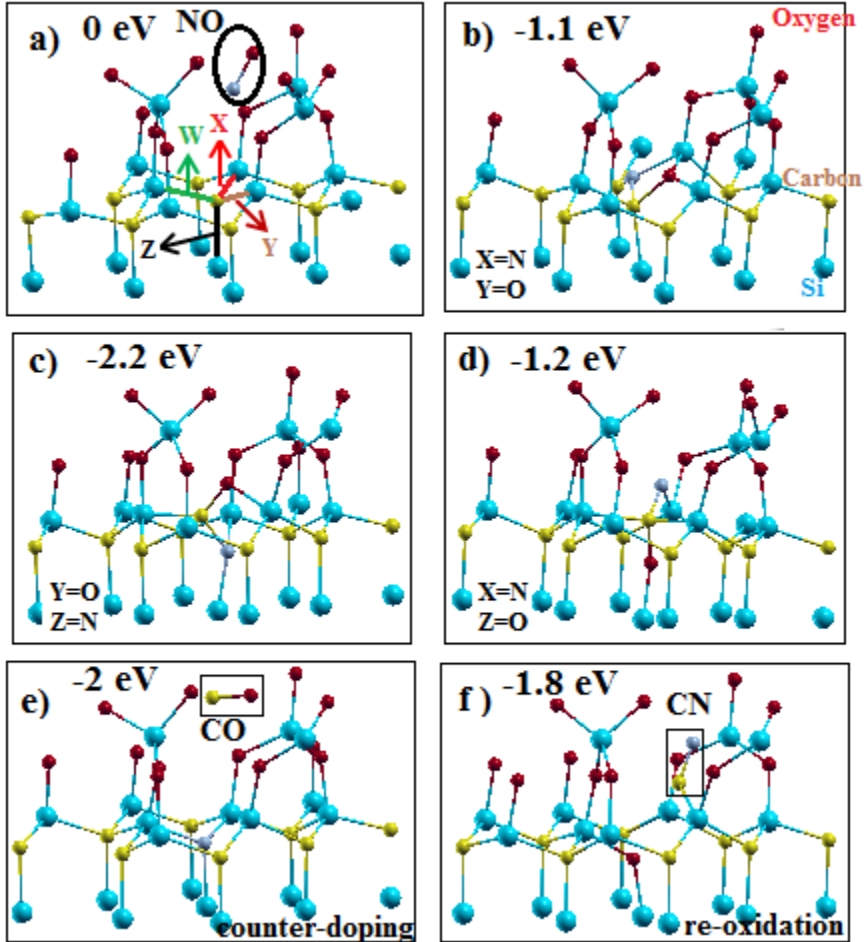


Figure 4.12: a) Incorporation of NO into 4H-SiC surface at the interface, b), c), d) various resulting configurations with their relative energies. The most feasible path results in e) counter-doping, f) re-oxidation.

In order to study the incorporation of N atoms in 4H-SiC substrate, I adopted the following approach. I incorporated NO into 4H-SiC surface at the interface in various possible locations (marked W, X, Y, Z in Figure 4.12(a)) and studied their energetics

to identify the most feasible process. The ground state energy was calculated using DFT at a PBE level. The introduction of N atom in location X, and O atom in location Y (as shown in Figure 4.12(b)) appears to be least favored. On the other hand, the introduction of the N atom in location marked Z, and O atom in location Y (Figure 4.12(c)) appears to be energetically most favored. Subsequent elimination of CO molecule from this structure leads to the substitution of N at the C site, leading to counter-doping [46], and increased effective mobility (Figure 4.12(e)). On the other hand, introduction of O atoms in location Z and Nitrogen in location X (Figure 4.12(d)) leads to re-oxidation through elimination of  $C\equiv N$  (Figure 4.12(f)).

In short, the substitution of C atoms in 4H-SiC substrate by N atoms was found to be energetically feasible. This counter-doping effect could lead to enhancement in effective carrier mobility. Expectedly, the re-oxidation of 4H-SiC substrate was also found to be feasible during high-temperature NO treatment.

#### 4.3.5 Effect of Molecular Hydrogen Treatment on Carboxyl Hole Traps

I investigated the effects of  $H_2$  treatment on hole trapping by carboxyl defects. My 5ps long QMD simulation of  $H_2$  treatment resulted in bonding arrangements shown in Figure 4.13(a) – consistent with previous density functional study [109]. I further explored the stability of the  $H_2$  treated carboxyl defect by calculating its formation energy in various charge states as a function of chemical potential using equation (3.2). The result is shown in Figure 4.14. A (+2/0) charge transition level (CTL) was observed at 1.1 eV above the 4H-SiC valence band maximum. Makov-Payne DFT-correction scheme was used here. This indicates that the defect would be stable in +2 and neutral state for Fermi levels below and above the CTL, respectively. In other

words, the H<sub>2</sub> treated carboxyl defect continues to act like a border hole trap similar to the original carboxyl defect in SiO<sub>2</sub>.

The structural transformations of the H<sub>2</sub> treated carboxyl defect during hole capture process were seen to closely resemble that of carboxyl defect. The configurations of the defect in its neutral, +1 and +2 charge states are depicted in Figure 4.13. The bond angles and bond lengths are shown in the figure. Significant puckering and Si-O backbonding was observed upon double hole capture.

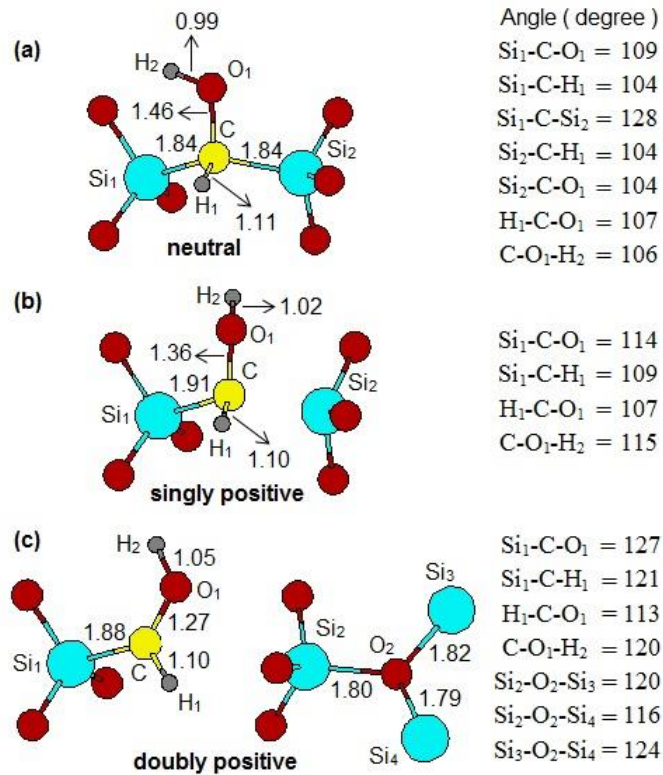


Figure 4.13: Structural transformations in H<sub>2</sub> passivated - carboxyl defect upon hole capture. a) Neutral state, b) +1 charged state, and c) +2 charged state. Bond lengths are indicated along the bonds in angstroms. Silicon - blue, Carbon - yellow, Oxygen - red, Hydrogen - grey.

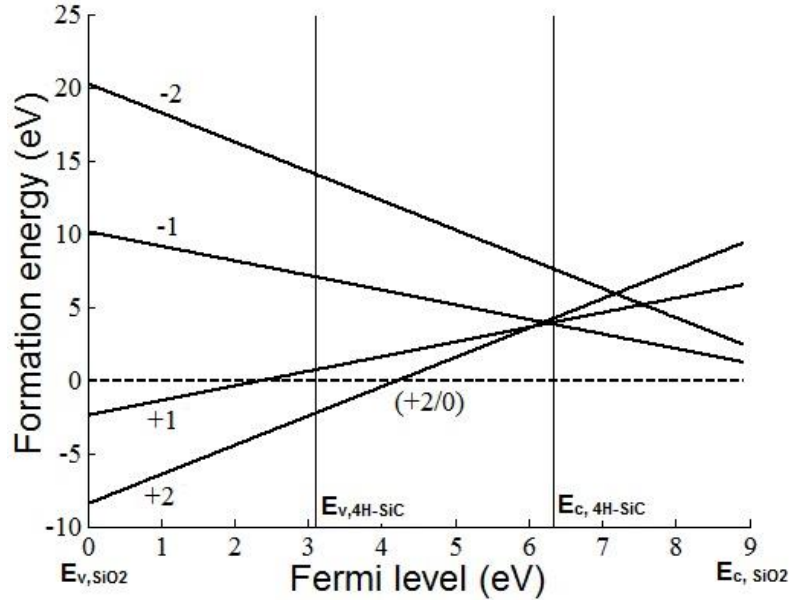


Figure 4.14: Formation energy of H<sub>2</sub>-passivated carboxyl defect in various charge states in SiO<sub>2</sub>. The energy of the neutral defect is taken as the reference (dotted line). The (+2/0) charge transition level is marked. 4H-SiC bandgap exists in between the vertical lines.

As in the case of the carboxyl defect, I analyzed the nature of chemical bonding using electron localization functions (ELF). For the neutral state, two distinct high-ELF isosurfaces (at ELF = 0.9) on the oxygen atom indicate two lone pairs as shown in Figure 4.15(a). Similarly, the isosurfaces representing single bonding pairs between O-H, C-H and C-Si are also seen along the bond line. These observations lead us to deduce a single bond between carbon and oxygen. However, the localization of C-O bonding pair is visible only at a lower ELF of 0.8 (Figure 4.15(b)). In addition, the calculated bond lengths compared well with the inferred bond orders.

Upon the capture of the first hole, the positively charged Si atom was seen to move away from the carbon atom (by  $\sim 15$  pm), as was the case with the carboxyl defect (Figure 4.13(b)). The lone electron of carbon appeared to remain localized between C and Si. A reduction in the C-O bond length was observed, indicating a redistribution of electron density around C and O atom. However, +1 state appears to be intermediate according to Figure 4.14.

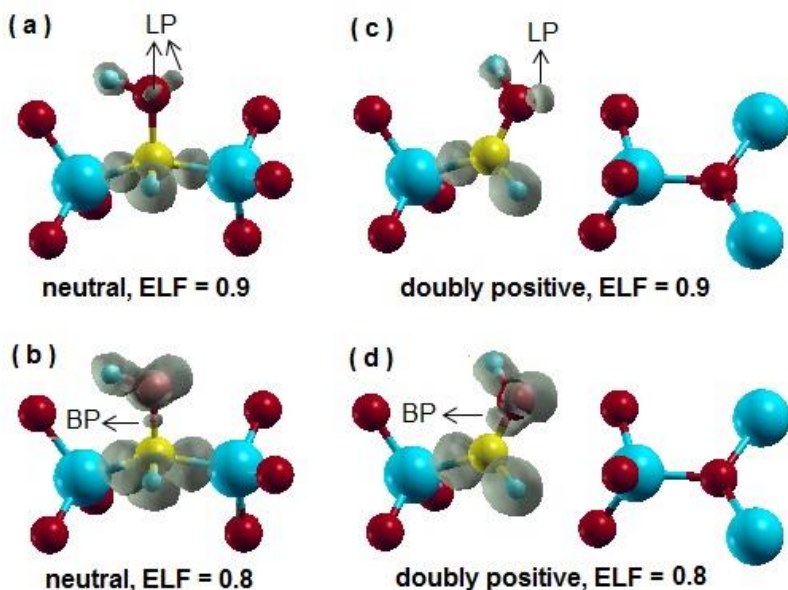


Figure 4.15: Electron localization function isosurfaces at two isovalues for the  $H_2$  passivated - carboxyl defect in its stable neutral and doubly positive charge states. High isovalue is chosen to identify the localization of lone pairs (LP) on oxygen. Low isovalue identifies the localization domains of bonding pairs (BP) in the carbon-oxygen bond, a) ELF = 0.9 and neutral state, b) ELF = 0.8 and neutral state, c) ELF = 0.9 and +2 state, and d) ELF = 0.8 and +2 state. Only the ELF around the defect is shown. Silicon - blue, Carbon - yellow, Oxygen - red, Hydrogen - small blue. Isosurfaces are in grey.

The carbon atom loses its dangling electron during the capture of the second hole. However, the electron-rich carboxyl oxygen donates a lone pair to form a double bond with carbon. This is evident from the single lone pair isosurface on the O atom at ELF= 0.9 (Figure 4.15(c)). The bonding pair localization domain is visible along the bond line at a lower ELF of 0.8, as seen in Figure 4.15(d). Additionally, the carbon-oxygen bond length corresponds to that of a double bond. The bond angles around carbon sums up to  $360^\circ$ , pointing to a planar arrangement stemming from its  $sp^2$  hybridization. Simultaneously, significant puckering of the positive Si atom ( $\sim 122$  pm from C) was observed, resulting in its back-bonding with an electronegative lattice oxygen atom (Figure 4.13(c)). This behavior is similar to that of the carboxyl defect and the  $E'$  center upon hole trapping. I argue that the structural relaxations associated with puckering and C=O formation provides stability to the  $H_2$  treated carboxyl defect in its +2 charge state, and renders it an ESR invisible hole trap in the lower half of 4H-SiC bandgap. In short, my calculations indicate that  $H_2$  passivation is unlikely to improve threshold voltage instability in 4H-SiC MOSFETs. They are likely to affect the device in the same way as the original carboxyl defects.

#### 4.3.6 Effect of Fluorine Treatment on Carboxyl and Oxygen Vacancy Hole Traps

I studied the effect of Fluorine passivation of carboxyl and oxygen vacancy hole traps using quantum molecular dynamics which lasted for 5ps. My results indicate that Fluorine passivation could be very effective in mitigating threshold voltage instability originating from carboxyl and oxygen vacancy hole traps.

The treatment with Fluorine was observed to remove CO from the carboxyl defect in my molecular dynamics simulations. This is possible due to very high Si-F bond

energy. The resulting configuration, depicted in Figure 4.16(a), shows F atoms bonded to two Si atoms. Additionally, Fluorine was also seen to passivate oxygen vacancies in the similar manner [110], leading to the structure shown in Figure 4.16(a).

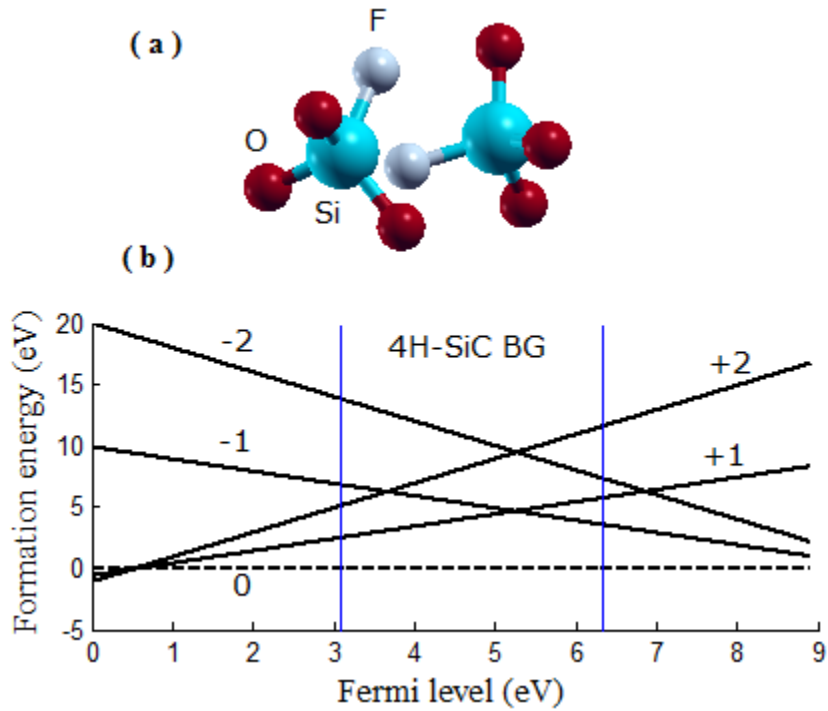


Figure 4.16: a) The structure resulting from Fluorine passivation of carboxyl or oxygen vacancy hole trap, b) Formation energy of the Fluorine-related structure in various charge states in  $\text{SiO}_2$ . The energy of the neutral defect is taken as the reference (dotted line). 4H-SiC bandgap exists in between the vertical lines. No CTL is seen within the 4H-SiC bandgap, indicating the effectiveness of Fluorine passivation in improving device reliability.

The DFT-based formation energy analysis of the passivated structure (Figure 4.16(a)) indicated no Fluorine-related CTL in the 4H-SiC band gap (Figure 4.16(b)).

Thus, I conclude that Fluorine implantation in 4H-SiC MOSFETs could result in substantial mitigation of  $V_{th}$  instability and enhancement of reliability. However, the effect of reduced dielectric constant of F-doped SiO<sub>2</sub>, reported previously for Si/SiO<sub>2</sub> system [111], on 4H-SiC device performance needs further investigations.

#### 4.4 Chapter Summary

In this chapter, I investigated the electrical and structural properties of single carbon interstitial defects in the near-interfacial oxide region of 4H-SiC MOSFETs. Energetically and kinetically, the carbon interstitials prefer to be in the carboxyl configuration. This configuration could act as border hole traps, and are stable in their +2 charge state. They introduce switching oxide hole trap energy levels in the 4H-SiC bandgap, and can potentially contribute to threshold voltage instability in 4H-SiC MOSFETs.

The structural transformations of the carboxyl defect during hole capture was studied. The atomic relaxations involved puckering and back-bonding of positively charged Si atoms – similar to the behavior of oxygen vacancy hole traps. Additionally, the bond-order increase between carbon and oxygen atoms of the defect during double hole capture serves to stabilize the defect. The observed structural and bonding transformations also explain the absence of electron spin resonance (ESR) signal for this defect in SiO<sub>2</sub> grown on 4H-SiC.

The impact of NO, H<sub>2</sub> and Fluorine treatment on the reliability-limiting defects (carboxyl and oxygen vacancy) in 4H-SiC power MOSFETs were studied. NO treatment was seen to eliminate the carboxyl defects through the formation of isocyanates (NCO) and subsequent reactions. However, NO could be trapped in

oxygen vacancies, leading to configurations that could introduce additional  $V_{th}$  instability. Additionally, Nitrogen incorporation in the near-interfacial oxide region could also introduce switching oxide traps.

H<sub>2</sub> passivation is likely to have no or minimal effect on threshold voltage instability. This is because the H<sub>2</sub> treated carboxyl defect, by themselves, act as hole traps. The stability-providing structural transformations in H<sub>2</sub> treated carboxyl hole traps were deduced to be similar to that of original carboxyl defects.

Fluorine passivation was determined to be very effective in eliminating both carboxyl- and oxygen vacancy-related hole traps. The resulting atomic configuration was not observed to introduce further  $V_{th}$  instability. Thus, this chapter suggests Fluorine treatment as an effective method to improve reliability in future 4H-SiC power MOSFETs.

## Chapter 5: Integrated Modeling of Performance-limiting Defects in 4H-SiC Power MOSFETs

### 5.1 Background and Motivation

The identification of defects responsible for high  $D_{it}$  at 4H-SiC/SiO<sub>2</sub> system has been a topic of intensive experimental and theoretical research in the past, as described in Chapter 1. While their atomic nature still remains elusive, certain passivation techniques have been found to reduce their densities. These include post-oxidation annealing in nitric oxide [45, 46] and POC<sub>l</sub><sub>3</sub> [48]. Growing SiO<sub>2</sub> on alternative faces of 4H-SiC has also been found to affect the density of interface traps differently. For example, phosphorous passivation of the interface between oxide and (11 $\bar{2}$ 0) face of 4H-SiC was shown to result in significant mobility improvement [46]. Under these circumstances, the quantification of these defects - an aspect which has received limited attention - assumes significance. Nevertheless, mathematical modeling, and CC-DLTS and C-V measurements were recently used to enumerate specific traps at the interface [112].

While techniques like DFT can examine the atomic make-up of individual defects in a supercell of 4H-SiC/SiO<sub>2</sub> interface, computational limitations prohibit them from simulating and determining defect densities in an actual device. However, two-dimensional drift-diffusion simulations of a device, described in Chapter 2, can throw light on the total number of occupied trap densities at the interface based on an appropriate model for interface trap density and its occupation probability. These details are calculated after calibrating the device simulations to the experimentally-

determined terminal characteristics (current-voltage) of an actual MOSFET. Models used in the simulator for various scattering mechanisms were validated through previous research [49, 50, 51, 52]. While the simulator presents the ‘larger picture’ by enumerating the total density of occupied traps, it is inadequate to predict their atomic structure, energy levels and individual densities.

In general, while DFT calculations tend to identify qualitatively the atomic makeup of interface traps and their energy levels, 2D-device simulations tend to quantify these traps. However, simultaneous determination of the atomic make-up of individual traps and their quantification has typically not been achieved.

In this chapter, I propose a methodology that unifies Drift-Diffusion simulations and Density functional calculations to identify and quantify mobility-reducing interface defects in 4H-SiC power MOSFETs. The algorithm developed here uses various inputs from 2D-device simulations and density functional simulations, and provides the following details – a) the number of distinct type of traps close to the 4H-SiC conduction band, b) their energy levels, c) their atomic make-up, and c) their concentrations. An important application of this study should be in the development of effective defect passivation schemes and understanding their effects on the density of specific defects. This is in line with one of the goals of my Ph.D. research – performance enhancement of 4H-SiC MOSFETs through channel mobility improvements.

## 5.2 Methodology for Defect Identification and Quantification

The overall methodology used for the identification and quantification of mobility-reducing defects is given in Figure 5.1. While the flowchart is described in

relation to acceptor-type traps in the upper half of the bandgap, the same procedure can be applied to donor traps as well. I give detailed description of the methodology in the following sections.

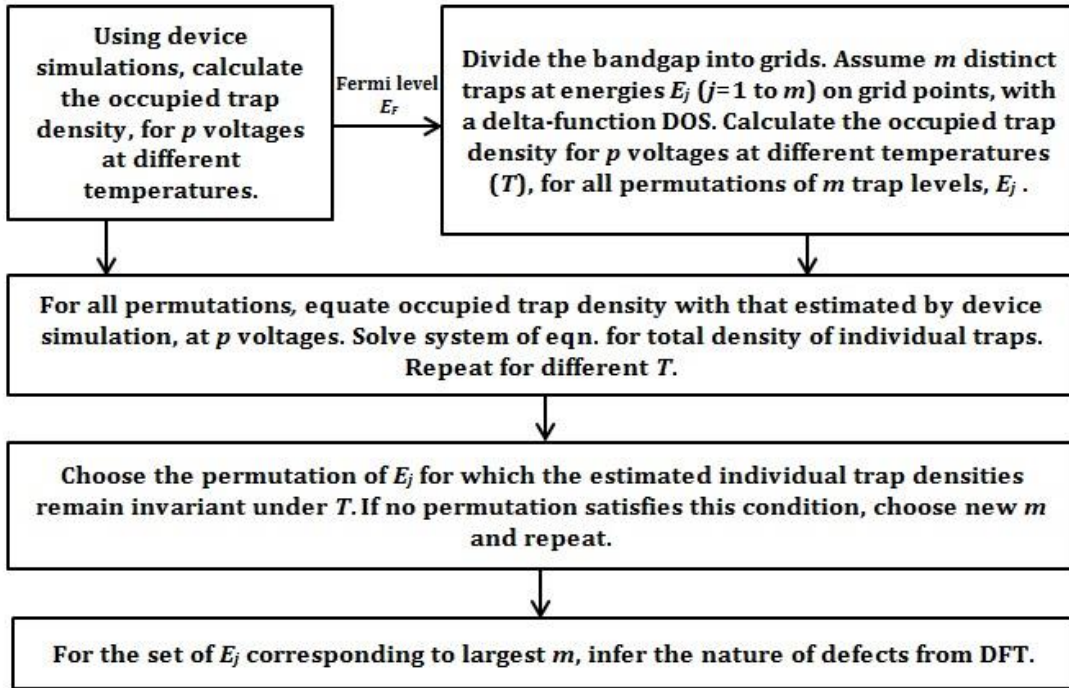


Figure 5.1: Methodology for the identification and quantification of mobility-reducing traps in 4H-SiC/SiO<sub>2</sub> interface.

### 5.2.1 2D-device Simulations and Experimental Verification

Firstly, the terminal current-voltage characteristics of a 4H-SiC power MOSFET are simulated for various temperatures by solving the semiconductor equations self-consistently. In order to calibrate the solver, we obtain agreement between the simulated curves and the experimentally measured I-V characteristics. An overview of the device solver has been provided in Section 2.1.

The nature of interface traps in the device simulator is described based on the conventional model where traps above and below the midgap are taken to be acceptors and donors, respectively. In the case of an n-type power MOSFET, the acceptor-type interface trap density ( $D_{it\_DS}$ ) is modeled as an exponential to resemble the upper half of experimentally-determined  $D_{it}$  spectrum. This model is given as

$$D_{it\_DS}(E_t) = D_{it\_mid} + D_{it\_edge} \exp\left(\frac{E_t - E_c}{\sigma_{it}}\right) \quad (5.1)$$

where  $E_c$  and  $E_t$  are the conduction band edge and trap energy, respectively and other terms are derived parameters. These parameters are restricted to take values which make  $D_{it\_DS}$  agree with experiments [29, 113]. The subscript in  $D_{it\_DS}$  indicates interface trap density as calculated with the device simulator (DS). The total number of occupied acceptor traps,  $N_{tot\_DS}$ , is calculated at a given gate bias and temperature as

$$N_{tot\_DS}(V_{GS}, T) = \int_{E_{mid}}^{E_c} D_{it\_DS}(E_t) f(E_t, E_F(V_{GS}), T) dE_t \quad (5.2)$$

Here,  $E_{mid}$  is the midgap level (=1.63 eV) and  $f(E_t)$  is the single-electron occupation probability of the trap at energy level  $E_t$  and is given as

$$f(E_t, E_F(V_{GS}), T) = \frac{1}{1 + \frac{1}{2} \exp\left(\frac{E_t - E_F}{k_b T}\right)} \quad (5.3)$$

where  $E_F$  is the Fermi level,  $k_b$  is the Boltzmann constant and  $T$  is the temperature.

The Fermi level is given as

$$E_F = E_c - k_b T \ln\left(\frac{N_c}{n}\right) \quad (5.4)$$

where  $N_c$  is the effective density of states at the CBE and  $n$  is the interface free electron concentration as determined by self-consistent solution to the semiconductor equations.

### 5.2.2 Algorithm for the Identification and Quantification of Traps

In this section, I present the methodology for an elimination-type search of the number of separate acceptor trap types and their energy levels, and for estimating their concentrations at the interface (Figure 5.1). The steps given below explain this algorithm more elaborately.

1. The total occupied acceptor trap density is calculated for a specific set of gate-source voltages at a specific temperature using the well-calibrated device simulator.
2. The energy space in the upper half of the 4H-SiC bandgap is discretized into small increments ( $dE$ ).
3. A specific number of distinct acceptor trap type is assumed and denoted  $m$ .
4. For a given  $m$ , all possible permutations of trap energy levels that fall on the grid points are considered. Thus, for  $n$  number of energy grid points, we have  $\frac{n!}{(n-m)! m!}$  number of sets, forming the sample space for the elimination-type search.
5. For each permutation, a delta-function Density of States is assigned for  $m$  traps. The heights of the delta functions correspond to individual trap concentration. I use the Fermi level calculated by the 2D-device simulator to determine the total number of occupied traps in terms of unknown delta function heights.

6. The occupied trap densities obtained in Step 1 and Step 5 are equated at different gate bias to obtain a system of linear equations. The total density of individual traps (heights of DOS) that might exist for each of  $m$  energy levels in a particular permutation is determined by optimally solving the system. Thus, corresponding to each set in step 4, we obtain a set of  $m$  individual trap densities.
7. Now, in order to choose the set representing the most realistic traps from the sample space, steps 5 and 6 are repeated at several different temperatures. I then select the permutation whose calculated total trap concentrations remain invariant (within a small percentage) with temperature, for a given  $m$ .
8. The value of  $m$  is incremented and steps 4 through 6 are repeated.
9. The maximum  $m$  that satisfies the condition in step 7 is selected as the possible number of distinct trap types in the device.

The details of the implementation of algorithm are given in the rest of this section. Firstly, the upper half of the bandgap is divided into  $n$  closely spaced grid points. A set of  $m$  distinct acceptor trap types with energies falling on the grid points is assumed. Thus, for an assumed  $m$ , we obtain a sample space of size  $\frac{n!}{(n-m)! m!}$ . The following procedure is employed to select the most realistic set representing the traps in the device.

In the algorithm, we denote the total DOS of traps ( $D_{it\_alg}$ ) in the bandgap as a sum of delta-functions whose coefficients corresponds to individual trap concentrations. Mathematically,

$$D_{it\_alg}(E_t) = \sum_{j=1}^m N_j \delta(E_t - E_j) \quad (5.5)$$

where  $E_j$  is the energy level of each trap and  $N_j$  is its concentration. For a given gate bias  $V_{GS}$  and temperature  $T$ , the number of occupied acceptor traps ( $N_{tot\_alg}$ ) for the DOS in equation (5.5) would be

$$\begin{aligned} N_{tot\_alg}(V_{GS}, T) &= \int_{E_{mid}}^{E_c} \sum_{j=1}^m N_j \delta(E_t - E_j) f(E_t, E_F(V_{GS}), T) dE_t \\ &= \sum_{j=1}^m N_j f(E_j, E_F(V_{GS}), T) \end{aligned} \quad (5.6)$$

where  $f$  is the probability function calculated by 2D-device simulations (equation (5.3)).

In order to solve for the unknown individual trap concentrations,  $N_j$ , in the above equation, I exploit the dependence of Fermi level and occupied trap concentrations on applied gate bias. Equation (5.2) is evaluated through device simulations and equated to equation (5.6) for a given temperature at  $p$  different gate voltages, where  $p > m$ . That is,

$$N_{tot\_alg}(V_{GS}, T) = N_{tot\_DS}(V_{GS}, T) \quad (5.7)$$

The resulting over-determined system of linear equations is solved to estimate  $N_j$  using the method of least-squares. The constraints on the solution are

$$\begin{aligned} \sum_{j=1}^m N_j &= \int_{E_{mid}}^{E_c} D_{it\_DS} dE_t \\ N_j &> 0 \end{aligned} \quad (5.8)$$

To elucidate the algorithm further, I provide a matrix representation of the system of  $p$  equations corresponding to  $p$  gate-source voltages and  $m$  trap levels as

$$[f]_{p \times m} [N]_{m \times 1} = [N_{tot\_DS}]_{p \times 1} \quad (5.9)$$

where  $[f]$ ,  $[N]$  and  $[N_{tot\_DS}]$  are the matrices representing the occupation probabilities, the unknown individual trap density and the number of occupied acceptor traps, respectively. The sizes of matrices, given as subscripts, show that the system of equations is over-determined. Since these equations are unlikely to have a unique solution, I adopt the method of least-squares for solving them. This is done by turning the over-determined system into a normal system of equations by multiplying both sides with the transpose of  $[f]$ .

$$[f]_{m \times p}^T [f]_{p \times m} [N]_{m \times 1} = [f]_{m \times p}^T [N_{tot\_DS}]_{p \times 1} \quad (5.10)$$

where  $[f]^T$  is the transpose of  $[f]$ . Subsequently, Gaussian elimination is used to solve for the individual trap concentrations. That is,

$$[N]_{m \times 1} = ([f]_{m \times p}^T [f]_{p \times m})^{-1} [f]_{m \times p}^T [N_{tot\_DS}]_{p \times 1} \quad (5.11)$$

This procedure is repeated for all the sets of  $m$  trap levels in the sample space. In order to choose the most likely set of trap levels, I exploit the dependence of Fermi level and occupied trap concentration on temperature. The trap selection criterion is detailed below.

The afore-mentioned algorithm for calculating the individual trap concentration is repeated for all permutations of  $m$  trap energy levels at various temperatures. *I argue that, for the most likely or realistic set of  $m$  traps at energies  $E_j$  ( $j=1$  to  $m$ ) in the sample space, the estimated individual trap concentrations ( $N_j$ ) would remain within a small percentage error at different temperatures.* If such a set was found to be non-existent in the entire sample space, a new number for distinct trap types ( $m$ ) is chosen for repeating the algorithm. In short, I argue that the most realistic or likely traps are represented by the largest set (largest  $m$ ) of trap energy levels that satisfies the above

temperature invariance of estimated densities. These trap levels are then compared with first-principle simulations to identify the atomic make-up of defects. A reasonable assumption that no new trap states are generated for the temperatures under consideration is made.

### 5.2.3 Density Functional Theory Simulations

The atomic configuration of defects, whose trap levels are determined using the methodology described in Section 5.2.2, are deciphered through DFT study of possible defects. The DFT simulation setup used for studying various near-interfacial defects in the 4H-SiC side of the interface is outlined in Section 2.6. Here, the trap energy levels are interpreted through its charge transition levels (CTL).

As mentioned in Section 3.2.1, CTL is defined as the electron chemical potential at which the formation energies of defects in two different charge states are equal. This is calculated by solving the formation energy equations (equation (3.2)) for the defect in two different charge states,  $q$  and  $q'$ . I designate the energy of this transition level as  $CTL(q/q')$ .

$$CTL(q/q') = \frac{E_{tot,q} - E_{tot,q'}}{q' - q} + \frac{E_{corr,q} - E_{corr,q'}}{q' - q} - \delta V - E_v \quad (5.12)$$

where  $E_{tot,q}$  and  $E_{tot,q'}$  are the total energies of the supercells with defects  $q$  and  $q'$  respectively.  $E_v$  is the valence band edge of the bulk 4H-SiC.  $\delta V$  is a correction factor added to the total energy of the defect system, which is calculated as the potential difference required for aligning the potential far from neutral defect to that of defect-free bulk [88].  $E_{corr,q}$  is a correction factor added to compensate for spurious electrostatic interactions between the charged defect and the background charges

introduced to prevent divergence of DFT simulations. Here, I have adopted a methodology that uses the monopole term of the correction, as suggested by Makov and Payne [89].

In this chapter, I also account for the influence of interface on the CTL through simple classical electrostatics, as in Ref. [37]. The potential energy of the dipole created by a charged defect in 4H-SiC and its image charge in the oxide is estimated classically using an effective dielectric constant. The extra energy due to this interface-specific polarization is then taken into account in the calculated trap level.

CTLs are picked up as trap levels in experiments like Deep-Level Transient Spectroscopy (DLTS) [114]. CTLs are different from optical transition levels observed in absorption or photoluminescence experiments, where atomic relaxations are not included.

### 5.3 Simulation Results

In this section, I describe the results derived for each of components in the integrated modeling approach described above. I begin with the 2D-device simulations of the 4H-SiC MOSFET.

#### 5.3.1 2-D Device Simulation Results

The  $I_D$ - $V_D$  and  $I_D$ - $V_G$  characteristics of an n-type 4H-SiC power MOSFET (fabricated on the Si-face of 4H-SiC and annealed in nitric oxide) were simulated at different temperatures. They are respectively shown in figures 5.2 and 5.3. Agreement between the simulated and the experimental I-V characteristics at each temperature (Figures 5.2 and 5.3) validates the models used in this work. The

parameters used in the  $D_{it}$  spectrum of equation (5.1) were extracted, and are provided in Table 5.1.

Table 5.1: Extracted parameters for modeling the density of interface traps ( $D_{it}$ ) in equation (5.1).

Trap density Parameters	Value
$D_{it\_edge}$ ( $\text{eV}^{-1}\text{cm}^{-2}$ )	$1.78 \times 10^{13}$
$D_{it\_mid}$ ( $\text{eV}^{-1}\text{cm}^{-2}$ )	$1.35 \times 10^{11}$
$\sigma$ (eV)	$8.90 \times 10^{-2}$

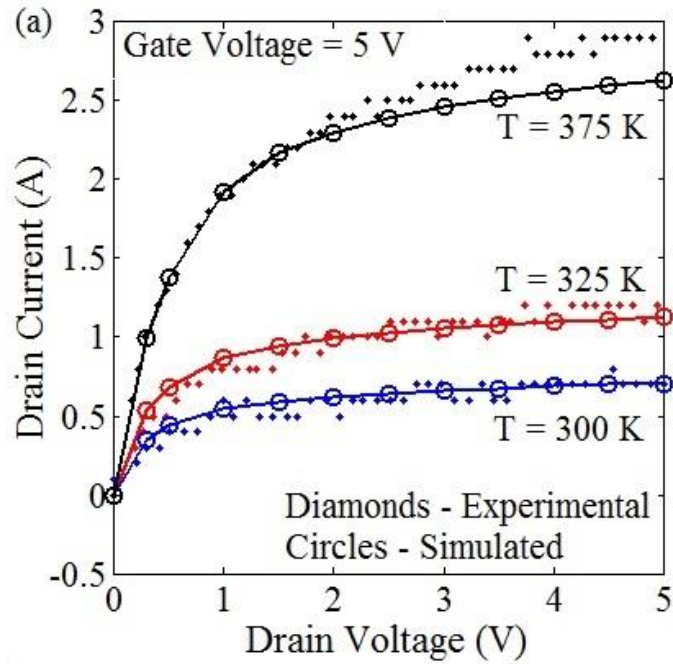


Figure 5.2: Experimental and simulated  $I_D$ - $V_D$  characteristics of 4H-SiC power MOSFET for different temperatures. Measurements were done at the U.S. Army Research Lab, Adelphi, MD.

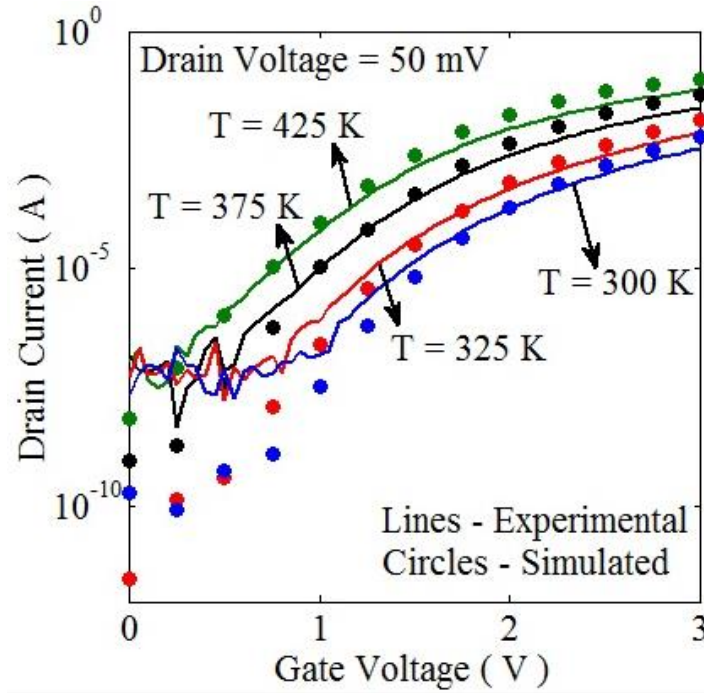


Figure 5.3: Experimental and simulated  $I_D$ - $V_G$  characteristics of 4H-SiC power MOSFET for different temperatures. Measurements were done at the U.S. Army Research Lab, Adelphi, MD.

After establishing the parameters in the device simulator by matching to experiment (Figure 5.2 and 5.3), I performed defect-specific device simulations performed at very low  $V_{DS}$  of  $5\mu\text{V}$ . This maintains a near-constant Fermi level along the channel and sets near-equilibrium conditions for the application of algorithm. At the same time, the choice of drain voltage for simulations should ensure that the data generated is not corrupted by numerical noise.

In Figure 5.4, I show the variation of Fermi level at the midpoint of the channel with applied gate bias and temperatures in the low- $V_G$  regime. The position of the Fermi energy is near the conduction band edge even at very low gate bias due to the high work function difference between 4H-SiC and the gate. Subsequently, the

concentration of occupied acceptor traps was determined at different gate voltages and temperatures using equations (5.2) and (5.3). This is depicted in Figure 5.5.

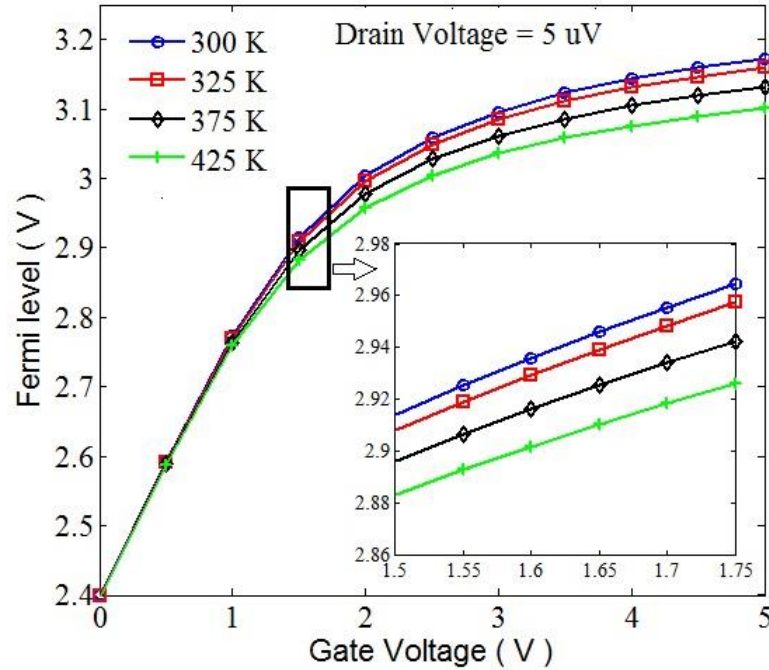


Figure 5.4: Fermi level position as a function of gate bias at different temperatures as calculated by 2D-device simulations. The voltage regime where the algorithm is applied is shown in the inset.

It should be noted that the occupied trap density increases with temperature at low gate voltages. This trend is seen to reverse for higher voltages, which is in keeping with previous research [115]. I explain this behavior in the light of two distinct effects that temperature has on the occupancy probability function,  $f(E_b, E_F, T)$ . It is well-known that the Fermi function broadens with increasing temperature. Simultaneously, the Fermi level and the Fermi function shift towards the intrinsic energy level in the bandgap. At low gate voltages, the temperature dependence of occupied trap

concentration is mainly influenced by the broadening of the probability function than the shift in Fermi level. This is evident from Figure 5.4, which shows closely spaced Fermi levels in the low-voltage regime for various temperatures. However, at higher voltages, the Fermi levels were seen to be widely spaced for different temperatures. In this case, the shifting effect of the occupancy probability function dominates its broadening effect, resulting in a decreased occupied trap density with temperature.

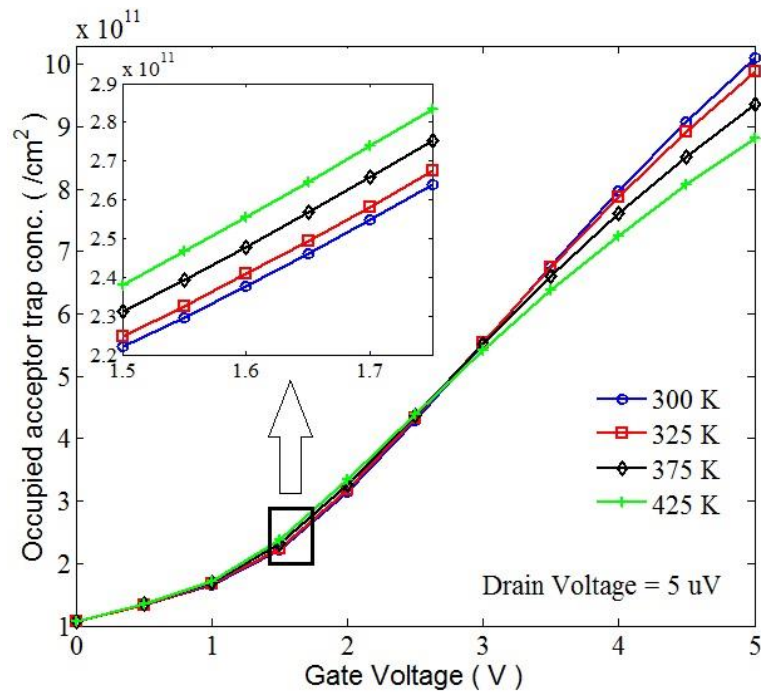


Figure 5.5: Occupied trap concentration at different gate voltages and temperatures as calculated by 2D-device simulations. The voltage regime where the algorithm is applied is shown in the inset.

### 5.3.2 Results from the Algorithm

In order to identify and quantify mobility-reducing defects in a 4H-SiC MOS system, I applied the algorithm described in Section 5.2.2. The unknown quantities in the algorithm include the number of distinct acceptor trap types ( $m$ ), the location of each of the trap energy in the bandgap ( $E_j$ ) and their respective concentrations ( $N_j$ ). The inputs from device simulations into the algorithm included the calculated Fermi levels and total occupied trap concentrations for a set of low gate voltages at various temperatures, as in the inset of Figures 5.4 and 5.5. A very low gate voltage regime was chosen for the algorithm as significant variation of trap filling occurs in this range.

The upper half of the bandgap (1.6 - 3.2 eV) was divided into grid points, spaced 0.05 eV apart. The algorithm was designed to test for up to five distinct trap types ( $m=1$  to 5). For each  $m$ , all possible permutations of trap energy values on the grid points were examined for being realistic traps. In order to calculate the respective concentrations of the  $m$  traps,  $N_j$  ( $j=1$  to  $m$ ), in a given permutation, we formed and optimally solved the over-determined system of linear equations, given in equation (5.9). Equations in the system were formed at different gate voltages varying from 1.5 V to 1.75 V in steps of 50 mV ( $p=6$ ,  $p>m$ ). The choice of this voltage range leads to sufficient variation in Fermi level (Figure 5.4 inset) and occupancy probabilities with gate bias, preventing the system from having infinite solutions and minimizing numerical noise.

The algorithm was repeated for temperatures 300 K, 325 K, 375 K and 425 K. Based on the trap selection criterion described in Section 5.2.2, we report the

existence of three ( $m=3$ ) distinct trap types, their energy levels and densities at two locations in the power MOSFET channel. The detailed results are tabulated in Table 5.2. For both the channel locations, the variation in calculated trap density,  $N_j$ , with respect to temperature for this specific combination of  $m$  and  $E_j$  was found to be less than 20%. For  $m > 3$ , all permutations of  $E_j$  ( $j=1$  to  $m$ ) were found to give significantly higher variation in calculated trap density with temperature and hence, were rejected.

Table 5.2: Trap energy levels and their concentrations extracted using the algorithm for two locations in the channel.

Distance into channel from source ( $\mu\text{m}$ )	Trap 1		Trap 2		Trap 3	
	Energy (eV)	Conc. ( $10^{11}/\text{cm}^2$ )	Energy (eV)	Conc. ( $10^{11}/\text{cm}^2$ )	Energy (eV)	Conc. ( $10^{12}/\text{cm}^2$ )
0.34	2.80	2.24	3.05	5.85	3.10	0.99
0.42	2.85	2.45	3.05	4.99	3.20	1.06

### 5.3.3 Density Functional Simulation Results

In order to identify the atomic nature of defects causing the trap levels given in Table 5.2, I investigated various near-interfacial defects in the 4H-SiC side of the interface by performing DFT simulations on a 72-atom bulk 4H-SiC. Specifically, I investigated Si vacancy and Carbon di-interstitial defect for being possible contributors to high  $D_{it}$  near the conduction band edge following suggestions from recent DFT simulations and experiments [32, 36, 41, 43].

**Silicon vacancies:** Recent spin-dependent recombination (SDR) experiments suggested the presence of Silicon vacancies as a major cause of electron trapping in 4H-SiC MOSFETs [32, 33]. Silicon vacancies occurring at two non-equivalent lattice sites of 4H-SiC crystal - hexagonal (*h*-centre) and cubic (*k*-centre) - were investigated using DFT. The charge states of -2, -1, 0, +1 and +2 were considered for each of the defects. Geometric optimization was performed on each of the defect structures until the maximum force acting on an atom was less than  $\sim 0.05$  eV/Å. The structurally optimized defect configurations for Si vacancy at *k*- and *h*- center are depicted using XCrySDen [116] in Figures 5.6 (a) and 5.6 (b), respectively.

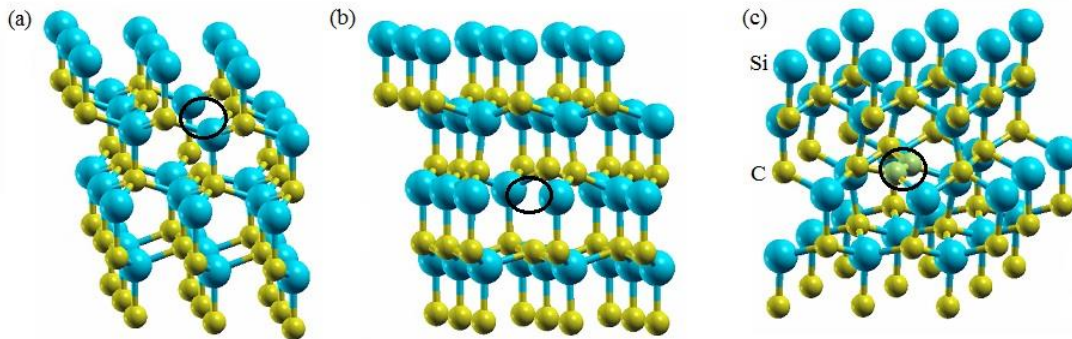


Figure 5.6: (a) Silicon vacancy at cubic site (*k*-center), (b) Silicon vacancy at hexagonal site (*h*-center) and (c) Carbon di-interstitial defect. The defects are circled and are in their neutral states. Larger spheres represent Silicon and smaller spheres represent Carbon.

I carried out DFT simulations using the simulation setup described in Section 2.6.  $\delta V$  in equation (5.12) was determined to be  $\sim -0.17$  eV and  $-0.28$  eV for Si vacancy at *h*- and *k*- center, respectively. The Makov-Payne electrostatic correction factors,

$E_{corr,q}$ , were calculated as 0.23 eV and 0.92 eV for  $|q|=1$  and 2, respectively. The additional energy due to polarization at the interface was calculated as 0.05 eV and 0.2 eV for charge states  $|q|=1$  and 2, respectively. Here, the defects were located at a distance of  $3\text{\AA}$  from the interface. Subsequently, using equation (5.12), the trap levels were determined, and are shown in Figure 5.7. The trap levels due to Si vacancies were seen to be near the midgap and valence band edge. Therefore, they are unlikely to be a major reason for high  $D_{it}$  near the conduction band edge. The results were seen to be reasonably similar to that of Ref. [43] despite the fact that Ref. [43] dealt with Si vacancies in bulk 4H-SiC, while our calculations focused on vacancies close to the interface as in a 4H-SiC MOSFET.

**Carbon di-interstitials:** The emission of Carbon atoms into SiC from the interface during oxidation has been studied previously [44]. Two interstitial C atoms have been shown to combine to form an immobile and stable C di-interstitial without a kinetic barrier [42]. Therefore, we followed earlier work [36] and examined this defect in bulk 4H-SiC in three different charge states – neutral, -1 and -2. For continuity of presentation, we describe it below.

The simulation environment used was the same as in the study of Si vacancies. The geometrically optimized structure for the C di-interstitial defect in its neutral state is shown in Figure 5.6 (c). An enlarged picture of the defect is also shown in Figure 5.8. Each of the C atoms in the defect can be seen to be bonded to a Si and C in the lattice. The Makov-Payne and electrostatic correction factors were the same as that of Si vacancies.  $\delta V$  was found to be  $\sim 0.11$  eV. The charge transition levels,  $CTL(0/-1)$  and  $CTL(-1/-2)$ , were determined to be at 3.36 eV and 3.27 eV,

respectively as shown in Figure 5.7. Being close to the conduction band edge (3.25 eV), these energy levels point to C di-interstitial in SiC side of the interface as a possible candidate for high  $D_{it}$ .

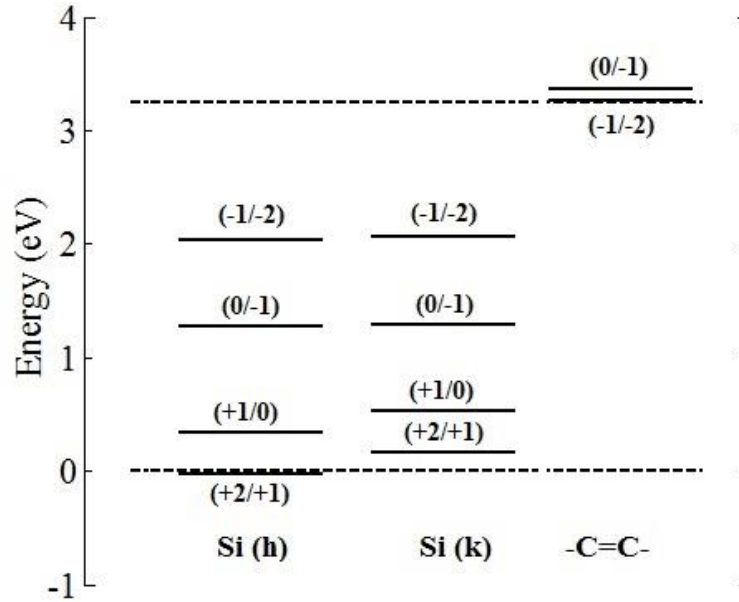


Figure 5.7: Positions of thermodynamic charge transition levels of defects in the bandgap of 4H-SiC/SiO<sub>2</sub> interface. The valence band maximum and conduction band minimum are shown as dotted lines. Si vacancy at *h*- and *k*- centers in charge states of +2, +1, 0, -1 and -2 were examined. Similarly, C di-interstitial in 0, -1 and -2 charge states were studied.

In summary, our DFT simulations of C di-interstitial defect suggested traps near the conduction band edge (CBE). Thus, we attribute the near-CBE trap level at 3.1-3.2 eV, extracted from the algorithm, in Table 5.2 to Carbon di-interstitial defect. The density of this defect at the interface is estimated as  $\sim 1 \times 10^{12}/\text{cm}^2$ . However, the

nature of traps located at 2.8-2.85 eV and 3.05 eV still remains elusive based on our DFT results. Further *ab-initio* simulations are required to determine the atomic make-up of these traps. However, we have quantified these traps using the methodology proposed above. Additionally, our DFT simulations indicate that Si vacancies (both at *h*- and *k*-centers) are probably not major contributors to high  $D_{it}$ .

#### 5.4 Comparison with Experiments

Based on the results given in Table 5.2, we find that three distinct peaks are likely to occur in the  $D_{it}$  spectrum near the 4H-SiC CBE. Two of the peaks are clearly distinguishable in the near-CBE  $D_{it}$  spectrum extracted using Gray-Brown C-V technique [113]. However, this work did not address the spread in these peaks.

Additionally, our results tend to agree with the recent results of Basile *et al.* where three different types of traps were distinguished in 4H-SiC/SiO<sub>2</sub> system [31], supporting the validity of the proposed algorithm. Their findings, based on emission and capture behavior of traps obtained by energy-resolved CCDLTS, indicated trap levels that are a) shallower than 0.1 eV below CBE (3.25 eV), b) centered at 0.15 eV below CBE, and c) centered at 0.4 eV below CBE. These levels compare well with our results of Table 5.2. While they attributed the trap levels at 0.4 eV and 0.15 eV below the 4H-SiC CBE to the defects in oxide, the  $E_c - 0.1\text{eV}$  was interpreted to be due to Carbon di-interstitial in the SiC side of the interface. This is corroborated by our DFT simulations on C di-interstitial defect, which indicate trap levels near the conduction band edge (Figure 5.7). Additionally, previous *ab-initio* calculations also have suggested C di-interstitial as a major defect causing poor channel mobility [41, 42]. The carbon di-interstitial defect is pictured in Figure 5.8.

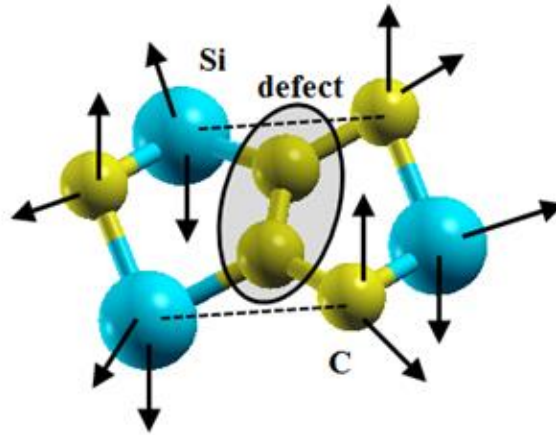


Figure 5.8: Pictorial representation of carbon di-interstitial defect. The arrows represent bonds. The dotted lines show the ideal bonding in the absence of the defect.

Another aspect of this work has been the quantification of traps at each energy level. Previously, Basile *et al.* suggested and quantified C di-interstitial defect in 4H-SiC MOS capacitors by modeling its spatial distribution and high-frequency C-V characteristics to fit the results of CCDLTS and C-V measurements [112]. They determined two distributions of C di-interstitials – a) a density of  $6.6 \times 10^{11}/\text{cm}^2$  spread within 2nm from interface, and b) a density of  $1 \times 10^{11}/\text{cm}^2$  distributed over 50nm from the interface. My algorithm calculated the number density of this defect to be  $\sim 1 \times 10^{12}/\text{cm}^2$ . This is higher than the total density determined by Basile *et al.* [112]. I ascribe this difference to the fact that we investigated a power MOSFET which was probably subjected to different conditions during processes like Nitrogen passivation. N passivation has been reported to decrease the total density of traps at 4H-SiC/SiO<sub>2</sub> interface. [45]. I have quantified the traps existing at other energy levels in the bandgap as well.

My ab-initio simulations on Si vacancies at both the non-equivalent sites in 4H-SiC side of the interface do not suggest them to be a major mobility-degrading defect. They are seen to create trap levels in the lower half of the bandgap as in Figure 5.7. Similarly, previous density functional investigations on Si vacancies in 4H-SiC bulk suggested their trap states to be near midgap and near valence band edge [43]. However, recent experiments based on spin dependent recombination spectroscopy have identified Si vacancy as an important defect in 4H-SiC MOSFETs [32, 33].

## 5.5 Additional Comments on the Methodology

The algorithm described in this paper is particularly useful to explore the trap states near the conduction band edge (CBE) of 4H-SiC/SiO<sub>2</sub>. Mobility-degrading defects, which are of utmost concern, are known to be dominant in this region as indicated by the U-shaped  $D_{it}$  spectrum. Owing to the large work-function difference between 4H-SiC and SiO<sub>2</sub>, the Fermi level remains close to the CBE even at zero gate bias. Therefore, by applying judiciously chosen gate voltages, the occupancy of trap levels near the conduction band edge can be modulated significantly – an idea which is at the core of the algorithm. By the same argument, the methodology would not be able to resolve trap states that exist between midgap and ~2.7 eV. This is because the traps in this region are always fully occupied. As a result, equation (5.9) will have either (a) infinite solutions, or (b) identical solutions for all the trap levels in this energy range. In either case, the algorithm would fail to resolve the trap levels since they exist far away from the Fermi level.

Previous experiments aimed at identification and quantification of interface traps were performed on MOS capacitors [112]. It should be noted that experiments like C-

V measurements are complicated on a power MOSFET due to the presence of additional parasitic capacitances. In this work, we overcame this limitation and identified and quantified traps directly in a 4H-SiC power MOSFET.

## 5.6 Chapter Summary

In this Chapter, I proposed an algorithm for the identification and quantification of specific mobility-reducing defects at 4H-SiC/SiO<sub>2</sub> interface. The algorithm relies on 2D-device simulations and *ab-initio* calculations.

Firstly, I carried out device simulation of a 4H-SiC power MOSFET. Such simulations, when calibrated to experiments, provide the density of occupied interface traps inside the 4H-SiC power MOSFET. Subsequently, the algorithm performs a brute-force search of possible trap energy levels in the semiconductor bandgap. Using delta-function DOS for traps and their occupancy probabilities, the algorithm recalculates the number of filled traps. The occupied trap densities obtained from both the methods are equated under different gate bias conditions to form a system of equations. By solving this system, I estimated the concentration of individual interface defects. The temperature invariance of the calculated trap concentration forms the criterion for the identification of realistic trap levels in the bandgap.

However, the above approach is blind towards the atomic configuration of the defects corresponding to these trap levels. I overcame this limitation by DFT simulations of possible defects and comparing the DFT-based trap levels with those obtained by the algorithm.

My results indicated that the  $D_{it}$  spectrum near the 4H-SiC conduction band edge has contributions from three trap types located at 2.8-2.85 eV, 3.05 eV and 3.1-3.2

eV. I also calculated their densities. My DFT simulations point to C di-interstitial defect in the 4H-SiC side of the interface as a possible mobility-reducing trap. However, Si vacancies in 4H-SiC are unlikely to be a major mobility-limiting trap. Further work is required to validate the methodology presented in this chapter for more generic cases.

## Chapter 6: Conclusions, Summary, and Future Work

In this chapter, I summarize the major results and conclusions of my Ph.D. research. I will also discuss the possible future course of this work.

### 6.1 Summary of the Research and Major Conclusions

In this Ph.D. work, I have focused on two broad issues that have hindered 4H-Silicon Carbide power MOSFETs from realizing their full potential – their poor reliability (threshold voltage instability), and poor performance (very low channel mobility). I have also focused on the development of device processing strategies that could improve the reliability of future devices.

#### 6.1.1 General Approach

My objective has been to understand the root causes of these concerns at an atomic level, and then to identify suitable fabrication process modifications that could mitigate these mechanisms. Due to the ‘all-encompassing’ nature of the problem – which ranges from the physics of defects in 4H-SiC power MOSFETs to their experimental manifestations in a variety of experiments – I used a combination of theoretical modeling approaches in conjunction with experiments.

In this approach, I first used *ab-initio* or first-principles hybrid Density Functional Theory (DFT) and associated tools for modeling the electrical activity of defects in 4H-SiC MOSFETs at an atomic level. The electrical activity of defects was analyzed using their thermodynamic charge transition levels (CTL). Here, the defects are

concluded to be electrically active provided they gave rise to CTLs within the 4H-SiC bandgap.

Subsequently, I integrated first-principles hybrid DFT with conventional mathematical modeling techniques (like Drift-Diffusion simulations, and rate equation-based modeling) which rely on physics-based models of various physical mechanisms (In this context, I call them ‘*second-principles*’ calculations). This approach allowed me to analyze the effect of atomic-level defects on the ‘*macroscopic*’ properties related to 4H-SiC power MOSFETs (For example, threshold voltage instability, and I-V characteristics etc.). Additionally, the models, derived using this approach, were validated by comparing them with electrical measurements (performed by the researchers at the U.S. Army Research Lab, Adelphi, and those reported in literature).

### 6.1.2 Reliability of 4H-SiC Power MOSFETs

From the reliability perspective, the specific problem addressed in this work includes understanding the atomistic origins of High-Temperature Gate Bias (HTGB) stress-induced threshold voltage ( $V_{th}$ ) instability in 4H-SiC MOSFETs. Dramatic super-linear increase in  $V_{th}$  instability has been recently observed as a function of logarithm of applied stress duration. This is in clear contrast to the typical room temperature behavior, where the instability was seen to vary linearly with the logarithm of applied stress time. While the room-temperature instability is typically attributed to hole trapping and de-trapping by direct tunneling into oxygen vacancy border bole traps, the exact mechanisms behind the high-temperature effect are poorly understood.

I approached the problem by assuming time-dependent activation of additional oxygen-vacancy hole traps at high temperature and applied gate bias in 4H-SiC MOSFETs, based on evidences provided by electrical and Electron Spin Resonance experiments. My hybrid DFT modeling efforts revealed two types of oxygen vacancies in silicon dioxide. While the electrical activity of one of them indeed supported the observations on room-temperature  $V_{th}$  instability, the other type of vacancy was seen to lend itself for electrical activation under HTBG stressing, supporting the high-temperature behavior. I then modeled the transients of the activation process using Arrhenius rate equations (with inputs from hybrid DFT calculations), which was found to agree well with the experimentally determined time-dependence of  $V_{th}$  instability under HTGB stressing. Thus, I validated the HTGB-stress assisted oxygen-vacancy hole trap activation model using first-principles and ‘*second-principles*’ (rate equations) calculations along with electrical measurements.

This work also investigated additional atomic-level defects - particularly related to Carbon - that could potentially contribute to threshold voltage instability in 4H-SiC power MOSFETs. This is important because carbon emission into the oxide has been reported during 4H-SiC oxidation. In this regard, I investigated the electrical activity of a basic defect configuration – a single carbon interstitial. Thermodynamically, the carbon interstitial is most likely to exist in the carboxyl configuration (Si-[C=O]-Si). This configuration was seen to act as a double hole trap, that could potentially contribute to room-temperature  $V_{th}$  instability through hole trapping and de-trapping by direct tunneling in response to applied bias. Additionally, the structural

transformations in carboxyl defects during hole capture were seen to be very similar to that of oxygen defects. Thus, I proposed carbon interstitials to play an important role in the reliability degradation in 4H-SiC MOSFETs. However, they are unlikely to contribute to the excessive aggravation of  $V_{th}$  instability under HTGB stress.

### 6.1.3 Mitigation of Reliability-limiting Defects

Another area which has received attention in this research is the development of defect mitigation strategies for improving device reliability. The idea is to identify suitable fabrication process modifications which could eliminate the root causes of room temperature and high temperature threshold voltage degradation (in other words, oxygen vacancies and carboxyl defects). The approach here is to use DFT-based first principle molecular dynamics simulations to study the interactions between defects and various other molecules (called passivants). This technique allowed me to see if the defects are eliminated by the passivants during their chemical reaction. Additionally, it also reveals various reaction product complexes in the lattice, whose electrical activity and implications on device reliability could be studied using their CTLs.

In this direction, this work suggested Fluorine passivation to be very effective in eliminating carboxyl defects and oxygen vacancies, thereby mitigating room-temperature and high-temperature reliability degradation in 4H-SiC MOSFETs. Additionally, controlled Nitric Oxide treatment could effectively eliminate carboxyl defects. Another side-effect of Nitric oxide passivation that was found to be thermodynamically feasible includes Nitrogen incorporation at the interface – a process called counter-doping. This phenomenon aids in improving the effective

carrier mobility in 4H-SiC MOSFETs. However, passivants like molecular hydrogen was found to be ineffective in improving the reliability of devices.

#### 6.1.4 Performance of 4H-SiC Power MOSFETs

From the performance perspective, the specific problem addressed in this work includes the identification and quantification of mobility-limiting defects in 4H-SiC power MOSFETs. The effective mobility in the state-of-the-art 4H-SiC MOSFETs is seen to be very low, mainly due to high density of interface traps ( $D_{it}$ ) owing to the poor quality of 4H-SiC/SiO<sub>2</sub> interface. Thus, this aspect is important for devising suitable defect mitigation strategies for future high-performance devices.

In this work, I approached this aspect by integrating DFT with conventional Drift-Diffusion simulations. Firstly, I simulated the I-V characteristics of a sample 4H-SiC power MOSFET using accurate models for mobility and  $D_{it}$ . Subsequently, I developed an algorithm that resolves the  $D_{it}$  into its component trap levels. The algorithm resulted in the identification of, i) the number of distinct trap levels contributing to the  $D_{it}$ , ii) their trap levels, and iii) their individual concentrations. Following this, I used hybrid DFT to analyze the electrical activity of potential interface defects to identify the atomic composition of the traps revealed by the algorithm.

Using this methodology, I proposed the  $D_{it}$  spectrum to be composed of three distinct traps, and calculated their individual densities. Additionally, I identified Carbon-dimer defect, located in 4H-SiC side of the interface, to be the most important performance-limiting defect in 4H-SiC MOSFETs. However, Silicon vacancies in

4H-SiC are unlikely to contribute to the high density of mobility-limiting interface traps.

## 6.2 Future Work

Significant amount of research is currently being devoted towards improving 4H-SiC MOSFET reliability and performance. Here, I outline a few directions in which this work could be carried forward in future.

In my work, I have developed the oxygen vacancy hole trap activation model for explaining the high temperature reliability degradation in 4H-SiC MOSFETs. However, the electric field dependence of this model needs to be ascertained. This would aid in the development of compact models that could help us in designing reliable 4H-SiC MOSFETs in future.

Additionally, the methodologies outlined this dissertation can be applied to understand the root cause of some recently observed physical phenomena in devices. For example, the threshold voltage instability envelope in 4H-SiC power MOSFETs has been seen to drift in the positive direction during the HTGB stress sequences. This is a critical reliability degrading phenomenon, and is tentatively attributed to electron trapping in the oxide. The atomic nature of these electron traps, and the physical mechanisms governing electron trapping are still unknown. These mechanisms need to be explored by combining DFT simulations of various possible defects with conventional TCAD modeling, in conjunction with experimental data. Furthermore, based on the identification of the root cause defects and mechanisms, suitable mitigation strategies could be developed using the molecular dynamics method.

Research-grade 4H-SiC MOSFETs are currently being fabricated on alternate 4H-SiC faces like the Carbon-face (100% C at the surface) and the a-face (50% C and 50% Si). The atomic nature of defects produced on these faces is possibly different from those occurring in the MOSFETs grown on the traditional Si-face. Consequently, their passivation mechanisms are also expected to be different. In this context, the reliability- and performance-limiting mechanisms in the devices grown on alternate faces merit detailed investigation. This could be achieved by extending the approach outlined in this work.

4H-SiC MOSFETs with improved channel electron mobility have been achieved using passivation processes like Antimony treatment. While counter-doping, by which antimony is incorporated at the 4H-SiC surface as a dopant, is believed result in improved mobility, the exact mechanism is still under debate. Such effects and their implications on device performance could be investigated in greater detail using DFT simulations with Drift-Diffusion simulations.

Finally, the methodology provided in chapter 6 has revealed three distinct defects at 4H-SiC/SiO<sub>2</sub> interface on the Si-face of 4H-SiC. I have identified one of them a carbon dimer defect in 4H-SiC. However, the atomic nature of the other two defects needs to be deciphered. This could be done in future through DFT simulations of more possible defect structures. Similarly, other possible candidates for border hole trapping in the device need to be explored.

## References

- [1] C. M. Zetterling, *Process Technology for Silicon Carbide Devices*, EMIS Processing Series, no.2. INSPEC, IEE, UK (2002).
- [2] A. Agarwal and S. Haney, *J. Electron. Mater.* **37**, 646 (2008).
- [3] S. Potbhare, N.Goldsman, G.Pennington, A. Lelis and J.M. McGarrity, *J. Appl. Phys*, vol. 100, 044516, 2006.
- [4] A. J. Lelis, D. B. Habersat, R. Green, A. Ogunniyi, M. Gurfinkel, J. Suehle, and N. Goldsman, *IEEE Trans. Electron Devices*, vol. **55**, no. 8, pp. 1835–1840, Aug. 2008.
- [5] Z. Chbili, K. P. Cheung, P. Campbell, J. S. Suehle, D. E. Ioannou, S.-H. Ryu, and A. J. Lelis, *2013 IEEE International Integrated Reliability Workshop Final Report (IRW)* pp. 90-93, 13 - 17 Oct. 2013.
- [6] M. Gurfinkel *et al.*, *IEEE Trans. Electron Devices*, vol. **55**, no. 8, pp. 2004–2012, Aug. 2008.
- [7] X. Shen *et al.*, *Appl. Phys. Lett.* **98**, 063507 (2011).
- [8] M. J. Marinella *et. al.*, *Appl. Phys. Lett.* **90**, 253508 (2007).
- [9] A. J. Lelis, R. Green, D. B. Habersat, and M. El, *IEEE Trans. Electron Devices*, vol. **62**, no.2, pp. 316-323, Feb. 2015.
- [10] A. J. Lelis, D. B. Habersat, R. Green, and N. Goldsman, *Mater. Sci. Forum*, vols. 717–720, pp. 465–468, May 2012.

- [11] Y. Hijikata, H. Yaguchi, and S. Yoshida, *Applied Physics Express* **2**, 021203 (2009).
- [12] A. J. Lelis, and T. R. Oldham, *IEEE Trans. Nuclear Science*, vol. 41, no. 6, pp. 1835-1843, Dec. 1994.
- [13] J. F. Conley-Jr., P. M. Lenahan, A. J. Lelis, and T. R. Oldham, *Appl. Phys. Lett.* **67**, 2179 (1995).
- [14] J. T. Ryan, P. M. Lenahan, T. Grasser, and H. Enichlmair, *Appl. Phys. Lett.* **96**, 223509 (2010).
- [15] T. Grasser, B. Kaczer, W. Goes, Th. Aichinger, Ph. Hehenberger, M. Nelhiebel, *Microelectronic Engineering* **86**, pp. 1876–1882, 2009.
- [16] Z.-Y Lu, C. J. Nicklaw, D.M. Fleetwood, R. D. Schrimpf, and S.T. Pantelides, *Phys. Rev. Lett.*, vol. **89**, no. 28, pp. 285505-1 - 285505-4, Dec. 2002.
- [17] T. Uchino, and T. Yoko, *Phys. Rev. B* **74**, 125203 (2006).
- [18] P. E. Blochl, *Phys. Rev. B* vol. **62**, no. 10, pp. 6158-6179 (2000).
- [19] J. K. Rudra, and W. B. Fowler, *Phys. Rev. B* **35**, no. 15, pp. 8223 (1987).
- [20] A. C. Pineda, and S. P. Karna, *J. Phys. Chem. A*, vol. **104**, no. 20, pp. 4699-4703 (2000).
- [21] A. V. Kimmel, P. V. Sushko, A. L. Shluger, and G. Bersuker, *ECS Transactions*, **19 (2)** 3-17 (2009).
- [22] C. M. Carbonaro, V. Fiorentini, and F. Bernardini, *Phys. Rev. Lett.* vol. **86**, no. 14, pp. 3064-3067 (2001).

- [23] S. Wang et. al., *Phys. Rev. Lett.* **98**, 026101 (2007).
- [24] T. Zheleva, A. Lelis, G. Duscher, F. Liu, I. Levin, and M. Das, *Appl. Phys. Lett.* **93**, 022108 (2008).
- [25] T.L. Biggerstaff et al., *Appl. Phys. Lett.* **95**, 032108 (2009).
- [26] J.A. Taillon et al., *J. Appl. Phys* **113**, 044517 (2013).
- [27] J. Rozen et. al., *J. Appl. Phys.* 103, 124513 (2008).
- [28] J. Rozen, S. Dhar, M. E. Zvanut, J. R. Williams, and L. C. Feldman, *J. Appl. Phys.* **105**, 124506 (2009).
- [29] V.V. Afanas'ev, M. Bassler, G. Pensl and M. Schulz, *Phys. Stat. sol (a)*, vol. 162, pp. 321-337, 1997.
- [30] T.E.Rudenko, I.N. Osiyuk, I.P. Tyagulski, H.O. Olafsson and E.O. Sveinbjornsson, *Solid State Electron.* **49**, 545-553 (2005).
- [31] A.F. Basile, J. Rozen, J.R. Williams, L.C. Feldman and P.M.Mooney, *J. Appl. Phys.* **109**, 064514 (2011).
- [32] C.J. Cochrane, P.M. Lenehan, and A.J. Lelis, *Appl. Phys. Lett.* **100**, 023509 (2012).
- [33] M.S. Dautrich, P.M. Lenehan, and A.J. Lelis, *Appl. Phys. Lett.* **89**, 223502 (2006).
- [34] P. Deak, J.M. Knaup, T. Hornos, C. Thill, A. Gali, and T. Frauenheim, *J. Phys. D: Appl. Phys.*, vol. 40, pp. 6242-6253, 2007.
- [35] A. Gavrikov et al., *J. Appl. Phys.* **104**, 093508 (2008).

- [36] F. Devynck, A. Alkauskas, P. Broqvist and A. Pasquarello, *AIP Conf. Proc.* **1199**, pp. 108-109, 2010.
- [37] F. Devynck, A. Alkauskas, P. Broqvist, and A. Pasquarello, *Phys. Rev. B* **84**, 235320 (2011).
- [38] F. Devynck, A. Alkauskas, P. Broqvist, and A. Pasquarello, *Phys. Rev. B* **83**, 195319 (2011).
- [39] J. M. Knaup, P. Deak, Th. Frauenheim, A. Gali, Z. Hajnal, W. J. Choyke, *Phys. Rev. B* **72**, 115323 (2005).
- [40] S. Salemi, N. Goldsman, D.P. Ettisserry, A. Akturk, and A. Lelis, *J. Appl. Phys.* **113**, 053703 (2013).
- [41] X. Shen and S. T. Pantelides, *Appl. Phys. Lett.* **98**, 053507 (2011).
- [42] X. Shen, M.P. Oxley, Y. Puzyrev, B.R. Tuttle, G. Duscher, and S. T. Pantelides, *J. Appl. Phys.* **108**, 123705 (2010).
- [43] A. Zywietz, J. Furthmuller, and F. Bechstedt, *Phys. Rev. B* **59**, No. 23 (1999).
- [44] Y. Hijikata, H. Yaguchi, and S. Yoshida, *Materials Science Forum*, vol. 679-680, pp. 429-432, 2011.
- [45] G.Y. Chung *et al.*, *IEEE Electron Device Letters*, vol. 22, No. 4, pp. 176-178, 2001.
- [46] G. Liu, A.C. Ahyi, Y. Xu, T. Isaacs-Smith, Y.K. Sharma, J.R. Williams, L.C. Feldman, and S. Dhar, *IEEE Electron Device Letters*, vol. 34, No. 2, pp. 181-183, 2013.

- [47] A. Modic *et. al.*, *Electron Device Letters, IEEE* , vol.35, no.9, pp.894,896, Sept. 2014.
- [48] P. Fiorenza, F. Giannazzo, M. Vivona, A. La Magna, and F. Roccaforte, *Appl. Phys. Lett.* **103**, 153508 (2013).
- [49] S. Potbhare, N. Goldsman, A. Lelis, J.M. McGarrity, F.B. McLean, and D. Habersat, *IEEE Transactions on Electron Devices*, vol. 55, iss. 8, pp. 2029-2040, 2008.
- [50] S. Potbhare, N. Goldsman, G. Pennington, A. Lelis, and J. M. McGarrity, *J. Appl. Phys.*, vol. 100, 044515, 2006.
- [51] S. Potbhare, N. Goldsman, A. Akturk, M. Gurfinkel, A. Lelis, and J.S. Suehle, *IEEE Transactions on Electron Devices*, vol. 55, No. 8, pp. 2061-2070, 2008.
- [52] S.K. Powell, N. Goldsman, J.M. McGarrity, J. Bernstein, C.J. Scozzie, and A. Lelis, *J. Appl. Phys.* **92**, 4053 (2002).
- [53] S. Potbhare, Ph.D. Dissertation, University of Maryland, 2008.
- [54] R.M. Martin, *Electronic Structure: Basic Theory and Practical Methods*, Cambridge University Press, 2008.
- [55] C. Kittel, *Introduction to Solid State Physics*, John Wiley & Sons, Inc., New York, 1986.
- [56] P. Giannozzi *et al.*, *J. Phys.: Condens. Matter*, vol.**21**, 395502, 2009.
- [57] G. Henkelman, B. P. Uberuaga, and H. Jonsson, *J. Chemical. Phys.* vol. **113**, no. 22, pp. 9901-9904 (2000).

- [58] F. Devynck, F. Giustino, P. Broqvist, and A. Pasquarello, *Phys. Rev. B* **76**, 075351 (2007).
- [59] J. Sarnthein, A. Pasquarello, and R. Car, *Phys. Rev. B*, vol. **52**, no. 17, pp. 12690-12695 (1995).
- [60] F. Wooten, K. Winer, and D. Weaire, *Phys. Rev. Lett.*, vol. **54**, no. 13, pp. 1392-1395 (1985).
- [61] Y. Tu, J. Tersoff, G. Grinstein, and D. Vanderbilt, *Phys. Rev. Lett.*, vol. **81**, no. 22, pp. 4899-4902 (1998).
- [62] R. A. Murray, and J. G. Gualtieri, *Proceedings of the 43rd Annual Symposium on Frequency Control, 1989.*, pp.477 - 484, 31 May-2 Jun 1989.
- [63] Benoit *et.al.*, *Eur. Phys. J. B* **13**, 631-636 (2000).
- [64] D. P. Ettisserry, N. Goldsman, A. Akturk, A. J. Lelis, *Semiconductor Device Research Symposium (ISDRS), 2013 International*, 11-13 Dec. 2013.
- [65] A. El-Sayed, M.B. Watkins, V.V. Afanasev, and A.L. Shluger, *Phys. Rev. B* **89**, 125201 (2014).
- [66] S. Goedecker, M. Teter, and J. Hutter, *Phys. Rev. B* vol. **54**, no. 3, pp. 1703-1710 (1996).
- [67] J. P. Perdew, K. Burke, and M. Ernzerhof, *Phys. Rev. Lett.* **77** (18), 3865-3868 (1996).

- [68] A. Alkauskas, P. Deak, G. Neugebauer, A. Pasquarello, C. G. Van de Walle, *Advanced Calculations for defects in Materials*, Wiley-VCH Verlag & Co. KGaA, Weinheim, Germany (2011). ISBN: 978-3-527-41024-8.
- [69] G.L. Zhao and D. Bagayoko, *New J. Phys.* **2**, No. 16, pp.1-12 (2000).
- [70] M.A. Anders *et.al.*, *Integrated Reliability Workshop Final Report (IIRW), 2014 IEEE International* , pp. 16-19, 12-16 Oct. 2014.
- [71] P. M. Lenahan, and P. V. Dressendorfer, *J. Appl. Phys.* **55**, 3495 (1984).
- [72] J. F. Conley-Jr., P. M. Lenahan, A. J. Lelis, and T. R. Oldham, *IEEE Trans. Nuclear Science*, vol. **42**, no. 6, pp. 1744-1749, Dec. 1995.
- [73] T. Grasser *et. al.*, *IEEE Trans. Electron Devices*, vol. 58, no. 11, pp. 3652-3666, Nov. 2011.
- [74] V. V. Afanas'ev, and A. Stesmans, *Appl. Phys. Lett.* **69**, 2252 (1996).
- [75] A. J. Lelis, R. Green, and D. B. Habersat, *Mater. Sci. Forum*, vols. 679–680, pp. 599–602, Mar. 2011.
- [76] A. J. Lelis, R. Green, D. B. Habersat, and N. Goldsman, *Mater. Sci. Forum*, vols. 645–648, pp. 983–986, Apr. 2010.
- [77] R. Green, A. J. Lelis, and D. B. Habersat, *Mater. Sci. Forum*, vol. 717–720, pp. 1085–1088, May 2012.
- [78] A. Oshiyama, *Jpn. J. Appl. Phys.*, vol. **37**, pp. L 232–L 234, 1998.
- [79] C. J. Nicklaw, Z.-Y. Lu, D. M. Fleetwood, R. D. Schrimpf, and S. T. Pantelides, *IEEE Trans. Nuclear Science*, vol. 49, no. 6, pp. 2667-2673, Dec. 2002.

- [80] L. Giacomazzi, L. Martin-Samos, A. Boukenter, Y. Ouerdane, S. Girard, and N. Richard, *Phys. Rev. B* **90**, 014108 (2014).
- [81] N. L. Anderson, R. P. Vedula, P. A. Schultz, R. M. Van Ginhoven, and A. Strachan, *Phys. Rev. Lett.* **106**, 206402 (2011).
- [82] P. V. Sushko, S. Mukhopadhyay, A. S. Mysovsky, V. B. Sulimov, A. Taga, and A. L. Shluger, *J. Phys.: Condens. Matter* **17**, pp. S2115–S2140, (2005).
- [83] S. Mukhopadhyay, P. V. Sushko, A. M. Stoneham, and A. L. Shluger, *Phys. Rev. B* **71**, 235204 (2005).
- [84] S. Mukhopadhyay, P. V. Sushko, A. M. Stoneham, and A. L. Shluger, *Phys. Rev. B* **70**, 195203 (2004).
- [85] A. Alkauskas, P. Broqvist, and A. Pasquarello, *AIP Conference Proceedings* **1199**, 79 (2010).
- [86] E. Choi, and K. J. Chang, *Appl. Phys. Lett.* **94**, 122901 (2009).
- [87] D. P. Ettisserry, N. Goldsman, A. Akturk, and A. J. Lelis, *J. Appl. Phys.* **116**, 174502 (2014).
- [88] H. P. Komsa, T. T. Rantala, and A. Pasquarello, *Phys. Rev. B.* **86**, 045112 (2012).
- [89] G. Makov and M.C. Payne, *Phys. Rev. B* **51** , No. 7 (1995).
- [90] S. Lany, and A. Zunger, *Modelling Simul. Mater. Sci. Eng.* **17**, 084002 (2009).
- [91] C. G. Van de Walle, and R. M. Martin, *Phys. Rev. B* vol. **34**, no. 8, pp. 5621-5634 (1986).

- [92] D. P. Ettisserry, N. Goldsman, A. Akturk, and A. J. Lelis, *Simulation of Semiconductor Processes and Devices (SISPAD), 2014 International Conference on* , pp. 61-64, Sept. 2014.
- [93] V. Afanas'ev, M. Bassler, G. Pensl, M. J. Schulz, E. S. von Kamienski, *J. Appl. Phys.* **79**, 3108 (1996).
- [94] B. Silvi, and A. Savin, *Nature*, vol. **371**, pp. 683-686, Oct. 1994.
- [95] M.A. Alam, and S. Mahapatra, *Microelectronics Reliability* **45** pp. 71–81, (2005).
- [96] A. L. Shluger, and K. P. McKenna, *Reliability Physics Symposium (IRPS), 2013 IEEE International*, pp. 5A.1.1-5A.1.9, Apr. 2013.
- [97] T. Grasser, B. Kaczer, W. Goes, Th. Aichinger, Ph. Hehenberger, and M. Nelhiebel, *IEEE 47th Annual International Reliability Physics Symposium*, Montreal, 2009.
- [98] R. Green, A. J. Lelis, M. El, and D. B. Habersat, *Mater. Sci. Forum*, vols. 740–742, pp. 549–552, Jan. 2013.
- [99] A. Alkauskas, P. Broqvist, F. Devynck, and A. Pasquarello, *Phys. Rev. Lett.* **101**, 106802 (2008).
- [100] Y. Mitani, M. Nagamine, H. Satake, and A. Toriumi, *IEEE International Electron Devices Meeting IEDM '02*, pp. 509–512, 8-11 Dec. 2002.
- [101] S. Wang, M. Di Ventra, S. G. Kim, and S. T. Pantelides, *Phys. Rev. Lett.* **86**, 5946 (2001).

- [102] C. Kohler, Z. Hajnal, P. Deak, T. Frauenheim, and S. Suhai, *Phys. Rev. B* **64**, 085333 (2001).
- [103] Y. Hijikata, H. Yaguchi, M. Yoshikawa, and S. Yoshida, *Applied Surface Science* **184**, pp. 161-166 (2001).
- [104] A. Savin, R. Nesper, S. Wengert, and T. F. Fassler, *Angew. Chem. Int. Ed. Engl.*, **36**, pp. 1808–1832 (1997).
- [105] M. C. Lin, Y. He, and C. F. Melius, *J. Phys. Chem.*, **97** (36), pp. 9124–9128 (1993).
- [106] X. Zeng, M. Ge, Z. Sun, and D. Wang, *Inorg. Chem.*, **44** (25), pp. 9283–9287 (2005).
- [107] Y. Xu *et. al.*, *J. Appl. Phys.* **115**, 033502 (2014).
- [108] Private communication, Prof. Salamanca Riba at University of Maryland, College Park, Summer 2014.
- [109] Y. Liu, M. R. Halfmoon, C. A. Rittenhouse, and S. Wang, *Appl. Phys. Lett.* **97**, 242111 (2010).
- [110] Y. Ono *et. al.*, *Appl. Phys. Lett.* **62**, 375 (1993).
- [111] S.M. Han *et. al.*, *J. Appl. Phys.* **83**, No. 4, 2172 (1998).
- [112] A. F. Basile and P. M. Mooney, *J. Appl. Phys.*, vol. 111, 094509, 2012.
- [113] N.S. Saks, S.S. Mani, and A.K. Agarwal, *Appl. Phys. Lett.* **76**, 2250 (2000).
- [114] C.G. Van de Walle, and J. Neugebauer, *J. Appl. Phys.* **95**, 3851 (2004).

[115] S. Dhar, A.C. Ahyi, J.R. Williams, S.H. Ryu, and A.K. Agarwal, *Materials Science Forum*, vol. 717-720, pp. 713-716, 2012.

[116] A. Kokalj, *Comp. Mater. Sci.*, vol. 28, p. 155, 2003.

## Journal and Conference Publications

### Journal Publications:

1. D.P. Ettisserry, N. Goldsman, A. Akturk, and A.J. Lelis, “Negative bias-and-Temperature-assisted activation of oxygen-vacancy hole traps in 4H-SiC MOSFETs,” *accepted for publication by the Journal of Applied Physics on 18 July, 2015*.
2. D.P. Ettisserry, N. Goldsman, A. Akturk, and A.J. Lelis, “Structure, bonding, and passivation of single carbon-related oxide hole traps near 4H-SiC/SiO<sub>2</sub> interfaces,” *Journal of Applied Physics* **116**, 174502 (2014).
3. D.P. Ettisserry, N. Goldsman, and A. Lelis, “A methodology to identify and quantify mobility-reducing defects in 4H-silicon carbide power metal-oxide-semiconductor field-effect transistors,” *Journal of Applied Physics* **115**, 103706 (2014).
4. S. Salemi, N. Goldsman, D.P. Ettisserry, A. Akturk, and A. Lelis, “The effect of defects and their passivation on the density of states of the 4H-silicon-carbide / silicon-dioxide interface,” *Journal of Applied Physics* **113**, 053703 (2013).

### Peer-reviewed Conference Presentations:

1. D.P. Ettisserry et. al., “Mechanisms of Nitrogen incorporation at 4H-SiC/SiO<sub>2</sub> interface during Nitric Oxide passivation – A first principles study,” accepted for oral presentation at the *Intl. Conference on Silicon Carbide and Related Materials (ICSCRM)*, 2015.
2. D.P. Ettisserry et. al., “Modeling of oxygen-vacancy hole trap activation in 4H-SiC MOSFETs using Density Functional Theory and Rate Equation Analysis,” accepted for oral presentation at the *International Conference on Simulation of Semiconductor Processes and Devices (SISPAD)*, 2015.
3. N. Goldsman, D.P. Ettisserry, A. Akturk, and A. Lelis, “Passivation schemes for hole traps in 4H-SiC MOSFETs,” *Workshop on defects in wide band gap semiconductors*, September 2014, College Park (*Invited*).
4. D.P. Ettisserry et. al., “Effects of carbon-related oxide defects on the reliability of 4H-SiC MOSFETs,” proc. of the *International Conference on Simulation of Semiconductor Processes and Devices (SISPAD)*, pg. 61 (2014, Yokohama).

5. D.P. Ettisserry *et. al.*, “First-principle study of Silicon vacancies near 4H-Silicon Carbide / Silicon dioxide interface”, *International Semiconductor Device Research Symposium* (ISDRS) 2013, Bethesda, MD.
6. D.P. Ettisserry *et. al.*, “Identification and quantification of 4H-SiC (0001)/SiO<sub>2</sub> interface defects by combining density functional and device simulations,” proc. of the *International Conference on Simulation of Semiconductor Processes and Devices* (SISPAD), pg. 396 (2013, Glasgow).
7. S. Salemi, D.P. Ettisserry, N. Goldsman *et al.*, “Density functional and Monte Carlo-based electron transport simulation in 4H-SiC(0001)/SiO<sub>2</sub> DMOSFET transition region,” proc. of the *International Conference on Simulation of Semiconductor Processes and Devices* (SISPAD), pg. 180 (2013, Glasgow).